

Nanostructures Technology, Research and Applications

Academic and Research Staff

James M. Carter, Robert C. Fleming, Dr. Ralf Heilmann, Mark. K. Mondol,
Dr. Mark L. Schattenburg, and Professor Henry I. Smith

Visiting Scientists and Research Affiliates

Dr. David J.D. Carter, Dr. Patrick N. Everett, Dr. James G. Goodberlet, Dr. Michael L. Lim,
Dr. Bernhard Vögeli, Masaki Yoshizawa, Dr. Jo-Ey Wong, Dr. Jong-Ho Yun

Graduate Students

Matthew Abraham, Solomon Assefa, Tymon Barwicz, Reginald Bryant, Carl Chen, Joy Cheng,
Craig Forest, Dario Gil, J. Todd Hastings, John Ho, Chulmin Joo, Wonjoon Jung,
Jung Wan Jung, Stan Jurga, Paul Konkola, Liz Lyons, Debbie Mascaro, Mitch Meinhold,
Rajesh Menon, Euclid Moon, Thomas O'Reilly, Minghao Qi, Timothy Savas, Yanxia Sun,
Sheila Tandon, Xudong Tang, Ryan Williams, Chee Wei Wong, Michael Walsh, Feng Zhang

Collaborators

Professor Dimitri Antoniadis, Professor Marc Baldo, Professor George Barbastathis,
Professor Vladimir Bulovic, Dr. Fernando Castano, Dr. Jane Guo, Professor Leslie Kolodziejski,
Dr. Kornelius Nielsch, Dr. Gale Petrich, Professor Rajeev Ram, Professor Caroline Ross

Technical and Support Staff

James Daley, Cynthia Lewis and Edward Murphy

1. Nanostructures Laboratory

The NanoStructures Laboratory (NSL) at MIT develops techniques for fabricating surface structures with feature sizes in the range from nanometers to micrometers, and uses these structures in a variety of research projects. The NSL is closely coupled to the Space Nanotechnology Laboratory (SNL) with which it shares facilities and a variety of joint programs. The NSL and SNL include facilities for lithography (photo, interferometric, electron-beam, and x-ray), etching (chemical, plasma and reactive-ion), liftoff, electroplating, sputter deposition, and e-beam evaporation. Much of the equipment, and nearly all of the methods, utilized in the NSL/SNL are developed in house. Generally, commercial lithography and processing equipment, designed for the semiconductor industry, cannot achieve the resolution needed for nanofabrication, is inordinately expensive, and lacks the required flexibility for our research. The research projects within the NSL/SNL fall into four major categories: (1) development of nanostructure fabrication technology; (2) nanoelectronics, nanomagnetism and microphotonics; (3) periodic structures for x-ray optics, spectroscopy, atomic interferometry and nanometer metrology; (4) building a bridge to macromolecular assembly and 3-dimensional structures via surface templating and membrane folding.

2. Scanning-Electron-Beam Lithography

Sponsors:

National Science Foundation - DMR-9808941
Defense Advanced Research Projects Agency & U.S. Army Research Office –
Grant DAAD19-99-1-0280

Project Staff:

J. Todd Hastings, Mark K. Mondol, Feng Zhang and Professor Henry I. Smith

Figure 1 is a photograph of the scanning-electron-beam lithography system (VS-26) located in the scanning-electron-beam lithography (SEBL) facility, Room 38-165. This instrument was put together at MIT from two systems (VS-2A and VS-6) obtained as gifts from IBM in the mid 1990's. It has a minimum beam diameter of about 12 nm and is capable of creating large-area patterns composed of multiple stitched fields. Conversion software has been developed which allows a CAD data file to be fractured and translated prior to exposure by the electron-beam tool. Substrates up to 20 cm diameter can be exposed at linewidths down to 30 nm. In order to write concentric circular patterns, such as Fresnel zone plates, software was developed to generate arbitrary arcs of an annulus with user-specified start and finish radii and angles.

The SEBL facility also houses a Raith Turnkey 150 system as shown in Figure 2. Its electron-optical column is essentially identical to that of a Gemini SEM, and provides a beam diameter as fine as 5 nm. Linewidths of 17 nm have been written with the system, as illustrated in Figure 3

The goals of the SEBL facility are to: (1) provide the MIT research community with an in-house SEBL capability for writing directly on experimental device substrates; (2) advance the state-of-the-art in SEBL, particularly with regards to pattern placement accuracy and long-range spatial-phase coherence; and (3) pattern photomasks and x-ray nanolithography masks for in-house use.

The VS-26 and Raith 150 are heavily used in a variety of projects, both mask making and direct write. These have included: 3-D, 2-D, and 1-D photonic bandgap structures; optical-communication filters; arrays of Fresnel zone plates; electrical contacts to bismuth nanowires; high-density magnetic nanodots and rings for information storage; distributed-feedback lasers; sub-100 nm electronic devices; double-gate sub-100nm MOSFETs; diffractive optical elements; and magnetic random access memory devices. Masks have been made for x-ray nanolithography and conformable-contact photolithography.

The Raith 150 is used in a program to develop spatial-phase-locked e-beam lithography. The objectives of this program are to achieve sub-1 nm pattern-placement accuracy, and to reduce the cost and complexity of SEBL. In a conventional SEBL system costing several million dollars, pattern placement accuracy is typically much worse than 10 nm.



Figure 1. Photograph of the VS-26 scanning-electron-beam lithography system.



Figure 2. The Raith-150 electron-beam lithography system. This tool provides sub-20-nm patterning resolution, and pattern-placement accuracy ~ 1 nm via spatial phase locking. The operator is graduate student J. Todd Hastings.

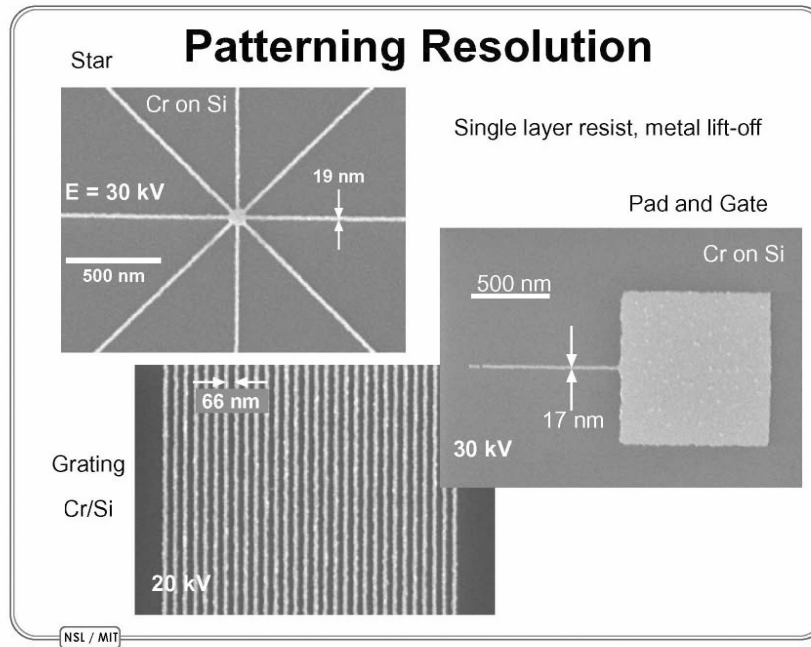


Figure 3: Scanning electron micrograph illustrating the resolution of the Raith 150 SEBL system.

3. Spatial-Phase-Locked Electron-Beam Lithography

Sponsors:

Defense Advanced Research Projects Agency & U.S. Army Research Office
Grant DAAD19-99-1-0280

Project Staff:

Cynthia Caramana, Dr. James Goodberlet, J. Todd Hastings, Mark K. Mondol, Feng Zhang, and Professor Henry I. Smith

Our research in spatial-phase-locked electron-beam lithography (SPLEBL) is aimed at reducing pattern-placement errors in electron-beam-lithography systems to the nanometer level. Such high precision is essential for a variety of future lithographic applications. SPLEBL is currently the only approach capable of achieving such accuracy. As shown in Figure 1, SPLEBL uses a periodic signal, derived from the interaction of the scanning e-beam with a fiducial grid on the substrate, to continuously track the position of the beam while patterns are being written. Any deviation of the beam from its intended location on the substrate is sensed, and corrections are fed back to the beam-control electronics to cancel errors in the beam's position. In this manner, the locations of patterns are directly registered to the fiducial grid on the substrate.

We have implemented two modes of spatial-phase locking on a Raith 150 scanning e-beam lithography system. The Raith 150 is an inexpensive system that provides high resolution (sub-20-nm) patterning. It has little shielding from environmental disturbances and has a number of shortcomings with respect to pattern fidelity. Because the system can only reliably deflect the e-beam over a small area (~100 x 100 μm), patterns must be built up by stitching together an array of these fields. The best field-to-field stitching errors observed without spatial-phase locking have a standard deviation of ~8 nm.

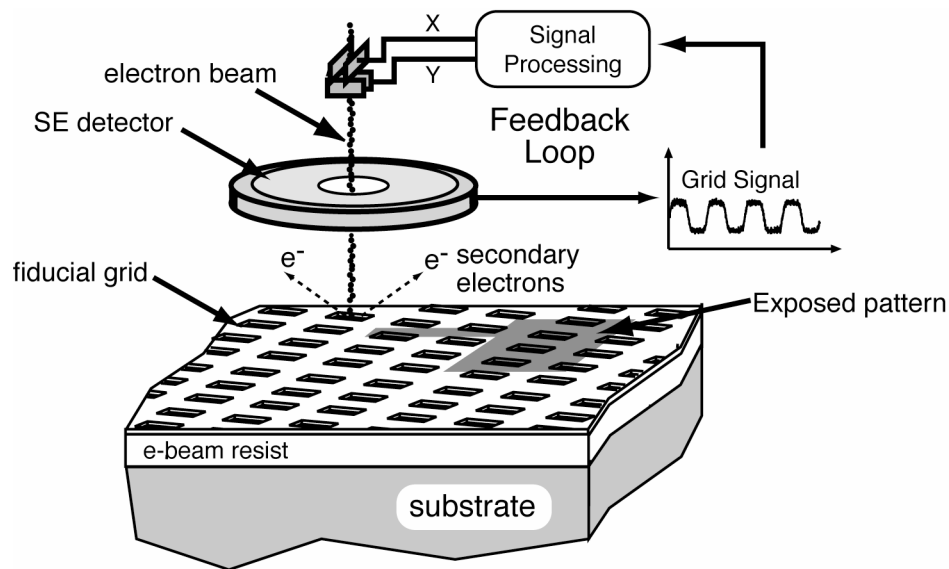


Figure 1: Schematic of the global-fiducial-grid mode of spatial-phase-locked electron-beam lithography. The periodic signal detected from the fiducial grid is used to measure placement error, and feed a correction signal back to the beam deflection system.

In the first mode of spatial-phase locking the fiducial grid is segmented into small areas of the substrate that will not be patterned. Before exposing each stitched field, the electron beam scans over these areas and detects the spatial-phase of the grid. As a result, the field's shift, scaling, and rotation can be corrected before writing the pattern. This technique achieved field stitching errors with a standard deviation of 2.6 nm, and has been used to expose 225-nm-period Bragg-grating filters in silicon-on-insulator waveguides.

To achieve maximum pattern-placement accuracy it is desirable to constantly correct the beam position during exposure. To do so requires that the grid cover the entire substrate but not perturb the electron-beam. Toward this end, we place a thin (<10 nm) metallic fiducial grid on top of PMMA e-beam resist. This grid produces a secondary-electron signal, while the primary electron-beam passes easily through to expose the resist below. Because the grid is conductive, it opens the possibility of obtaining higher signal-to-noise ratios through voltage contrast.

In order to implement the continuous-feedback mode, it was necessary to add raster-scan capability to the Raith 150. We added the required hardware and software to switch the beam on and off at desired times as the system raster-scans the beam across the field. In addition, we implemented hardware and software to measure the residual field distortion relative to the fiducial grid, and to apply 3rd order corrections during the raster-scan exposures.

To provide continuous feedback control for beam positioning, we developed a phase-locking algorithm. The e-beam is scanned at an angle to the fiducial grid axes. This produces a signal with two fundamental frequency components whose phases are used to calculate the x- and y-beam-placement errors. To implement this algorithm we added analog-to-digital conversion for the secondary electron signal, digital-signal processing with custom software for correction calculations, and digital-to-analog conversion for the x- and y- correction signals.

To evaluate the effectiveness of this algorithm we exposed test patterns with a 10 keV electron beam using an 8-nm thick, 250-nm period, Al fiducial grid. Figure 2 shows stitching measurements of the resulting pattern with standard deviations at or below 1.3 nm. Locking to the fiducial grid ensures a comparable level of global pattern-placement accuracy. These experiments were conducted with patterns that do not require beam-current modulation to continuously track the grid. Developing appropriate current-modulating electron optics remains a high priority to enable patterning of arbitrary patterns. Another high priority for future research is to develop a means of putting down the fiducial grid that does require multi-step lithography.

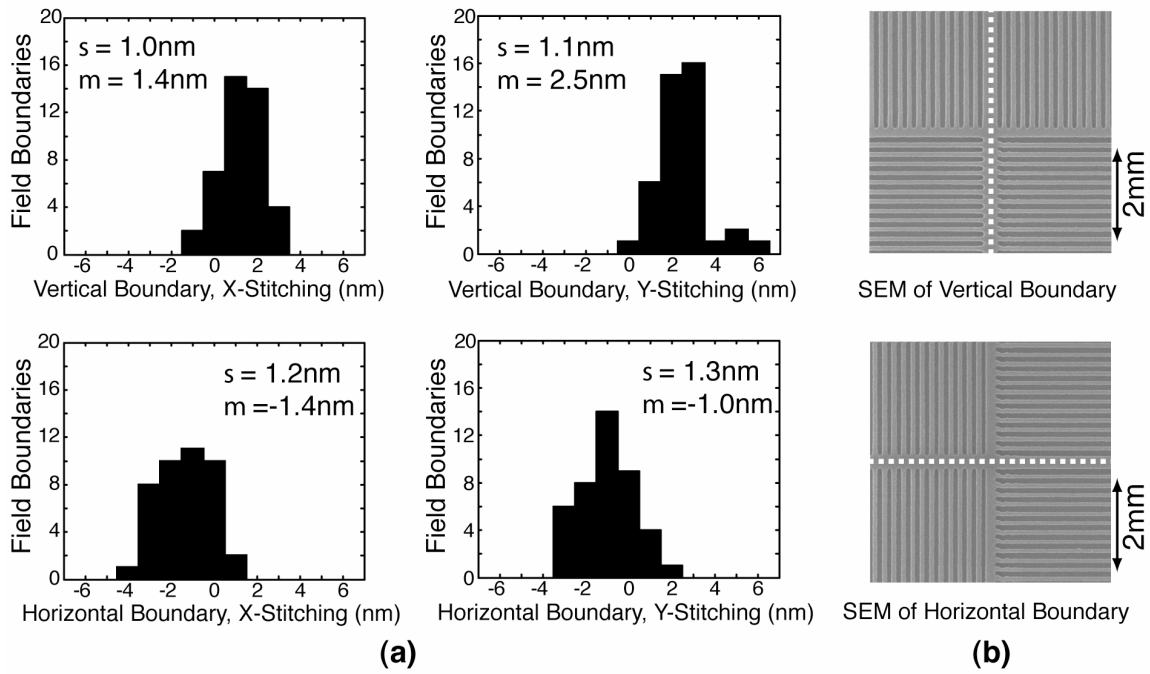


Figure 2: (a) Histograms showing x- and y-stitching measurements at all 84 field boundaries of 49 stitched fields. Spatial-phase locking has reduced the standard deviation of the stitching errors to below 1.3 nm. (b) Sample 200-nm period stitched grating patterns. The dashed line indicates the field boundary.

4. X-Ray Nanolithography

Sponsors:

Defense Advanced Research Projects Agency and University of Wisconsin
Contract # A720156

Project Staff:

Lynn Chen, James M. Daley, Euclid E. Moon, and Professor Henry I. Smith

For several years, we have been developing the tools and methods of x-ray nanolithography. We have explored the theoretical and practical limitations, and endeavored to make its various components (*e.g.* mask-making, resists, electroplating, sources, alignment, etc.) reliable and “user-friendly.” Because of the critical importance of x-ray mask technology, we discuss this in a separate section.

X-ray nanolithography (XNL) is a reliable and simple means of replicating patterns with feature sizes down to about 20 nm. Typically, the x-ray mask is made with scanning-electron-beam lithography (SEBL), although we very often employ a combination of interference lithography, photolithography, SEBL, and XNL to fabricate the mask. Once the mask is fabricated it can be replicated an unlimited number of times. The simplicity and process latitude of XNL make it ideally suited for nanostructures research. In fact, at the present time, XNL is the only technique available for replicating sub-100 nm patterns of arbitrary geometry.

In the NanoStructures Lab (NSL), x-ray lithography is used in the fabrication of a large variety of structures and devices, including: photonic bandgap devices, short-channel MOSFETs, and optical channel-dropping filters.

Our sources for x-ray nanolithography are simple, low-cost electron-bombardment targets. We utilize the L line of copper at $\lambda = 1.32$ nm. The sources are separated by a 1.5 μm -thick SiN_x vacuum window from a helium-filled exposure chamber.

We have submitted a proposal to DARPA for the purchase of a laser-plasma source from JMAR, Inc. Their source operates at a wavelength of 1.1 nm which is very close to the wavelength we currently use. Figure 1 is an example of some lithography done with the JMAR source using an MIT mask. Acquisition of a JMAR laser-plasma source should enable us to reduce our exposure times from hours to minutes.

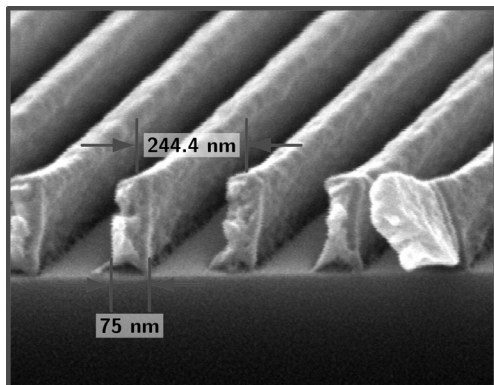


Figure 1: Example of x-ray lithography done with the JMAR laser plasma x-ray source.

Although the wavelength used is very short (1.32 nm) compared to the minimum feature sizes of interest (*e.g.*, 20 nm) diffraction in the gap between the mask and the substrate can be detrimental. For example, with a Cu_L source, a 50 nm feature must be exposed at a mask-to-substrate gap of less than about 4 μm in order to maintain good process latitude. A 25 nm

feature would require a gap of 1 μm . For very small features, we eliminate the gap and use contact between the substrate and the flexible membrane mask. This technique has enabled us to replicate features as small as 20 nm in a practical, reproducible way. Figure 2 shows scanning electron micrographs of device patterns with feature sizes less than 40 nm.

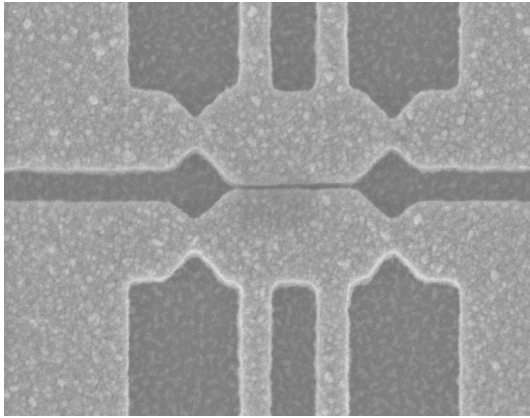


Figure 2. Scanning electron micrographs of device pattern with feature size $\sim 20\text{nm}$ achieved by x-ray nanolithography.

We are currently investigating if gaps below 4 μm can be reliably measured and controlled. For this, the substrate will have to be much flatter than 1 μm , something that is easily achieved with an appropriate pin chuck such as those used in optical projection lithography steppers. In fact, for the same minimum linewidth, the control of substrate flatness in x-ray lithography is less critical than in optical projection lithography by a factor 13. For a linewidth control of 10% the control of gap in x-ray lithography is given by

$$\Delta G = 0.2 G.$$

At linewidths of 25 nm and 50 nm, the allowable gap variation is 680 nm and 170 nm, respectively. Since the mask, if made properly, can be optically flat, the only contributor to gap variation is non flatness of the wafer or tilt of the mask relative to the wafer. We believe these can be controlled to meet the above requirements. For measuring gaps below 4 μm we will use the “transverse chirp gapping” scheme described elsewhere in this report.

Another approach to achieving extremely fine linewidths is to use a much shorter wavelength, around 0.5 nm. At this wavelength the high-atomic-number materials such as gold, tungsten and tantalum, and their alloys, have x-ray attenuation comparable to that at a wavelength of 1 nm. The shorter wavelength enables one to use a larger gap between mask and substrate for the same resolution. The penalty one pays is that the attenuation of resist is significantly reduced, necessitating the doping of the resists with materials such as chlorine or bromine. Another issue is the energetic photoelectrons emanating from the substrate. Their deleterious effect can be eliminated by using a trilayer resist, with the bottom buffer layer absorbing the energetic photoelectrons. We are collaborating with F. Cerrina at U. Wisconsin and T. Kitayama of Mitsubishi in the development of this shorter wavelength approach.

5. Adaptive-Membrane-Mask Technology

Sponsors:

Defense Advanced Research Projects Agency/Naval Air Systems Command, Contract N00019-98-K-0110 and Louisiana State University, Contract R110030

Project Staff:

James M. Daley, Thomas B. O'Reilly, Professor Martin Feldman (LSU), Professor George Barbastathis and Professor Henry I. Smith

The conventional approach to maintaining pattern fidelity and overlay in lithography is to minimize distortion in pattern generation and transfer, and to make masks as rigid as possible. Since July 2000, we have been pursuing a radically new approach that seeks to exploit the flexibility of membrane masks. This approach, which we call the adaptive membrane mask (AMM), seeks to actively measure and control mask distortion, making it possible to eliminate or compensate for many types of distortion common in lithography. This approach is similar in spirit to adaptive optics where optical surfaces are actively deformed to compensate for system or media distortions.

Our approach to distortion measurement is based on holographic interferometry. A reference grid is fabricated on the back of a membrane mask using interference lithography (IL). Mask distortion is measured using the holographic-phase-shifting interferometer (HPSI), shown in Figure 1, essentially an IL system modified to measure in-plane distortion of the reference grid on the membrane. We believe that HPSI will be able to measure in-plane distortion of the mask with resolution of the order of 1 nm.

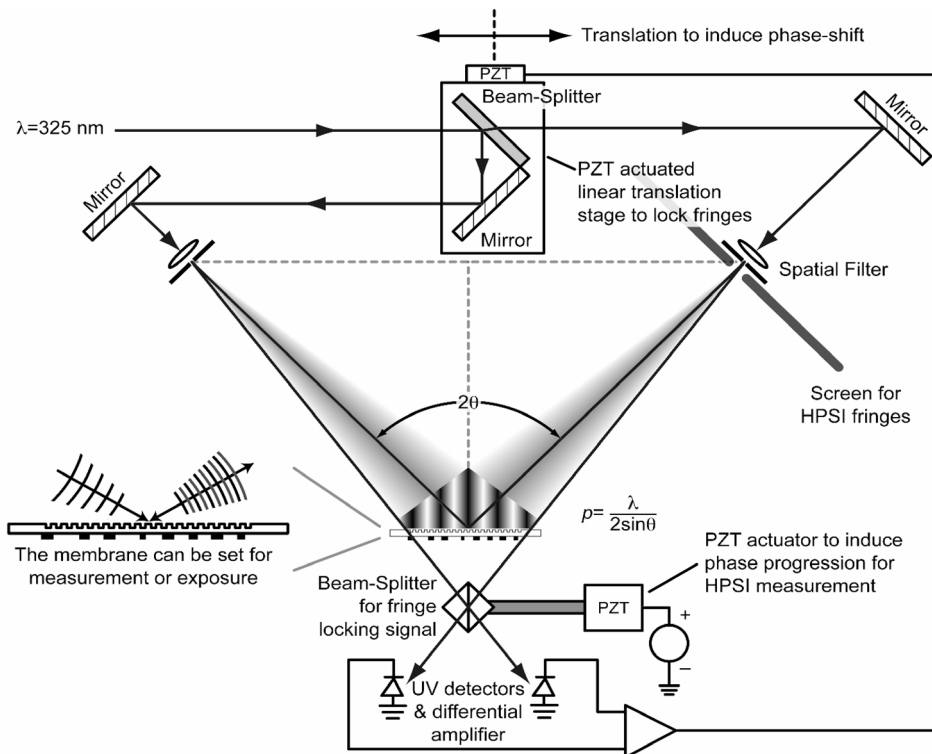


Figure 1. Schematic of the Holographic-Phase-Shifting Interferometer(HPSI). This setup can be used as an interference lithography system to write reference grids as well as a holographic interferometer to measure grid distortion.

Once the distortion is measured, an algorithm developed at MIT is used to calculate the temperature distribution that will generate thermal stresses to eliminate the measured distortion. The membrane mask is heated using a computer-controlled illumination source, based on either a spatial light modulator, such as the Texas Instruments digital micromirror array, or a scanned laser system. The distortion is measured again, and the process is repeated iteratively until the distortion is eliminated. The final temperature distribution is measured using an infrared camera. The proposed implementation is outlined in Figure 2. Because membrane distortion is directly related to temperature, it can be eliminated by maintaining this final temperature distribution.

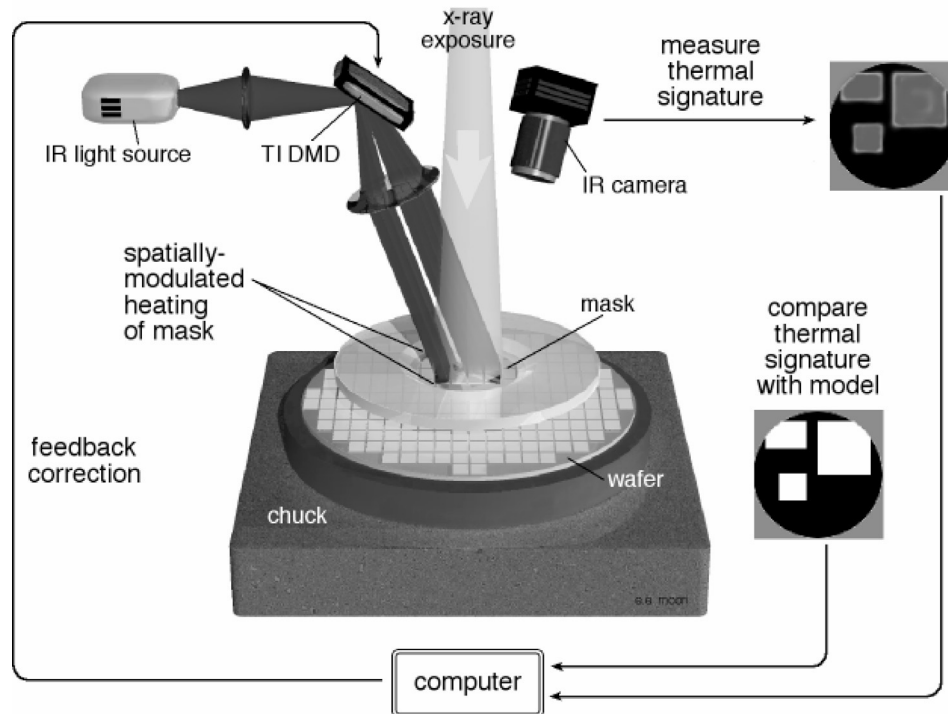


Figure 2. Proposed implementation of Adaptive-Membrane-Mask Distortion Correction

The AMM approach is ideally matched to x-ray lithography (XRL). The primary sources of distortion in XRL are distortion of the mask due to stresses in the absorber layer and by radiation damage. XRL membrane masks used in industry are typically 2 microns thick silicon carbide, which is not subject to radiation damage at exposure levels seen in industry. The ability to measure and correct distortion may allow the use of a wider range of materials for both membrane and absorber, and relax some process constraints currently needed to minimize absorber stress. For instance, masks can be made from silicon nitride, which is less expensive and easier to make than silicon carbide, but is subject to radiation-damage-related distortion. The use of thinner membranes has the additional advantage of reducing exposure times and increasing optical transmission for mask alignment.

An AMM can be used to provide magnification correction. AMM can also be used to correct for wafer distortion, which can arise from a number of causes: high temperature processing, stress in grown overlayers, stress due to ion implantation, etc. As long as these distortions are measurable and repeatable, an adaptive mask can compensate for them, allowing more flexibility in wafer processing. For example, high temperature processes that induce wafer distortion can be used, since the AMM can compensate for them.

The advantages described above also apply to the use of AMM with types of lithography other than XRL that use membrane or stencil masks, including electron-, ion- and neutral-atom

lithography. In addition, we believe that adaptive masks may be applicable to optical-projection lithography (OPL), by far the dominant technique for fabricating semiconductor chips. Although rigid masks are currently used in OPL, reducing the importance of distortion in the mask, OPL is subject to all of the other types of distortion described above. In addition, the projection lens system introduces distortion in the image produced on the substrate. Application of AMM to OPL, should allow control of this distortion, and may allow the use of simpler projection lens systems.

Preliminary work has shown good agreement between experiment and model. Figure 3 compares experimental and analytical results for a simple case where the left half of the membrane is heated. Here, displacements are plotted along a horizontal line in the middle of the membrane.

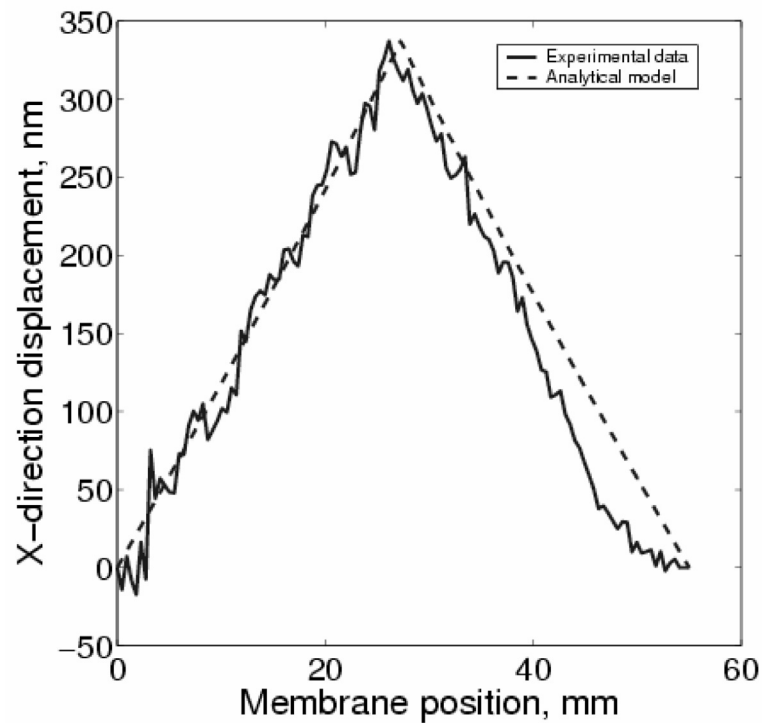


Figure 3. Comparison of experimental and analytical results

6. Nanometer-level Feedback-Stabilized Interferometric Aligning and Gapping in an X-ray Lithographic System

Sponsors:

JMAR/SAL Incorporated, and University of Wisconsin, A720156

Project Staff:

Euclid E. Moon, Lynn Chen, Dr. Patrick N. Everett, and Professor Henry I. Smith

An experimental x-ray exposure system has been constructed that employs Interferometric-Spatial-Phase Imaging (ISPI) for high-precision aligning and gapping. The ISPI scheme utilizes grating and checkerboard marks on mask and substrate. When illuminated with oblique-incidence spatially-coherent light, interference patterns are formed, which are imaged by $f/10$ optics at a 22 degree angle from the x-ray beam at a 110 mm working distance. Since the microscopes and illumination are removed from the path of the x-ray beam, alignment and gap are detected and feedback-controlled during, as well as before, exposure.

As shown in Fig. 1, each alignment mark consists of three gratings (or checkerboards), of slightly different periods, p_1 and p_2 , arranged so that the two outer gratings with p_1 (on the mask) are superimposed over p_2 checkerboards (on the substrate). In the middle of the three-part mark, a p_2 grating is superimposed over a p_1 checkerboard. In this arrangement, when the mask is moved relative to the substrate, interference fringes from the middle part of the mark move in the opposite direction of the fringes from the outer parts. Alignment is determined from the relative spatial phase between the middle and outer fringe sets, measured with a sub-nanometer sensitivity frequency-domain algorithm. Phase bias due to rotation of the camera with respect to the mark is removed by examining the spatial phase difference between the two outer fringe sets.

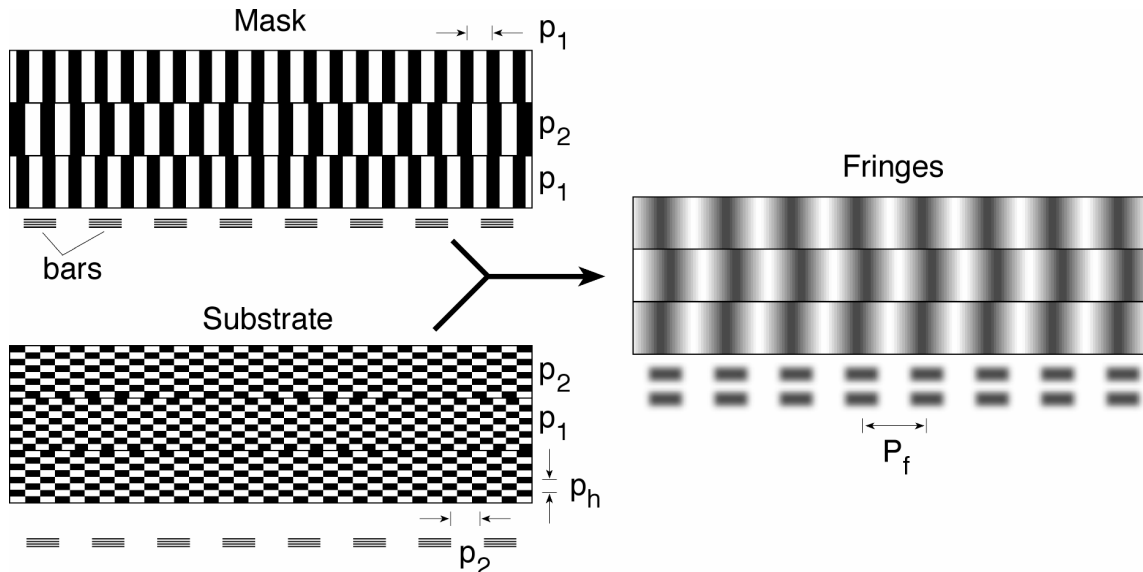


Figure 1: Schematic of ISPI aligning marks. Fine alignment is detected using the spatial phase relation of middle to outer fringe sets. Errors from camera-mark rotation are removed by phase comparison of outer fringe sets. Spatial-phase ambiguity is eliminated by comparing the phase between bar arrays on the mask and wafer, as well as between bars and fringes.

Gap is measured from checkerboards on the mask, which have a constant period in the plane of illumination, but a varying, or chirped, period in the transverse plane. Three chirped gratings are used, with the middle chirp in the opposite direction from the outer chirps. Constant-period fringes can be obtained by design of the chirp rate. In a manner similar to that for alignment, the spatial phase of the fringes encodes gap information. In addition to phase, average intensity and fringe frequency also vary with gap. Fringe frequency variation is indicated in Figure 2, where a middle and outer fringe pair are shown at gaps of (a) 4.3 μm and (b) 19.3 μm . Fringe frequency can be used to resolve gaps to $\pm 1 \mu\text{m}$.

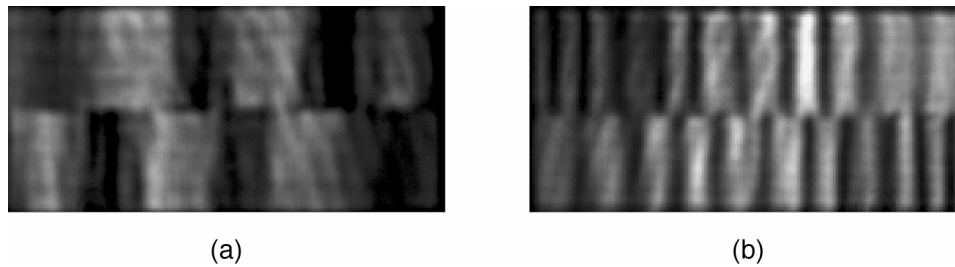


Figure 2: Illustration of fringe variation with gap. Between (a) 4.3 μm and (b) 19.3 μm gaps the number of fringes increases by 0.51 fringe/ μm .

To increase gap resolution, frequency, phase and average intensity of the transverse chirp fringes are used simultaneously. The data from a gap scan between 6 and 8 μm (with 5 nm gap steps) is plotted in Fig. 3(a). The same three quantities are plotted in three dimensions in Fig. 3(b). The curve in Fig. 3(b) traces out a highly repeatable, pseudo-helical path that indicates a unique gap within the 2- μm range. The observed gap detectivity of $<20 \text{ nm}$ is more than adequate for linewidth control of sub-50 nm features in proximity x-ray lithography.

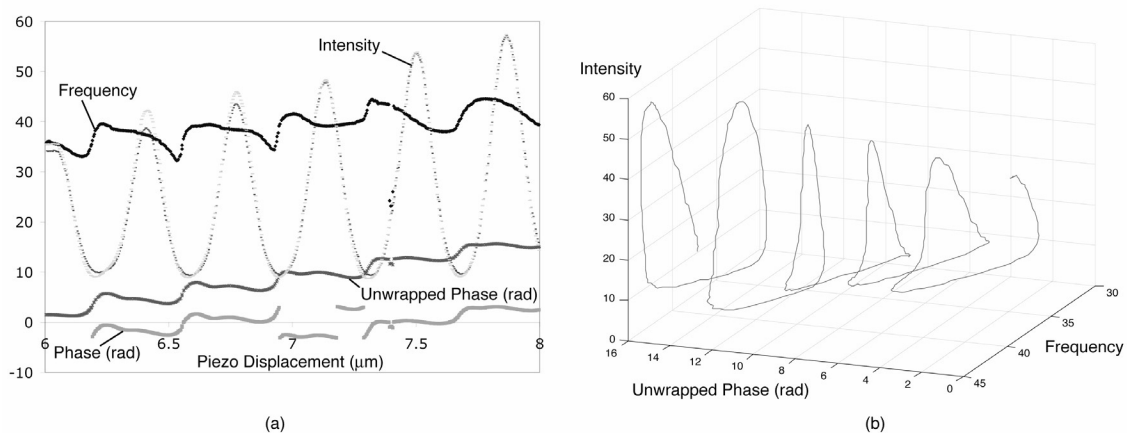


Figure 3: (a) Plot of three measurable quantities in ISPI transverse chirp gapping fringes: frequency, phase, and average intensity as a function of gap. (b) Within the ± 1 range of fringe frequency resolution, a unique correspondence to gap is found from a combination of all three fringe quantities. (Note that in both plots frequency is upshifted by $\sim 4\times$ due to zero padding.)

The same ISPI microscopes are used to detect both alignment and gap, however, alignment and gap have distinct (and conflicting) illumination requirements. Aligning is fundamentally achromatic, so any wavelength within a wide range can be used. In practice, it is advantageous to use multiple laser lines to avoid thin-film interference effects that could cause signal extinction at certain resist thicknesses. Gapping, on the other hand, is intrinsically dependent upon wavelength. Indeed, phase, frequency and intensity in the gap marks all vary with illumination wavelength. Multiple wavelengths, if used simultaneously, would cause confusion from several sets of gap fringes. To meet both requirements, a Closed-Loop Variable Bandwidth light source (Fig. 4) is used to provide a narrow bandwidth for gapping or a broad band for aligning. The CLVB source consists of four diode lasers in the range between 635 and 690 nm, four fiber-coupled beamsplitters, and a compact spectrometer with USB computer link, which permits equalization of the power in the spectral lines during aligning, or measurement of the exact wavelength of a single laser line for gapping.

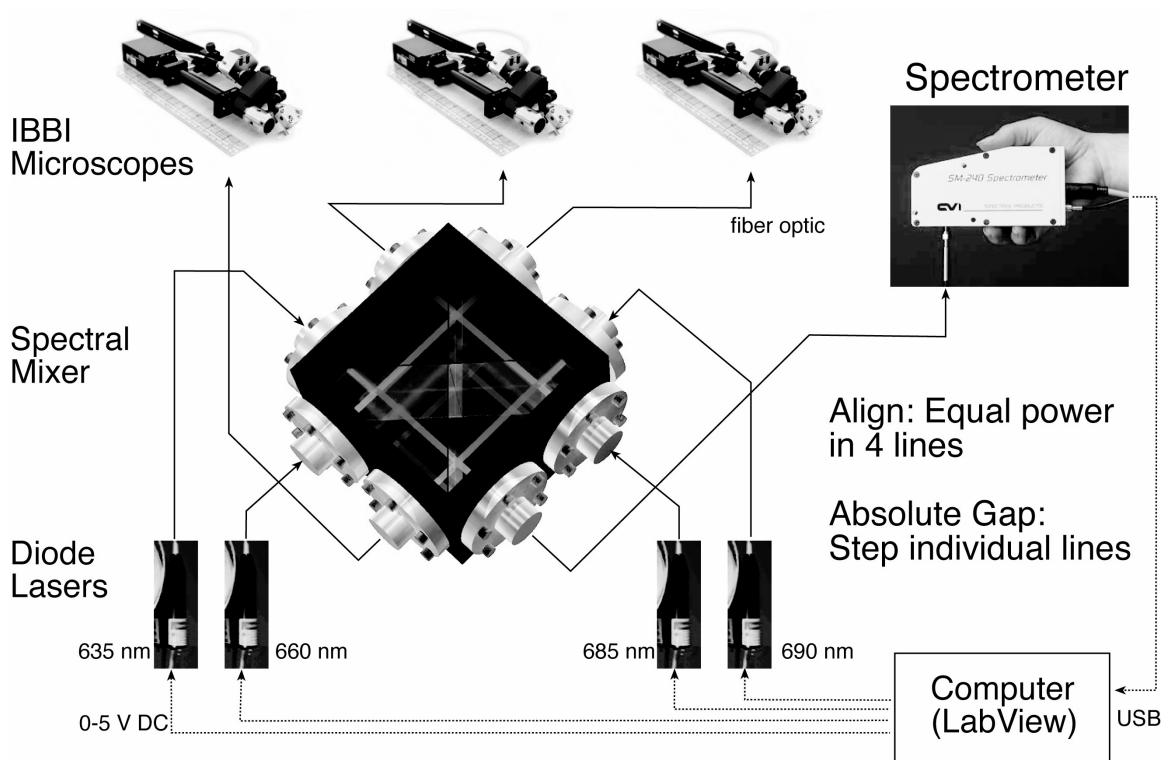


Figure 4: A Closed-Loop Variable Bandwidth (CLVB) light source provides optimum illumination for both aligning and gapping. A single laser line is used for gapping, but a broad spectrum using multiple lasers is ideal for aligning. The spectrometer monitors wavelength when gapping, and relative intensities when aligning.

The unique collection of capabilities inherent to ISPI aligning and gapping is being employed in the fabrication of a variety of electronic and optical devices.

7. Zone-Plate-Array Lithography (ZPAL): The System

Sponsors:

Defense Advanced Research Projects Agency and Army Research Office
Grant No. DAAD19-01-1-0330

Project Staff:

Dario Gil, Rajesh Menon, Amil Patel, and Professor Henry I. Smith

In semiconductor lithography, glass masks are illuminated with deep UV laser light and their image is reduced through a lens onto the substrate to define circuitry. As feature sizes are pushed towards 100 nm and smaller, lithography systems and masks are becoming increasingly complex and costly (~\$1 million per mask set). In addition, the delay in obtaining a mask set, with complex optical-proximity correction and phase-shifting features can be months. This presents a huge hurdle to continuing progress in semiconductor technology.

At the MIT NanoStructures Laboratory, we are pursuing a radically new scheme, which requires no mask, called zone-plate-array lithography (ZPAL), made possible by inexpensive, high-speed computation and micromechanics. ZPAL replaces the "printing press" of traditional lithography with a technology more akin to that of a laser printer. Although it will not have the throughput of an optical stepper, ZPAL is ideal for prototyping and also for semiconductor products requiring only a few wafers, e.g., application-specific IC's.

Instead of a single, massive lens, an array of hundreds or thousands of microfabricated Fresnel-zone-plate lenses is used, each focusing a beam of light onto the substrate. A computer-controlled array of micromechanical mirrors turns the light to each lens on or off as the stage is scanned under the array, thereby printing the desired pattern in a dot-matrix fashion. No mask is required, enabling designers to rapidly change circuit designs. A schematic of ZPAL is shown in Figure 1.

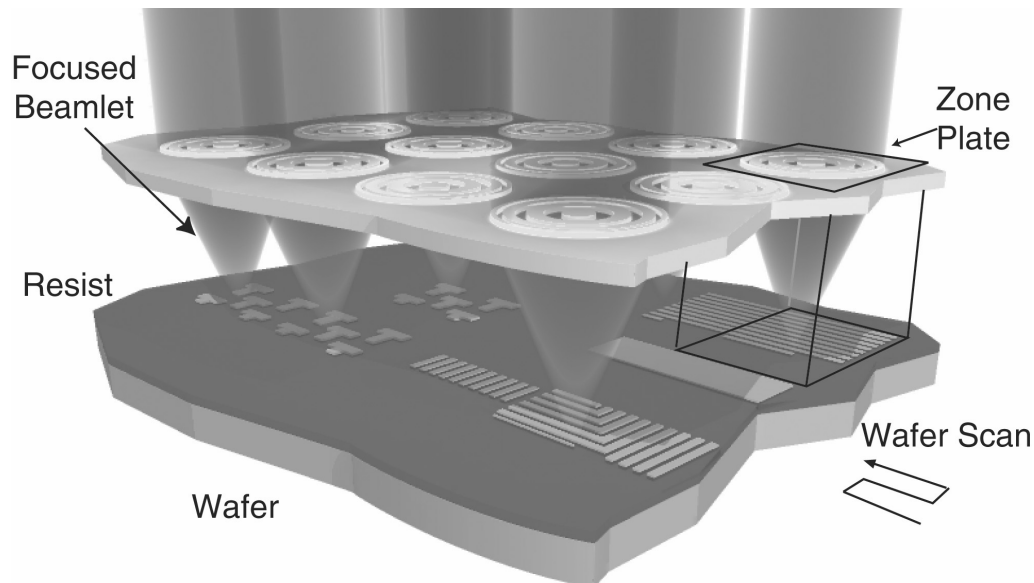


Figure 1: Schematic of zone-plate-array lithography (ZPAL). An array of Fresnel zone plates focuses radiation beamlets onto a substrate. The individual beamlets are turned on and off by upstream micromechanics as the substrate is scanned under the array. In this way, patterns of arbitrary geometry can be created in a dot-matrix fashion. The minimum linewidth is equal to the minimum width of the outermost zone of the zone plates.

ZPAL leverages advances in nanofabrication, micromechanics, laser-controlled stages, and high-speed, low-cost computation to create a new form of lithography.

Recent research efforts have primarily concentrated on developing planar processes for fabrication of zone-plate arrays, proving the lithographic capabilities of zone plates, developing robust system-simulation tools and building a fast data-delivery system.

Fabrication of Phase-Zone-Plate Arrays:

Phase-zone-plate arrays are fabricated using a process consisting of electron-beam lithography and self-aligned electrochemical etching. We use the negative e-beam resist HSQ (hydrogen silsesquioxane, by Dow Corning). HSQ's extraordinarily high resolution (~10nm) and its glass-like properties make it an optimal choice for fabricating diffractive-optical elements that operate in the UV and DUV regimes. HSQ has an index of refraction very close to that of fused silica, and negligible absorption down to 157nm. The resist is first spun to the thickness corresponding to the desired phase step for the zone plate, patterned with e-beam lithography, and then the unexposed regions are developed away. It is also necessary to prevent the light from transmitting through those areas on the substrate not occupied by the zone plate. This is achieved by evaporating metal (chrome in this case) onto the substrate. Since the metal within the zones of the zone plate is electrically isolated from the metal outside, the metal within the zone plate can be removed by an electrochemical etching process (Fulton/Dolan Process).

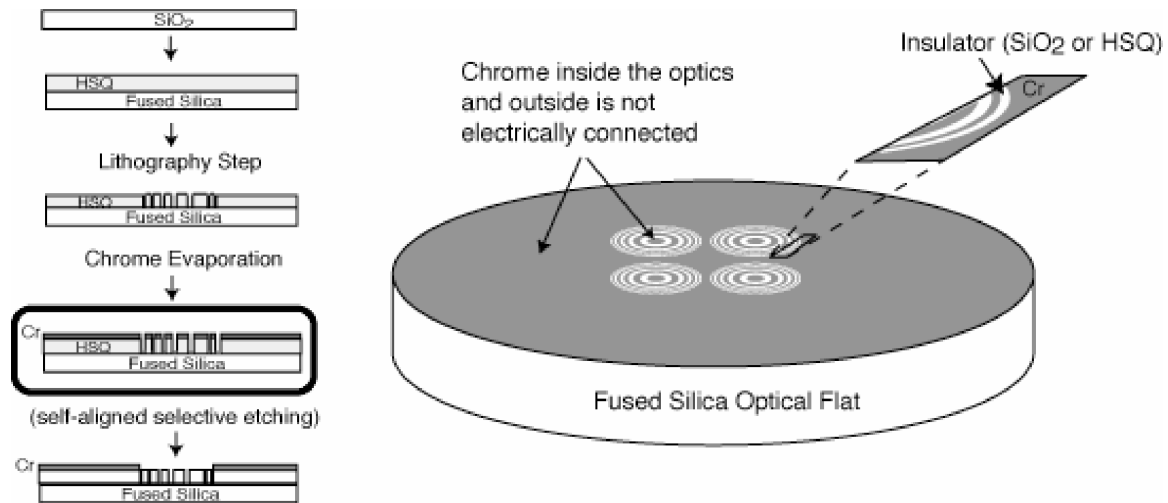


Figure 2: Left: Typical sequence of the self-aligned process requiring a single-lithography step. Starting with a transparent blank material, HSQ is spun on it. The thickness of the HSQ is chosen to provide the appropriate phase step for the zone plate. After patterning the elements in HSQ, the absorber metal is evaporated. Right: Detail of the process after the absorber has been evaporated. Note that the absorber (chrome in this case) inside the zone plate and outside is not electrically connected. The lack of electrical connectivity will allow for the absorber within the diffractive elements to be removed by means of a wet-etch Fulton/Dolan technique.

Zone-plate arrays can be manufactured in a highly reliable manner. We have fabricated zone plates that perform very close to their theoretical limit (as shown in another section), and have manufactured arrays containing over 1,000 zone plates (see figure 3.). We believe much larger arrays, of ~1M zone plates, are possible.

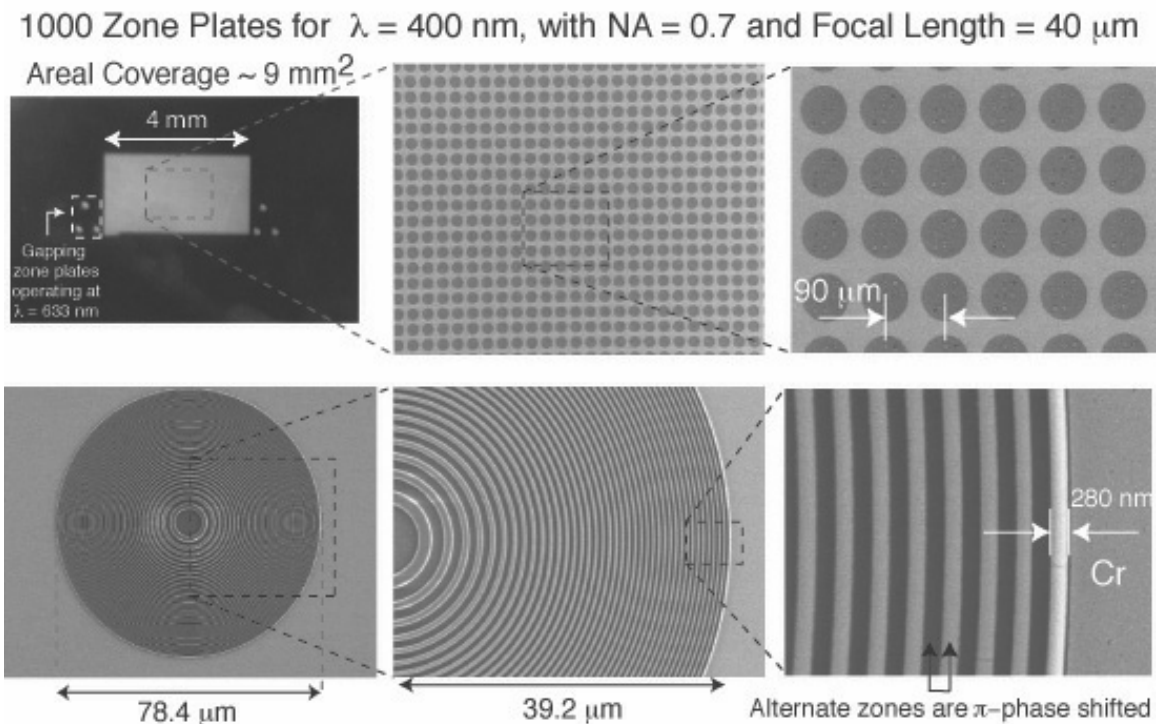


Figure 3: Large zone plate arrays can be readily fabricated with our novel process that requires a single lithography exposure and no etching, even for the case of phase zone plates. Top-left: Optical micrograph showing an array containing over 1,000 zone plates with an aerial coverage of 9 mm^2 . Bottom-right: Detail of the outer-most zones. The duty-cycle is very close to 50%, and the phase shift between alternate zones was controlled to about 1%.

System simulation Tools:

We have developed simulation tools to design zone plates as well as other diffractive focusing elements and to study the effect of various system parameters on the lithographic performance of ZPAL.

The simulation begins with modeling the diffraction of light by a zone plate using the finite-difference time-domain method. Calculated fields are further propagated to the focal plane of the zone plate using a vector plane-wave spectrum method. Since this is a full-vector model of electromagnetic theory, it gives extremely accurate predictions about the spatial structure of the point-spread function (PSF). This is illustrated in figure 4, where the PSF of the zone plate was experimentally determined by exposing single spots at a large number of doses in photoresist. The photoresist, being highly nonlinear, acts as a sampler to obtain points on the PSF. The excellent agreement between the model and experiment attests to the model's accuracy as well as the reliable fabrication of the zone plates.

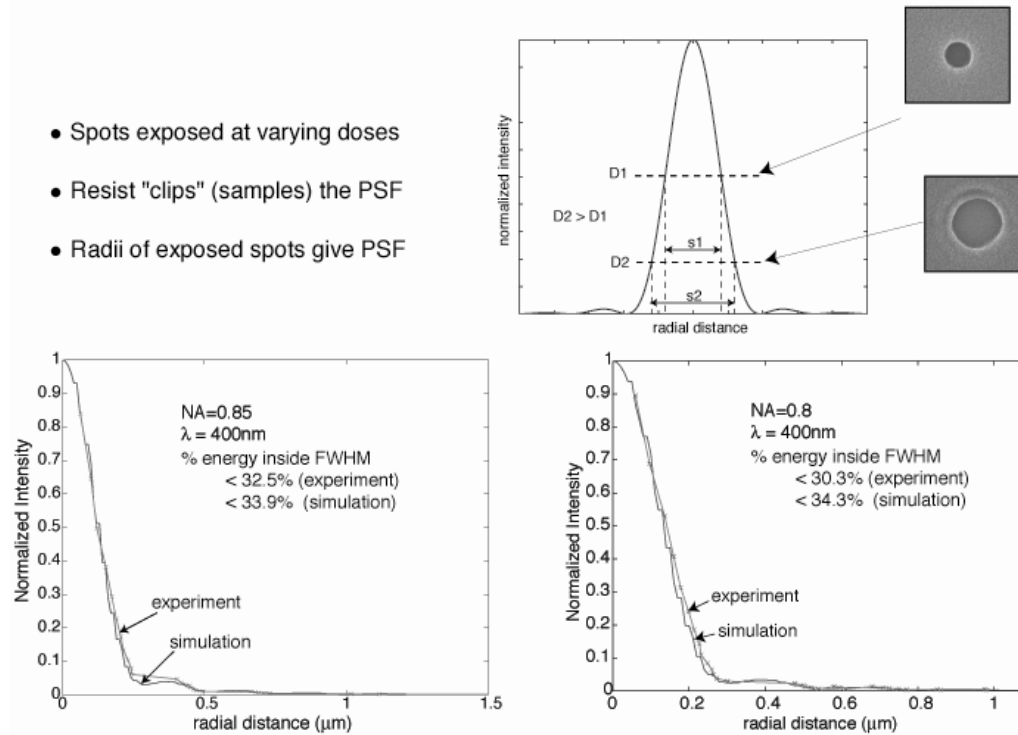


Figure 4: Top: Experimental process for quantifying the PSF. Spots of several exposure times were patterned in photoresist, which acts as a sampler of the PSF. The radii of the exposed spots can be assembled to form the PSF. Bottom: PSFs for zone plates of NA=0.85 (left) and NA=0.8(right) were determined experimentally using the simulation tools. The results show excellent agreement.

Since ZPAL results in an incoherent addition of spots in photoresist, by convolving the PSF with a desired pattern, we can simulate exposed patterns. This is important to understand various component-tolerances in the system.

Micromechanics & Data Delivery System:

We have switched from the previously reported method of multiplexing the light for ZPAL, the Texas Instruments DMD™ micromirror array, to the Silicon Light Machines Grating Light Valve™ (GLV™) linear array. Although the GLV™ has a smaller number of pixels (1,088) compared to the DMD™ micromirror array (~1 million or more), the higher speed of operation of the GLV™ (20ns rise time as opposed to 20 ms for the DMD™), the fact that gray-scaling is built in, and its diffractive mode of operation (making it compatible with shorter wavelengths, possibly even down to 157nm) made it a superior choice for ZPAL.

The GLV™ is a micromechanical phase grating consisting of parallel rows of reflective Al ribbons. Alternate rows of ribbons can be pulled down electrostatically in a controlled manner to create diffraction effects on incident light. When no force is applied, all the ribbons lie in the same plane. If illuminated, incident light will be reflected from their surfaces at the same angle at which it is incident. When alternate ribbons are pulled down, a grating structure is created. In this state diffraction will produce light at an angle different from that of the incident light. By alternating between these two states (i.e. from flat ribbons to a grating structure) the GLV™ can switch light ON and OFF. Furthermore, by tuning the applied electrostatic force, the depth to which the ribbons are pulled down can be controlled, impacting the amount of light diffracted into the first

order. Grayscaleing of the incident light can be achieved in this manner. Each of the 1088 pixels present in the linear array can accept 8-bits of grayscaleing (256 levels). Since the motion involved in switching the pixels of the GLV™ is small (one-quarter wavelength), the GLV™ is capable of very high switching speeds, with a rise time from the ON to the OFF position of only 20ns. One pixel of the linear array is depicted schematically in figure 5, along with the intended implementation in ZPAL.

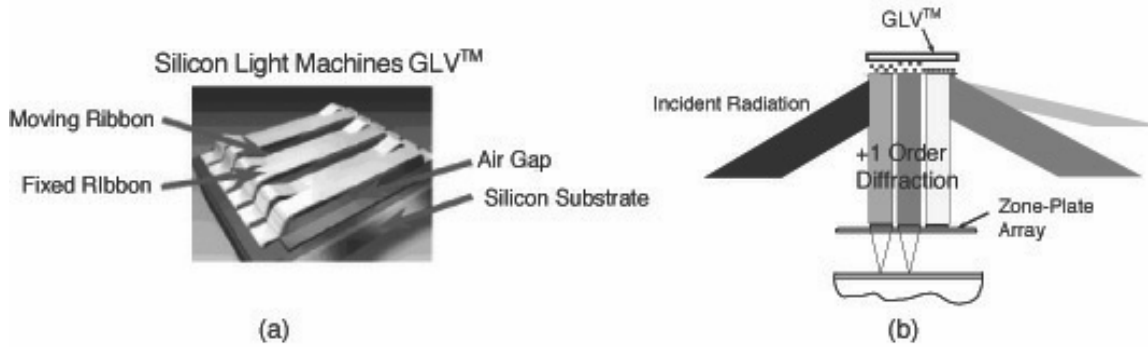


Figure 5: Schematics of the Silicon Light Machines Grating Light Valve (GLV) device. (a): Fixed and electrostatically-deflected moving ribbons create a variable-height grating. (b): Incident light will be diffracted from the grating at a known angle, with varying intensity depending on the height of the grating. Each pixel, a small patch of the grating, diffracts onto a single zone plate, thus turning on and off (or grayscaleing) each pixel written onto the substrate in ZPAL.

We have built a custom system to deliver the pattern data from the ZPAL control computer to the 1,088 pixels of the GLV™ array at very high speeds. Data is first transferred from the computer through the PCI bus to a National Instruments digital I/O board (Model#: 6601). The data is then sent from the I/O board to the GLV™ through a custom-made printed circuit board (PCB), which performs the data routing and interpretation as required by the GLV™ electronics. The I/O board, equipped with an 80 Mhz clock to enable clocking the data at very high speeds, has the capability of both reading data from the control computer and sending data to the GLV™ simultaneously. In practice, two I/O boards are used in parallel to achieve high data rates. All the software was written in LabView on a Dell windows workstation.

In order to test the data delivery system, we have built an experimental setup as shown in figure 6(a). Light from a Helium-Neon laser is collimated and directed onto the GLV™. A lens is used to focus the 1st order diffracted beam onto a detector. We send data to the GLV™ and measure the modulation of the light on the detector. Figure 6(b) shows the detector signal as a function of time when the GLV™ was driven with “ON-OFF” data at a frequency of 7.5 kHz (the specification required for our prototype system), corresponding to an average data transfer rate of 130 Mbits/s. The vertical axis is the detector voltage, but it was not calibrated and hence is not labeled in the figure.

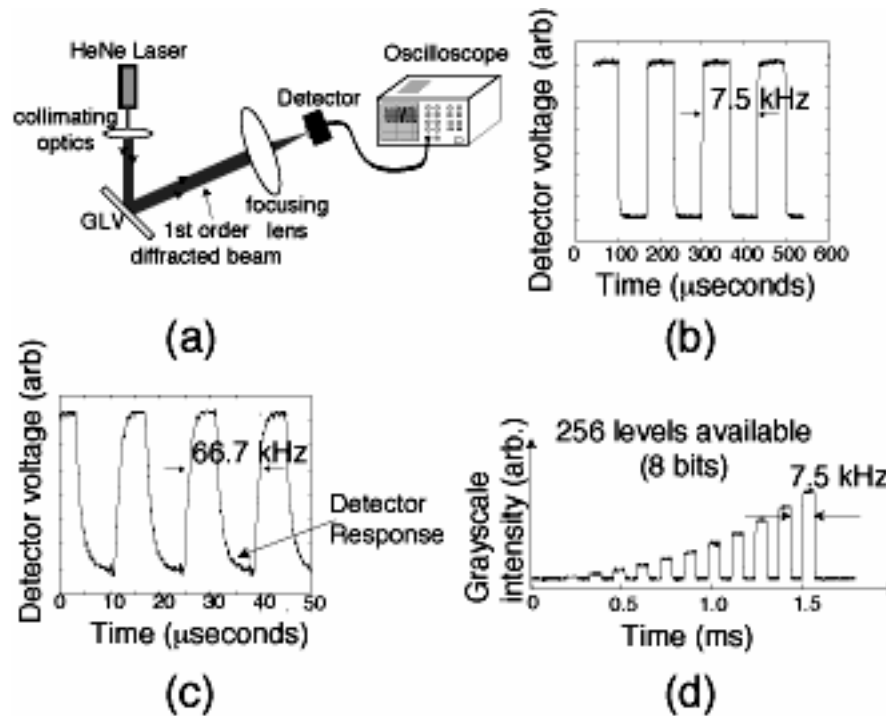


Figure 6(a): Schematic of the experimental setup for testing the data delivery system for ZPAL.
(b) The GLV operating at 7.5 kHz, the required speed for our prototype system. **(c)** The GLV operating at 66.67 kHz, corresponding to a 1Gbit/sec data rate. **(d)** Grayscale at 7.5 kHz

Since the GLV™ is capable of operating at much higher frequencies (~500 kHz), we tested our system to determine the limits of the data delivery architecture, even though our requirements had been successfully met. Figure 6(c) shows the GLV™ operating at a frequency of 66.67 kHz, corresponding to a data transfer rate of about 1Gbit/s. At present we were limited by the response time of our detector, but data from our logic analyzer indicates that we can successfully send rates in excess of 100 kHz with our current implementation. Since dose control is an important requirement for good lithographic performance, the ability to grayscale is paramount in any multiplexing device to be employed in a ZPAL system. The GLV™ offers 8-bits of grayscale (256 levels), 3 bits more than what is needed for our writing strategy, which requires 5-bits. As shown in figure 6(d), our data-delivery system is capable of achieving all 8-bits of grayscale without sacrificing switching speed.

8. Zone-Plate-Array Lithography (ZPAL): Lithographic Performance

Sponsors

Defense Advanced Research Projects Agency and Army Research Office
Grant No. DAAD19-01-1-0330

Project Staff

Dario Gil, Rajesh Menon, Amil Patel, and Professor Henry I. Smith

In a direct-write system such as ZPAL, the major figures-of-merit are resolution and contrast. The resolution is quantified by the following equation:

$$w_{\min} = k_1 \lambda / NA \quad (1)$$

where w_{\min} is the minimum feature size, NA is the numerical aperture of the zone plate, λ is the exposure wavelength and k_1 is a proportionality factor that, in effect, indicates how close to theoretical limits one operates.

In order to reduce the minimum feature size, one can increase the NA of the zone plates. The results presented in figure 1, using $NA=0.9$, are the highest quality lithographic patterns ever produced with ZPAL, showing good fidelity, low edge roughness, and the ability to pattern very dense features down to the minimum spot size. It is worth noting that since all exposed pixels received the same dose, proximity effects are minimal in the exposures.

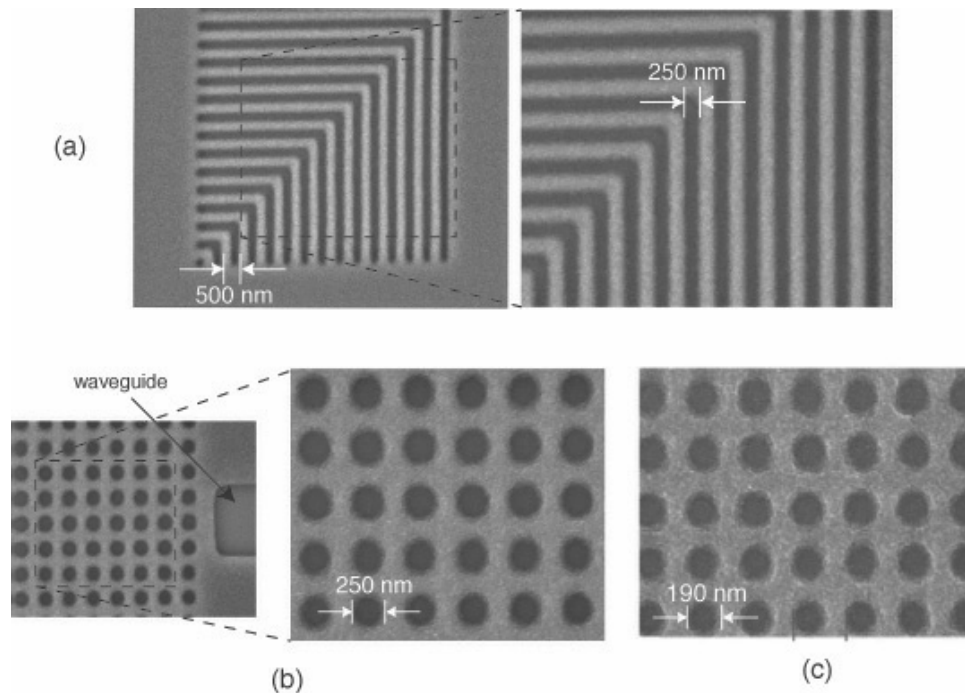


Figure 1: Scanning electron micrographs of patterns exposed with our continuous-scan 0.9 NA UV-ZPAL system operating at $\lambda = 400\text{nm}$. (a) Dense nested Ls, (b) 2D photonic bandgap structures with 500 nm period, (c) 2D photonic bandgap structures with 360 nm period.

The ability to pattern curved structures and non-manhattan geometries is important for a number of applications, and our ZPAL system, by employing sub-pixel stepping, can satisfy these needs, as illustrated in figure 2.

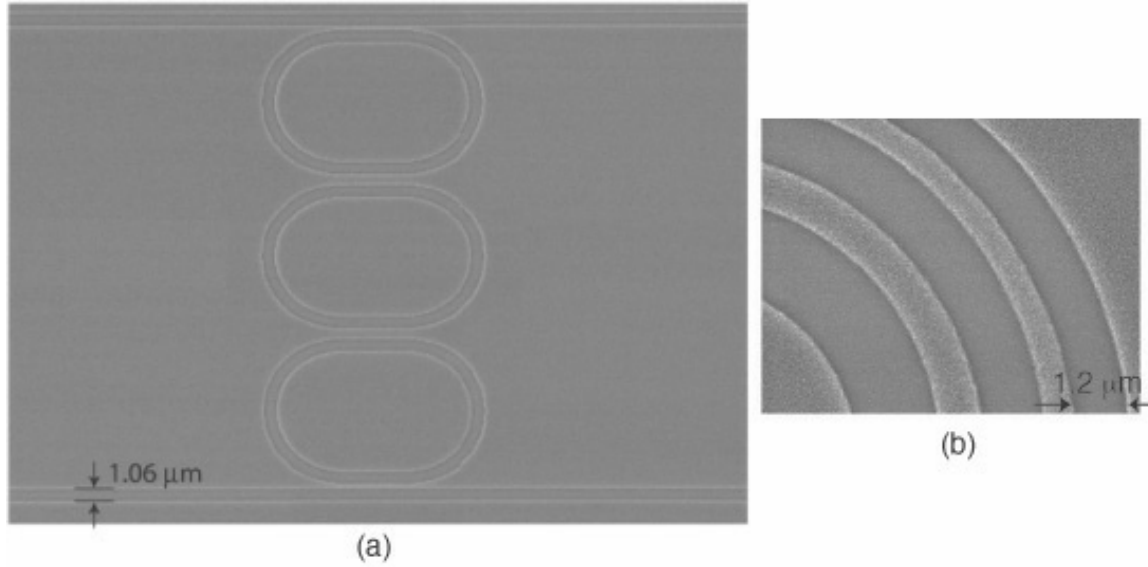


Figure 2: Scanning electron micrographs of patterns exposed with our continuous-scan 0.9 NA UV-ZPAL system operating at $\lambda = 400\text{nm}$. Sub-pixel stepping enables patterning of curved structures with smooth edges. (a) waveguides with ring resonators, (b) one quadrant of a zone plate.

The minimum feature size can be further reduced by reducing k_1 . This corresponds to decreasing the size of the address grid, as illustrated in figure 3.

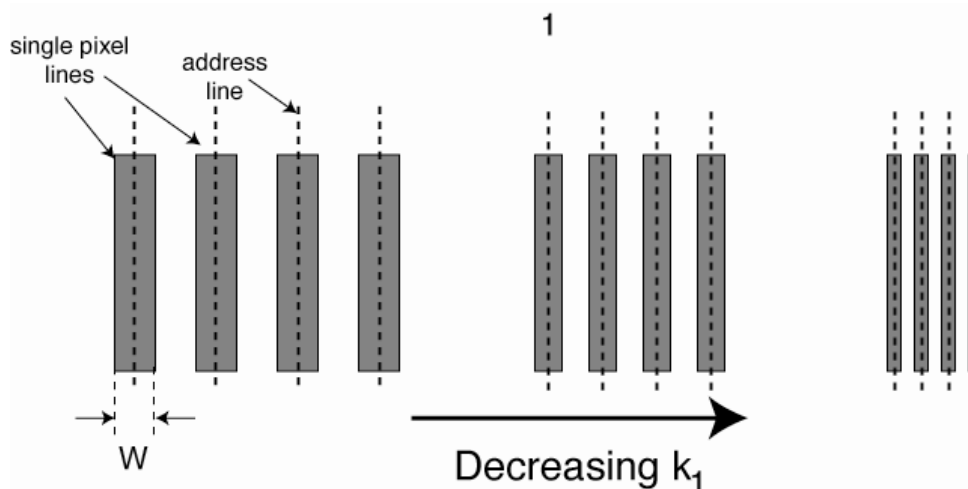


Figure 3: k_1 in ZPAL. Decreasing k_1 decreases the minimum feature size. This is done by decreasing the address grid of the system i.e. the scan lines of the focused spot are brought closer together as shown. At some point, the final image will not have sufficient contrast to be resolved by the photoresist. That point determines the limiting k_1 factor.

Figure 4 shows a set of scanning electron micrographs of dense lines and spaces with varying k_1 's, from 0.56 to 0.38. We are currently exploring the limits of how much lower we can go, since even at $k_1 = 0.38$ the quality of the patterning remains remarkable. Systematic characterization of lithographic exposures has also allowed us to determine that the process latitude for our current system is around 13% (even when operating at $k_1 = 0.38$). We believe the superior lithographic performance of ZPAL is connected with the fact that there is no phase relationship between sequentially exposed spots (i.e., incoherent imaging).

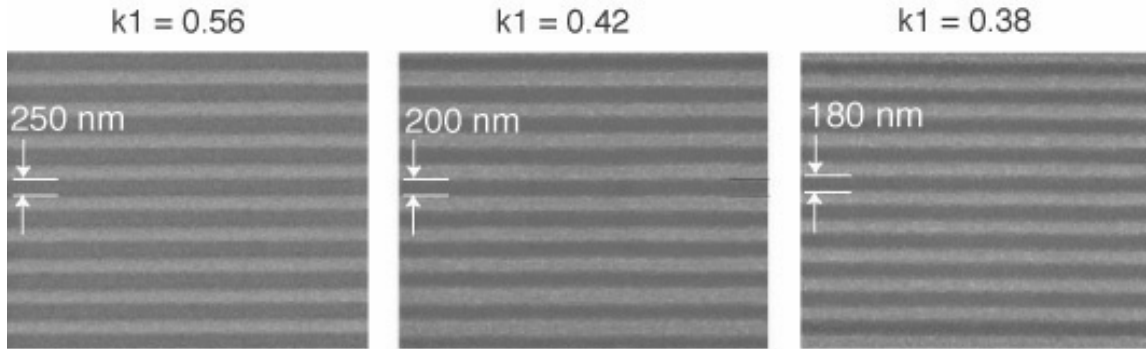


Figure 4: Exploring the limits of k_1 with ZPAL. High-numerical-aperture zone plates (0.85 and 0.9) can operate at low k_1 factors (below 0.4). Sub-70 nm patterning should be possible, by operating at the demonstrated $k_1=0.39$, with 0.9NA zone plates and $\lambda = 157\text{nm}$.

Image contrast is an important lithographic-figure-of-merit. This is particularly important since phase zone plates have higher (odd) diffraction orders which contribute to the background. Here, we show that large area patterning is indeed possible with zone plates, even without order-sorting apertures, and at very high numerical apertures.

For evaluating contrast, it is sufficient to pattern full fields at the maximum resolution. Figure 5 demonstrates that full fields of dense lines and spaces can be written with high-NA zone plates. The top of the figure provides a schematic of ZPAL (without the micromechanics) illustrating the concept of parallel writing by stitching multiple fields. The bottom of the figure contains an experimental result in which we exposed fields of $125\mu\text{m} \times 125\mu\text{m}$ (currently the scanning limit of our stage) with a 0.9 NA zone plate operating at $\lambda=400\text{nm}$ and a focal length of $40\mu\text{m}$. A field of $125\mu\text{m} \times 125\mu\text{m}$ corresponds to the area under a 0.85 NA zone plate, as indicated in the figure. The exposed pattern consists of 1:1 dense lines and spaces with a period of 440nm. The zoomed in scanning-electron micrograph of the bottom-right of figure 5 provides a clear view of what the pattern looks like, namely a 440nm-period dense 1:1 grating.

In summary, our results provide hard evidence that high-numerical-aperture zone plates are capable of providing sufficient contrast for state-of-the-art lithography. Although multiple diffracted orders exist, the background exposure that they produce is not deleterious. Moreover, the background can be further reduced by the utilization of order-sorting apertures.

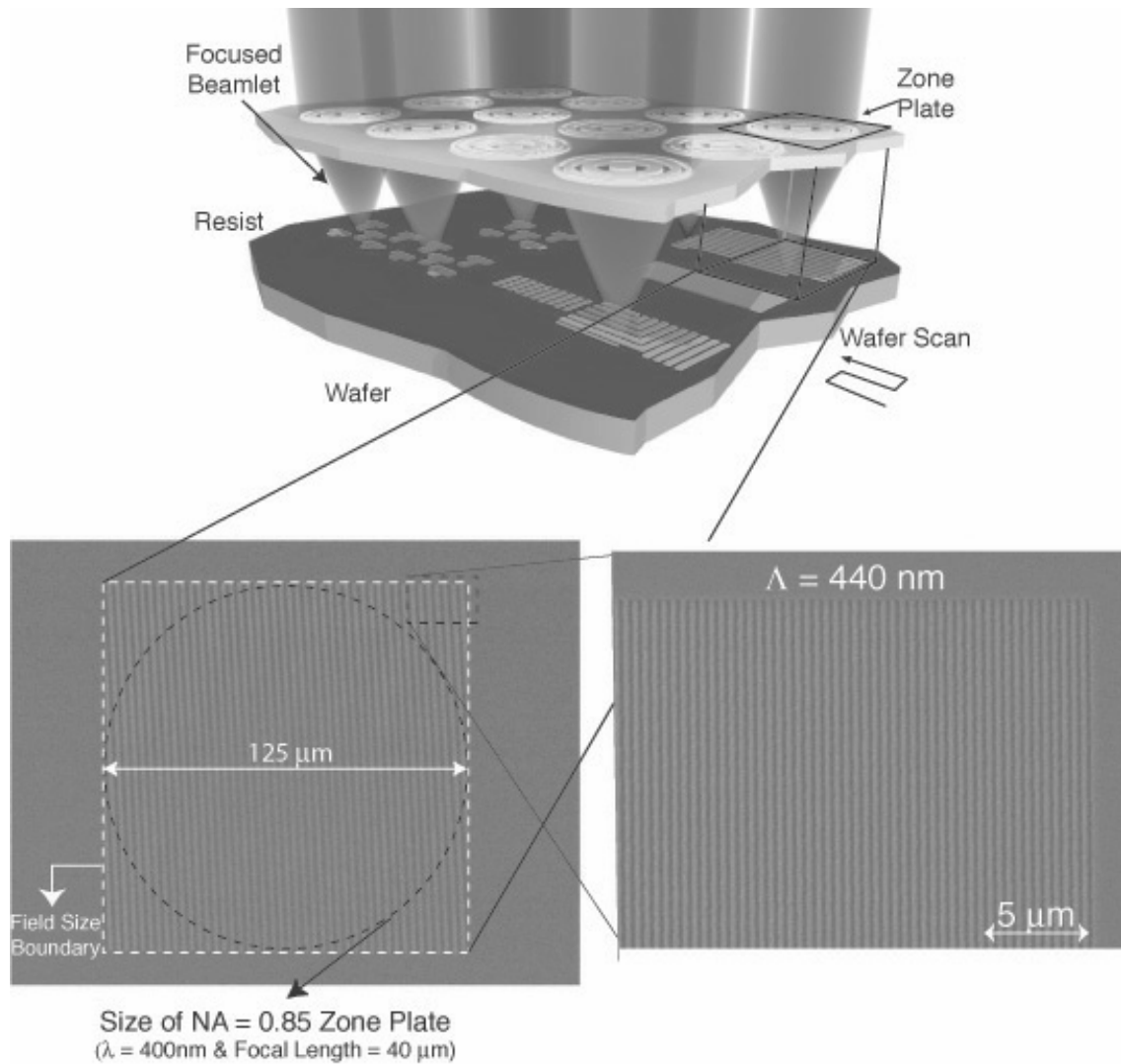


Figure 5: Top: Schematic of the ZPAL system without the micromechanics. Large-area patterns are created by stitching adjacent fields, with a field defined as the square area located underneath any given zone plate. Bottom-left: Proof that full-field patterning is possible with ZPAL despite the existence of multiple orders. A dense 1:1, 440nm-period grating was exposed (with 400nm wavelength) covering the area of a 0.85 NA zone plate. Note that the inclined periodicity ($\sim 3\mu\text{m}$ period) observed in the left scanning-electron micrograph is the result of a moiré effect (resulting from the beating of the periodic sampling of the SEM with which the picture was acquired and the periodicity of the exposed grating). Bottom-right: Zoomed in SEM of the top-right corner of the large area grating.

9. **Fabricating Advanced Microsystems with Conformable-Contact Photolithography**

Sponsor

Defense Advanced Research Projects Agency/Navy Grant N66001-00-1-8932

Project Staff

James Daley, Dr. James G. Goodberlet, Dr. Hamide Kavak, Dr. V.H.S. Moorthy and Professor Henry I. Smith

The goal of this research program is to apply conformable-contact photolithography (CCP) to the fabrication of novel or technologically advanced sub-micron devices. In a previous program under the same sponsor, it was shown that CCP enables low-cost, sub-100-nm patterning with sub-100-nm overlay capability. A particular thrust of this program is to use CCP in the development of a novel integrated photomultiplier termed the “microphotomultiplier.” This device would enable on-chip, ultrasensitive and ultrafast photodetection for potential applications in optical, biochemical sensing, communications or low-light-level imaging technologies. Also during this program, the CCP technology has been transferred to a company that is developing grating-based, integrated-optical devices for signal multiplexing/demultiplexing, and to a foreign university with an active program in near-field photolithography. Additionally, a local company has begun manufacturing equipment to make CCP available to universities or small businesses with interests in deep sub-micron patterning but constrained by limited budgets.

The microphotomultiplier, illustrated in Figure 1 and described in last year’s report, poses several fabrication challenges. Long, deep, narrow channels, which provide electron amplification, must be patterned and etched into the substrate. Channels with high aspect ratio, defined as length divided by width, provide greater electron multiplication or device gain and are preferred. To reduce the overall size of the device, and reduce the difficulty in sealing the channels for vacuum operation, narrower channels are preferred. After etching the channels, the walls must be coated with a resistive film that enhances secondary electron emission and prevents their charging. Further, a photocathode must be fabricated at one end, and two closely-spaced electrodes, the anode and signal collector (not shown in the figure), defined at the opposite end to enable photodetection, device bias, and signal detection.

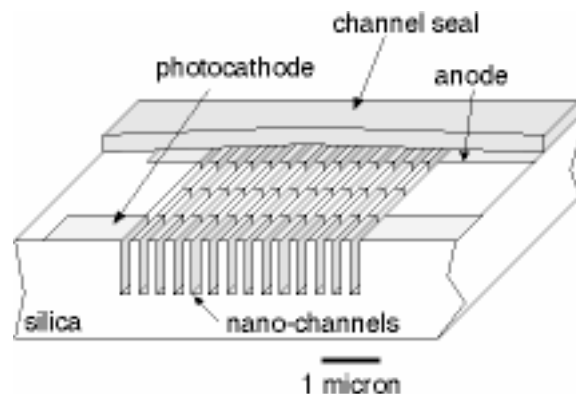


Figure 1. This cut-away illustration of the integrated microphotomultiplier shows the electron-amplifying channels and device electrodes. This device offers the promise of ultrasensitive and ultrafast photodetection in a micro-scale package.

For the first fabrication attempts the microphotomultiplier's channel width was chosen to be about 125 nm, and several device lengths, ranging from about 3 μm to 50 μm were trialed. There were typically 200 or more channels in a single device. The channels were defined in the first level of lithography and subsequently etched into an oxide substrate. In the second level of lithography, a resistive strip was aligned to the channels with better than 200 nm overlay accuracy. (In a separate alignment evaluation experiment, it was shown that sub-50-nm overlay accuracy could be achieved.) Amorphous silicon was deposited to define the resistive strip. In a third level of lithography and subsequent processing, the photocathode, anode and signal collector were defined in gold. The use of gold enabled photoemission, at short-wavelength radiation, and would not rapidly degrade upon exposure to air. The anode was spaced about 800 nm from the signal collector. A prototype device, fabricated through these three levels of lithography is shown in Figure 2. All levels of patterning and alignment were done using CCP techniques.

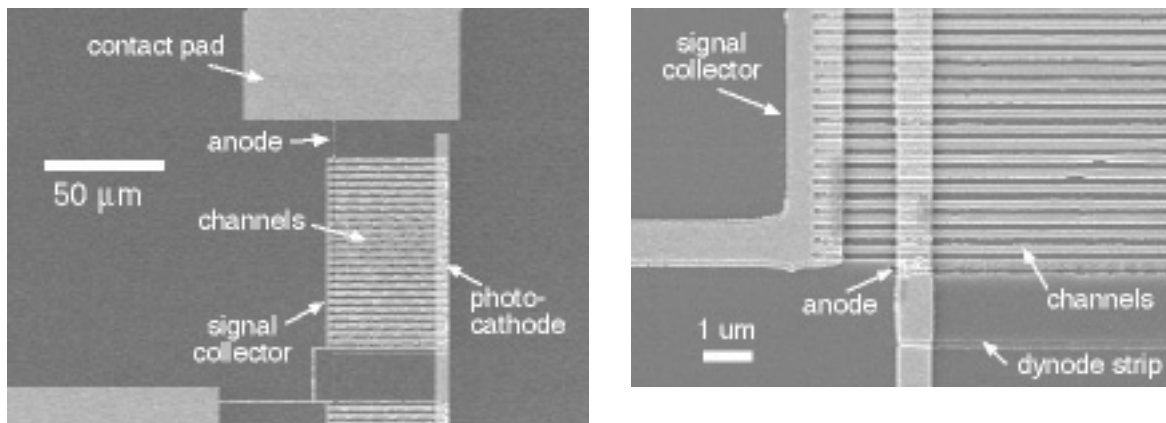


Figure 2. These SEM images show a prototype microphotomultiplier. Three levels of conformable-contact photolithography, which includes two aligned levels, were carried out in fabricating this device. A large-area view is shown in (a), and a close-up view of the lower left corner of the device is shown in (b).

Preliminary device testing was carried out in a small, custom-built vacuum chamber that housed contact probes and positioning stages. Devices were illuminated with a deep ultraviolet radiation source located outside the chamber. Four initial measurements were carried out to test for (1) resistivity of the amorphous silicon, (2) photoconduction between the photocathode and anode, (3) electrical breakdown when high voltage is applied between the cathode and anode, and (4) continuity of electrode leads across the narrow channels. The first three tests were carried out on test devices located on flat surfaces, i.e. without the presence of the channels, and the last test was carried out with the channels present.

The results from the resistivity measurement yielded 31 $\text{M}\Omega\text{-cm}$ for the strip. The measured resistivity was four orders of magnitude higher than expected and reported in other work. [J. Sangrador, et al, *Thin Solid Films* 125 (1985) 79.] This is believed to be due to poor e-beam deposition conditions. In our deposition chamber, the base pressure was 10^{-5} Torr, and we expected the dynode strip to be rich in oxide. Photoconduction was readily measured between the photocathode and anode, and is graphed in Figure 3. For this measurement, the device was illuminated with a small pencil lamp, $\lambda = 253 \text{ nm}$, while a +9V bias was applied to the signal collector. The graph reports the measured photocurrent from cathode to anode as a function of time. The change in photocurrent, despite constant illumination intensity, is due to surface contamination effects on the photocathode, and has been observed in similar work with gold photocathodes. [S. Gosavi et al, *J. Vac. Sci. Technol. B* 19 (2001) 2591.] The amount of photocurrent suggested a quantum efficiency in the 10^{-3} range for gold which agrees with previously reported values. [A. H. Sommer, *Photoemissive Materials*, John Wiley & Sons, Inc.,

New York, NY (1968) 33.] Measurements of breakdown voltage showed an average device failure about 500V bias, based upon testing of eight devices. This result was encouraging, because sufficient device gain would be expected at such a high potential along the amplifying channels. The results from the continuity measurements showed no devices with continuous electrical leads across the narrow channels. This problem, which precluded further testing, was traced to a lithographic error at the edge of the channel regions. By augmenting fabrication procedures, this problem can be eliminated and future prototype devices can be fully demonstrated.

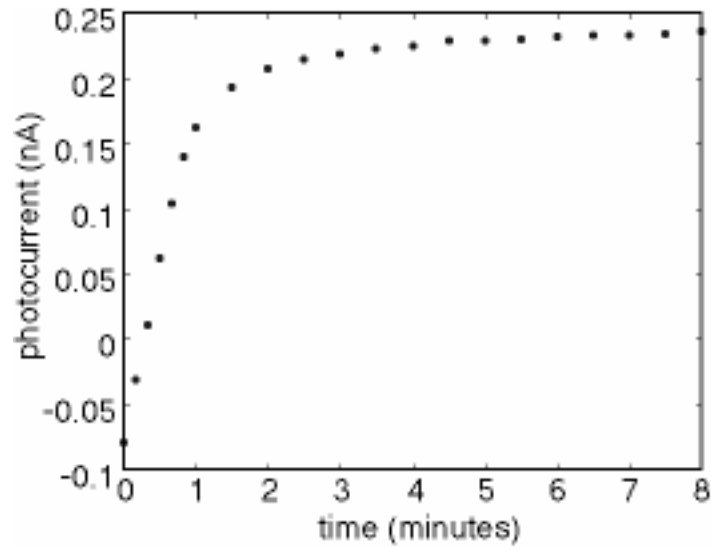


Figure 3. The typical photocurrent measured in test devices shows an increase with time. This is due to a reduction of surface contamination at the photocathode.

A secondary objective of this research program was to extend conformable-contact photolithography to other microfabrication applications. Accordingly, the technology has been successfully transferred to a California-based company that is developing a novel integrated-optical mux/demux device. This company has patterned 500-nm-pitch gratings and micron-sized waveguides, and successfully implemented multi-level alignment using CCP techniques. Mask making procedures, a critical component to CCP, were transferred to the University of Canterbury in Christchurch, New Zealand where an active research program in near-field photolithography is ongoing. Additionally, a local company has begun manufacturing conformable-contact photolithography equipment which will enable low-cost pattern replication and multi-level alignment at the sub-200-nm level.

10. Interference Lithography

Sponsors:

Defense Advanced Research Projects Agency and U.S. Army Research Office –
Grant DAAD19-99-1-0280

Project Staff:

James M. Carter, Robert C. Fleming, Timothy A. Savas, Michael E. Walsh, Thomas B. O'Reilly,
Dr. Mark L. Schattenburg, and Professor Henry I. Smith

Interference lithography (IL) is the preferred method for fabricating periodic and quasi-periodic patterns that must be spatially coherent over large areas. IL is a conceptually simple process where two coherent beams interfere to produce a standing wave, which can be recorded in a photoresist. The spatial-period of the grating can be as low as half the wavelength of the interfering light, allowing for structures of the order of 100nm from UV wavelengths, and features as small as 30-40 nm are possible using a DUV ArF laser.

The NanoStructures Lab has been developing IL technology for close to 20 years, and we currently operate 4 different IL systems for a wide variety of applications. One system, shown schematically in Figure 1, is run in cooperation with the Space Nanotechnology Lab. This system is specially designed for high stability and repeatability and is capable of producing metrological quality gratings and grids up to 10 cm in diameter at spatial periods down to 200nm. Used primarily for satellite applications, gratings produced with this tool have flown on numerous missions, most notably, the Chandra x-ray astronomy satellite launched in August of 1999 included hundreds of matched, high-precision gratings.

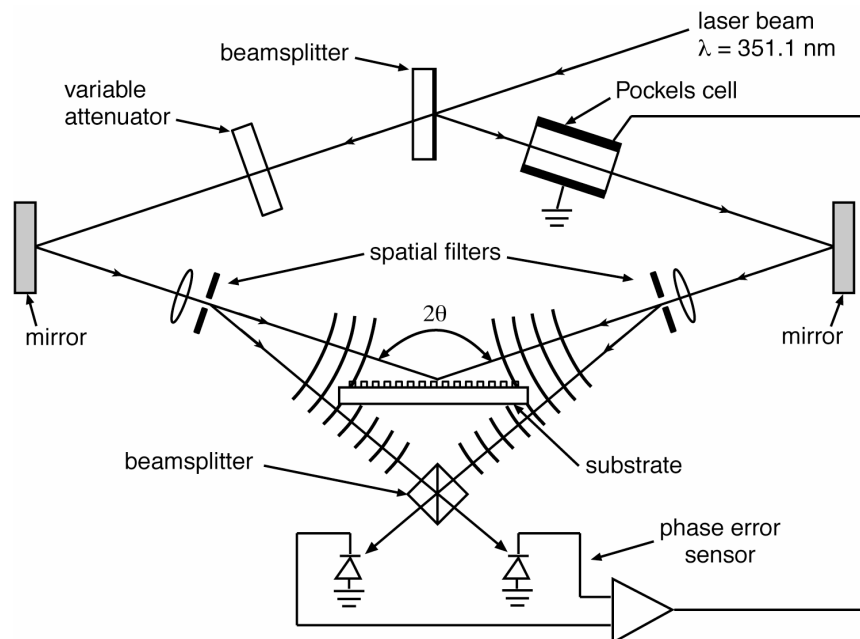


Figure 1. Schematic of one of the MIT interferometric lithography systems. This system occupies a 2x3m optical bench in a class 100 clean environment. The beamsplitter directs portions of the two interfering spherical beams to photodiodes. A feedback locking is achieved by differentially amplifying the photodiode signals and applying a correction to the Pockels cell which phase shifts one of the beams in order to stabilize the standing wave pattern at the substrate.

We operate another system similar to the one shown in Figure 1 based around the 325 nm line of a HeCd laser. This system functions both as an exposure tool with capabilities comparable to those described above as well as an analysis tool. Using a technique known as holographic phase-shifting interferometry (HPSI), the linearity and spatial phase of gratings produced in this system can be quantitatively measured and mapped with an accuracy on the order of parts per million. Known hyperbolic distortions in the spatial-phase of gratings printed using IL are responsible for changes in periodicity of a few angstroms (for a 200nm period grating) over a 10 cm wafer. Although seemingly small, distortions of this scale can be highly significant, especially in metrological applications such as the fiducial grids for spatial-phase locked electron beam lithography. Using the HPSI, we have been able to investigate innovative techniques for reducing these distortion levels. One method, based on the controlled bending of the substrate during exposure, has demonstrated a reduction of the distortion pattern from 2 dimensions to 1 dimension as well as reducing the magnitude of the distortions by about a factor of 5.

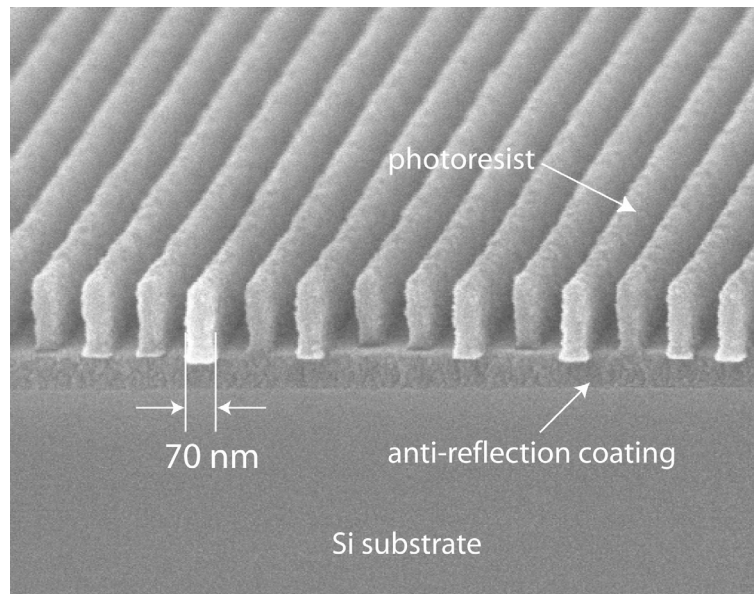
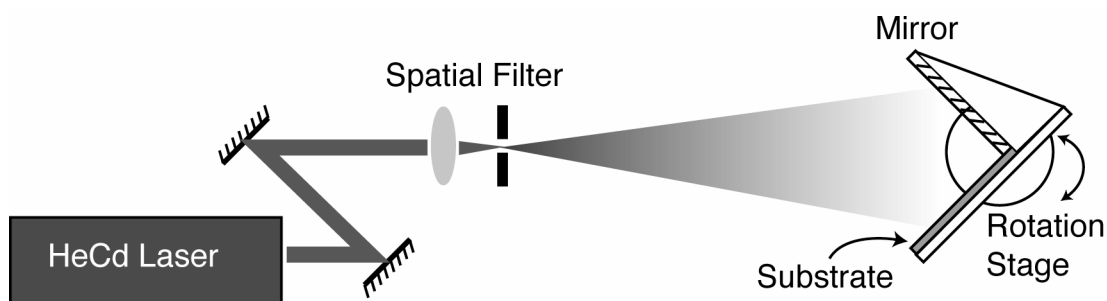


Figure 2: Schematic of a Lloyds-mirror interferometer. The substrate and mirror are fixed at a 90° angle to one another, and centered in a single incident beam. Rotating the substrate/mirror assembly about its center point varies the spatial-period of the exposed grating. The micrograph shows a grating with 70 nm lines on a 170 nm pitch exposed using the Lloyds-mirror.

Also utilizing a 325 nm HeCd laser is the Lloyds-mirror interferometer, shown schematically in Figure 2. The primary advantage of the Lloyds-mirror is that the spatial-period of the exposed gratings can be easily and continuously varied from many microns down to ~170 nm simply by rotating the stage without realigning the optical path. This has opened the door to new possibilities such as varied aspect-ratio grids (different periodicities in the two axes of the grid) for patterned magnetic media and MRAM (magnetic random access memory) devices. Among the many other applications of IL supported by the Lloyds-mirror are alignment templates for organic crystals and block co-polymers, semiconductor quantum dots, and other self-assembling structures. Distributed feedback (DFB) structures for quantum dot lasers and photonic bandgap devices have also been made using the Lloyds mirror.

For spatial periods of the order of 100 nm, we use a 193 nm ArF laser. To compensate for the limited temporal coherence of the source, we utilize an achromatic scheme shown in Figure 3. In this configuration the spatial period of the printed grating is dependent only on the period of the parent gratings used in the interferometer, regardless of the optical path or the wavelength and coherence of the source. Thus, gratings and grids produced with this tool are extremely repeatable. Figure 4 shows a 100 nm-period grid of 13 nm-diameter posts etched into Si, produced using achromatic interferometric lithography (AIL) and a sequence of etching steps. Other applications AIL include patterned magnetic media, gratings for atom-beam interferometry UV polarizers, and templated self-assembly.

A new generation of achromatic interference lithography tools is currently being developed to produce 50 nm period gratings and grids, or 25 nm lines and spaces. Because of the limited availability of sub-100nm wavelength sources, all of the possible implementations for making 50 nm period gratings are based around the achromatic scheme described for 100 nm period gratings. Among the possibilities are free-standing gratings etched in a thin membrane for use with soft x-rays, or use of reflection gratings in an analogous AIL scheme with a 58.4 nm helium discharge.

The fourth type of interference lithography is scanning-beam interference lithography (SBIL). Such a system, which is also called the Nanoruler, has been constructed in the Space Nanotechnology Laboratory, and is described in another section.

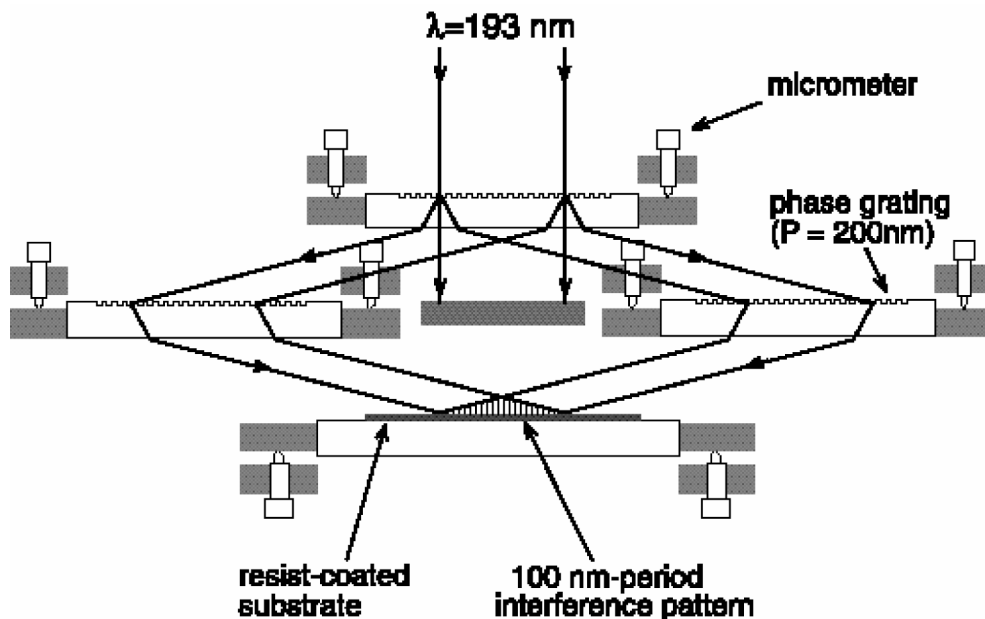
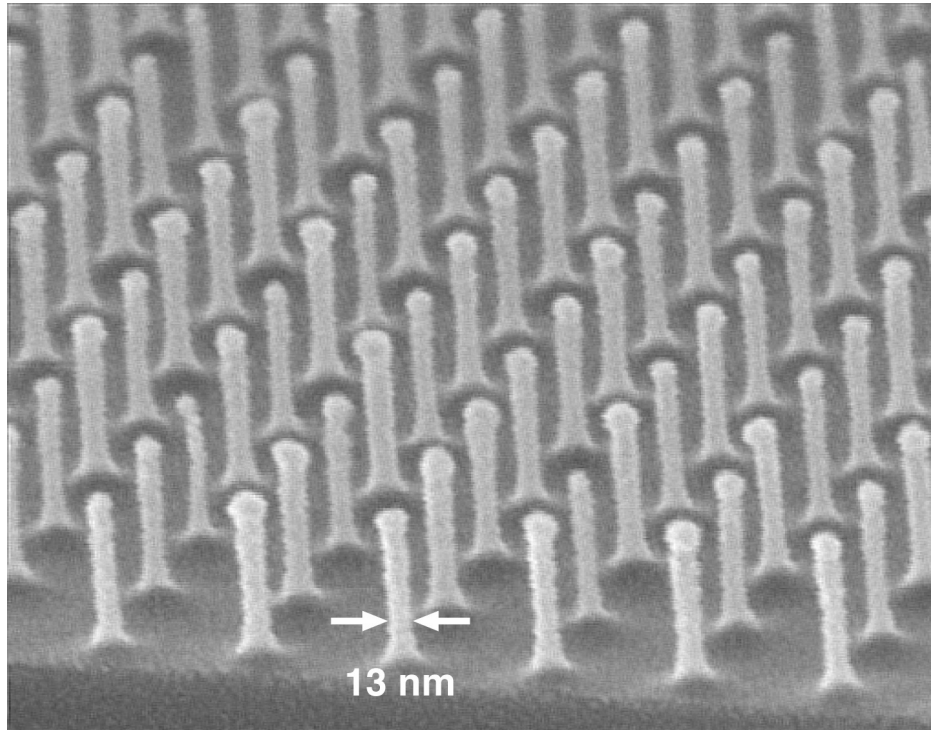


Figure 3. Achromatic interferometric lithography (AIL) configuration employed to produce 100 nm-period gratings and grids.



100nm-period posts in Si

Figure 4: Scanning electron micrograph of a 100 nm-period grid, exposed in PMMA on top of an antireflection coating, and transferred into Si by reactive ion etching.

11. The MIT Nanoruler: A Tool for Patterning Nano-Accurate Gratings.

Project Staff:

C. Chen, C.-H. Chang, C. Joo, P. Konkola, J. Montoya, Dr. R. Heilmann
(Dr. Mark L. Schattenburg and Prof. Henry I. Smith)

Sponsors:

Defence Advanced Research Projects Agency /Army Research Office (DAAD19-02-1-0204),
NASA (NAG5-5405)

Historically, the ability to observe and measure the results of processes has been critical to advancing fabrication technology. Thus, improvements in optical microscopy (e.g., Nomarski differential interference contrast) were a key enabler of the microelectronics revolution. In turn, the scanning-electron and atomic-force microscopes are essential tools as we move into the nanotechnology era. While the ability to print or resolve a particular feature size is a necessary condition for the successful lithographic manufacturing of nanosystems, it is, by no means, the only requirement. Equally important is the ability to measure and control the size and placement of lithographic features with very high accuracy

All modern lithographic production and inspection tools, and all precision tools for that matter, are based on the notion of a *metrology frame*. Such a frame is composed of three components: (1) a rigid mechanical structure, (2) means to measure the motion of a workpiece with respect to the metrology frame, and (3) means to project, image or detect patterns on the workpiece, such as by use of an optical or electron lens. The preferred means for measuring workpiece motion has been the laser interferometer. The accuracy of a lithographic tool is critically dependant on the accuracy of its metrology frame, which, in turn, is dependant on the accuracy of the interferometer. Due to a number of complex factors, however, interferometer accuracy is not keeping pace with the shrinking tolerances as called for by the semiconductor industry roadmap (see Fig. 1) and the future nanotechnology revolution.

To address this problem, we are developing a lithographic tool called the *Nanoruler* that is designed to pattern gratings of such high accuracy that they may serve as the means for detecting workpiece motion in precision tools, using a method known as optical encoding, with an accuracy that is some 10-100X better than laser interferometers. The Nanoruler utilizes a patterning method called *scanning-beam-interference lithography* (SBIL), developed in the Space Nanotechnology Laboratory (SNL), that is capable of rapidly patterning large gratings (>300 mm diameter) in only a few minutes with unprecedented accuracy (see Fig. 2). Such super-accurate gratings can serve as optical encoder plates, as mentioned. Another important application for the Nanoruler is the patterning of nano-accurate gratings necessary for locking an electron beam using a novel technique called spatial-phase locked electron beam lithography (SPLEBL) that is under development in the NanoStructures Laboratory (NSL) and described elsewhere.

High fidelity gratings are also critical for advanced instrumentation and optics such as laboratory and astronomical spectrographs, high-bandwidth optical communications and fusion energy research. Conventional means of fabricating gratings, such as diamond ruling, holography, or beam writing, can take many hours or weeks to complete, and typically produce gratings of poor spatial-phase fidelity.

The concept of SBIL is to combine the sub-1 nm displacement-measuring capability of laser interferometry to control a high-performance air-bearing stage, with the interference of narrow coherent beams, to produce coherent, large-area, linear gratings and grids. Our ultimate goal is to produce gratings with sub-nm distortion over areas many tens of centimeters in diameter. SBIL requires sophisticated environmental controls to mitigate the effects of disturbances such as acoustics, vibration, and air turbulence, and variations of temperature, pressure, and humidity.

22 – **Nanostructures** – Nanostructures Technology, Research and Applications – 22
RLE Progress Report 145

The system also features real-time measurement and control of optical phase using heterodyne fringe detection, acousto-optic modulator phase locking (see Fig. 3), and a high-speed digital signal processor (DSP) controller (see Fig. 4).

An important feature of SBIL is the ability to both write and read gratings with nanometer control of grating phase. Fig. 5 is a map of phase error for a grating that was first written in the Nanoruler, developed, and then placed back into the tool and read. The data demonstrates ~2 nm 3 σ repeatability of the writing/reading process, which includes errors due to substrate chucking/unchucking.

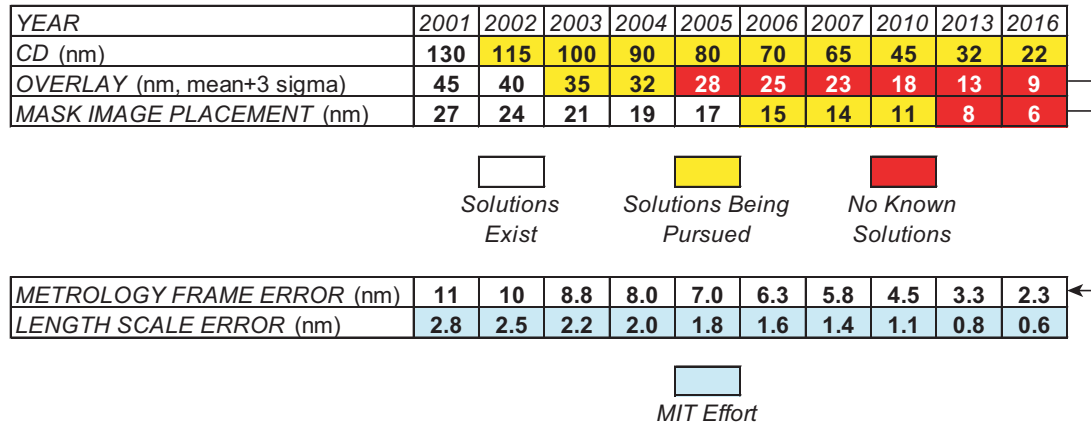


Figure 1. Semiconductor Industry Association (SIA) roadmap tracking critical dimension (CD) or minimum feature size, overlay error, mask image placement error, and metrology tool error. The MIT effort seeks to produce grating metrology standards with sub-nm errors, which would be used as planar metrology length scales or optical encoders in lithographic and other equipment, eliminating the laser interferometer.

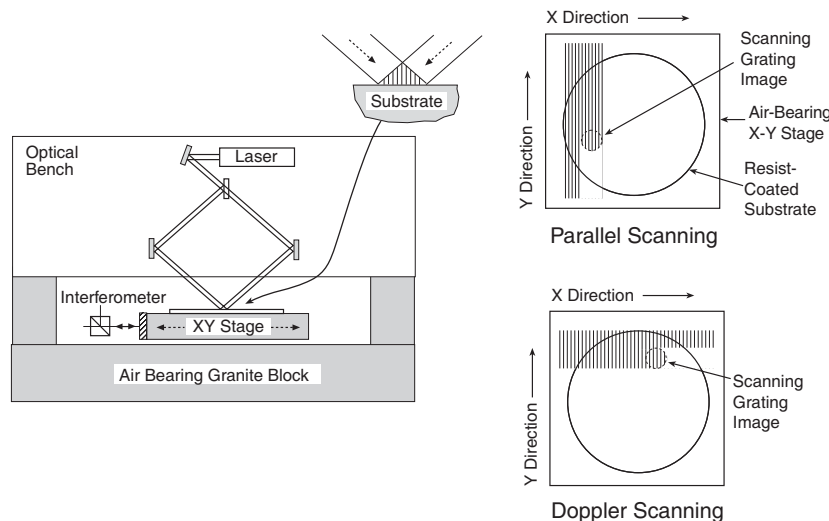


Figure 2. Schematic of the scanning-beam-interference-lithography (SBIL) system under development in the SNL. A pair of narrow, low-distortion beams overlap and interfere at the substrate, producing a small grating “image.” The substrate is moved under the beams, writing a large area grating. Tightly overlapped scans ensure a uniform dose.

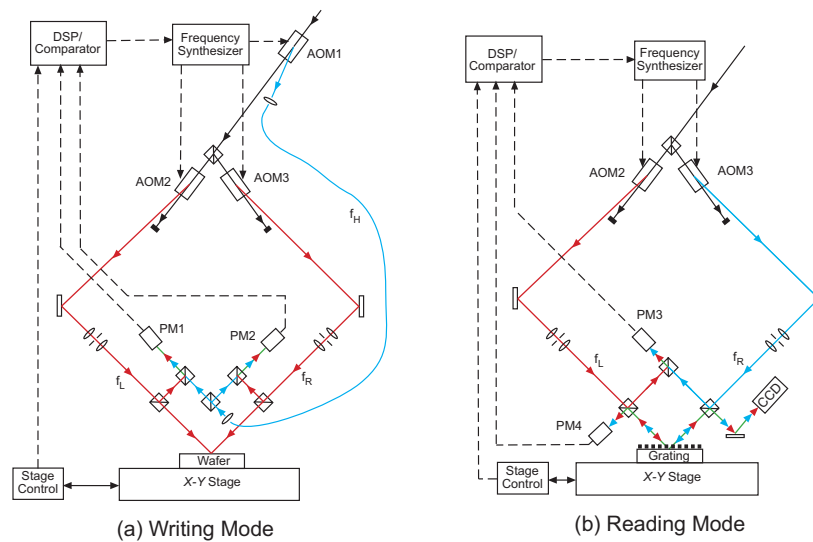


Figure 3. Schematic of SBIL acousto-optic (AO) modulator phase locking system. Both writing and reading modes are depicted. The phase of the grating image is measured by a small interferometer close to the writing surface. The AO modulators Doppler shift the beams into the megaHertz range, providing high-accuracy heterodyne measurement of phase. This information is processed by a digital signal processor and used to control RF frequency synthesizers which drive the AO modulators, thus locking the image phase to the moving substrate.

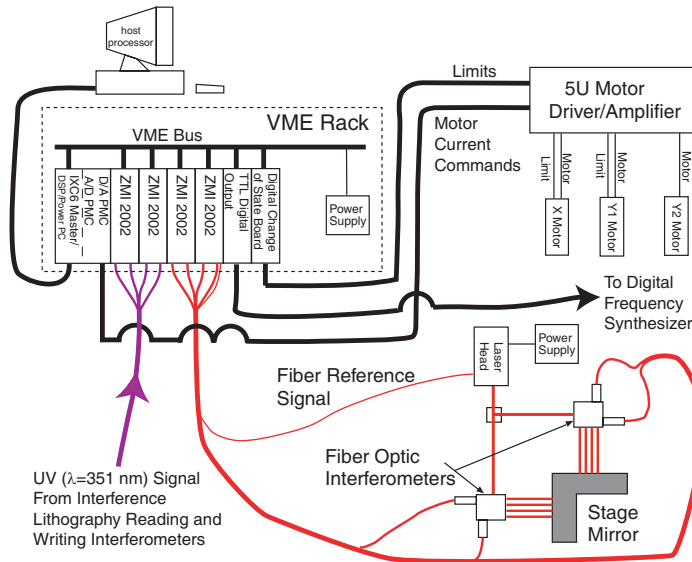


Figure 4. Schematic of SBIL system control architecture. The system utilizes a frequency stabilized HeNe laser ($\lambda=632.8$ nm) and heterodyne interferometry to measure substrate position, and argon ion laser ($\lambda=351.1$) heterodyne interferometry to measure image fringe phase. Phase error signals are processed by an IXTHOS 4x167 MHz DSP board which then drives the stage DC motors and the RF digital frequency synthesizer controlling the fringe-locking AO modulators.

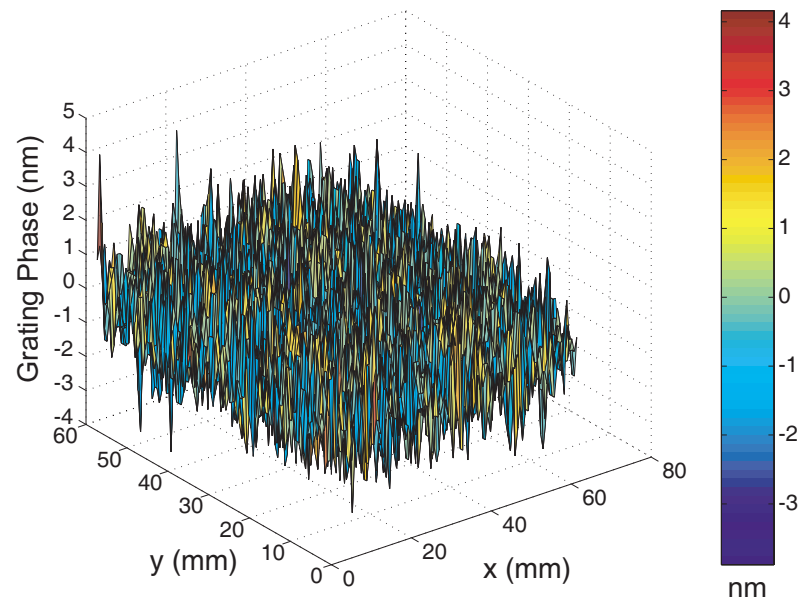


Figure 5. Wafer phase mapping repeatability (nm), for a 400 nm-period grating that was written and then read by the Nanoruler.

12. Interference Lithography for Patterning Variable-Period Gratings

Project Staff

C. Chen, C.-H. Chang, C. Joo, P. Konkola, J. Montoya, Dr. R. Heilmann
(Dr. Mark L. Schattenburg)

Sponsor

NASA (Grant NAG5-12583)

Scanning-beam-interference lithography (SBIL) patterns large-area, linear, low-phase-distortion gratings with a pair of small diameter (millimeter size) phase-locked laser beams. We are developing a prototype system that generalizes the concept of phase-locked scanning beams for patterning continuously varying (chirped or quasi-periodic) patterns. These structures can subsequently be used to fabricate chirped x-ray reflection gratings for astronomical imaging applications, chirped fiber Bragg gratings for time-delay or spectral filtering applications, and/or diffractive optical elements.

Figure 1 shows the experimental diagram of the variable-period scanning-beam interference-lithography (VP-SBIL) system. For controlling the grating period and orientation, the system employs dual-axis picomotor-driven gimbal mirrors to produce symmetric deflections of a pair of interfering beams around the optical axis without translation. Two objective plano-convex lenses ($f\# = 4.25, 2.12$) are used in a 4-f optical configuration. Such a lens system allows the conjugate points of beam deflection (on mirrors) to overlap at the focal plane of the second objective lens. The spot size of image overlap is reduced to half the beam diameter as the ratio of focal lengths $f_2/f_1=0.5$. This relaxes the maximum period variation ($\Delta\Lambda$) constraint over the image diameter (D) that requires $\Delta\Lambda/\Lambda \ll \Lambda/D$ where Λ is the grating period.

To attain phase stability during grating patterning, homodyne fringe locking is adopted using an imaging detector, analog fringe-locker and a piezo-actuated mirror in closed-loop. In the present experimental configuration, two-axis beam rotation can generate any fringe orientation. However, variation in grating period (~ 1000 to $2 \mu\text{m}$) is limited by the range of deflection produced by the gimbal mirrors ($\pm 10^\circ$) and by the numerical aperture (NA) of the lens system. Using position-sensitive detectors with an appropriate imaging and Fourier lens configuration, closed-loop beam steering is implemented to vary the grating period and orientation in a predetermined fashion. Typical requirements for x-ray reflection grating fabrication are $\Lambda_{\text{ave}} \sim 2 \mu\text{m}$ and chirp factor $\Delta\Lambda/\Lambda \sim 5\%$.

Fig. 2 shows two grating images of period $2.0 \mu\text{m}$ and $4.0 \mu\text{m}$ obtained on a static substrate by changing the angle between the beams using the picomotor-controlled gimbal mirrors. Line uniformity in the images indicates minimal fringe distortion over the entire beam overlap. The picomotors can be constantly driven to write large-area gratings with continuously varying period and orientation on a substrate mounted to a precision X-Y stage. The Piezo-actuated picomotors (which produce displacement jitter and exhibit low bandwidth operation) will be subsequently replaced by voice coil-actuated fast steering mirrors.

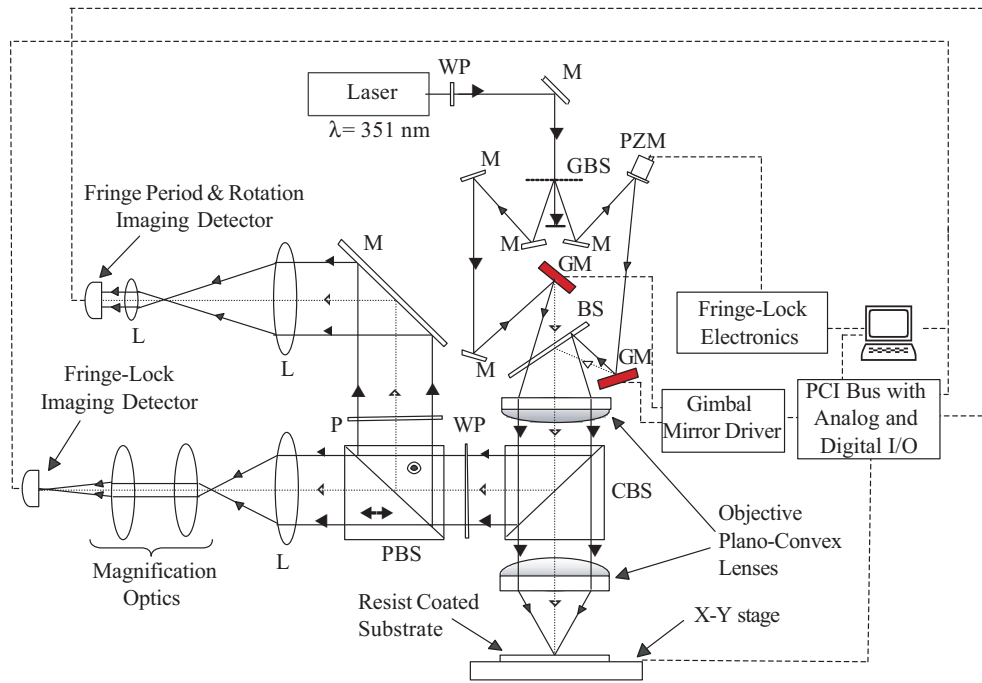


Figure 1. Experimental diagram of variable-period scanning-beam interference-lithography system. *M*: mirror, *L*: lens, *P*: polarizer, *GM*: gimbal mirror, *WP*: wave plate, *BS*: beam splitter, *PZM* piezo-actuated mirror, *GBS*: grating BS, *CBS*: cubic BS, *PBS*: polarizing BS.

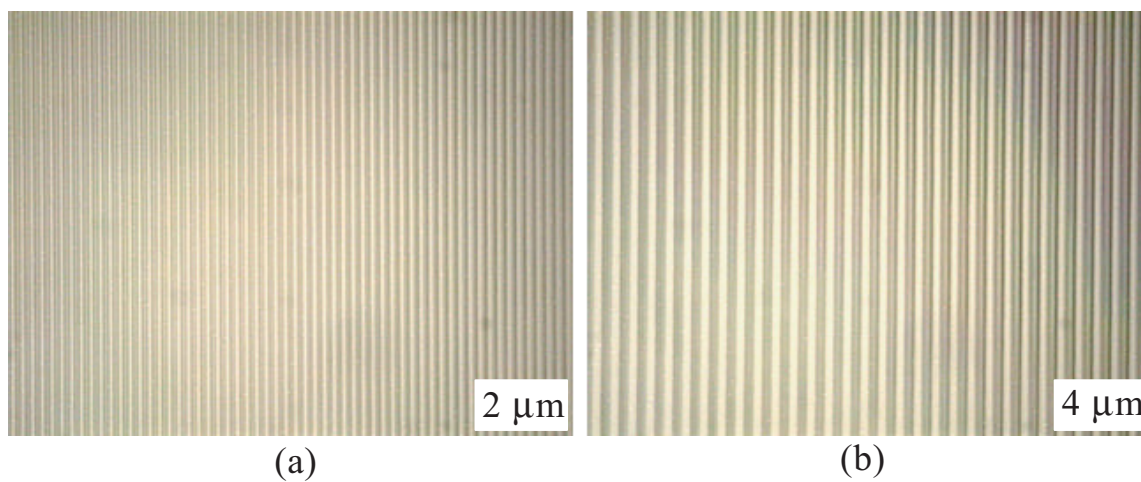


Figure 2. Grating images written by VP-SBIL with period (a) 2.0 μm and (b) 4.0 μm .

13. Precision Fabrication Techniques for Microphotonic Devices

Sponsors:

Defense Advanced Research Projects Agency and U.S. Army Research Office
Grant # DAAD19-99-1-0280, and
Pirelli Lab S.p.A. Contract Number AGMT. DTD. 9/1/01

Project Staff:

Tymon Barwicz, J. Todd Hastings, Joseph Huang, M. Jalal Khan, Michael H. Lim, Professor Hermann Haus, and Professor Henry I. Smith.

Microphotonic devices seek to miniaturize and integrate the components needed for optical networking. These devices have exacting fabrication tolerances for feature size, pattern-placement, and surface roughness. Careful control of feature size is critical for resonant structures and phase-matching between coupled waveguides, while pattern-placement is essential for devices that rely on long-range interference effects. Surface roughness often dominates optical loss in a device. As a result, only careful control of the fabrication process can maximize device performance. This project focuses on Bragg-grating-based devices and high-index-contrast devices; both of which require precision fabrication.

Grating-Based Devices

Bragg gratings have widespread application in the field of optical telecommunications. A Bragg grating is formed by creating a periodic corrugation or refractive index modulation in an optical waveguide. Such a structure behaves as a wavelength-selective filter, reflecting a narrow band of wavelengths while transmitting all other wavelengths. Although Bragg gratings are commonly imprinted in photosensitive optical fiber, physically-patterned gratings in planar waveguides, shown in figure 1, offer a number of advantages. For example, one can build Bragg gratings in non-photosensitive materials such as indium phosphide or silicon. In addition, integrated gratings can contain precise phase-shifts and variations in grating strength to achieve a desired filter response. Finally, the planar-fabrication process can integrate multiple gratings with splitters, couplers, and other optoelectronic components on a single, readily manufacturable chip.

We use a combination of several different types of lithography to generate Bragg-grating devices. In interference lithography, two coherent laser beams are crossed, generating a standing-wave interference pattern. This standing-wave pattern is used to expose photoresist, yielding a coherent submicron-period grating. This grating can be used directly as the device grating or it can serve as a precision reference for later electron-beam lithography steps.

For devices that require long Bragg gratings with engineered phase shifts or variations in grating strength, we use a technique called spatially-phase-locked e-beam lithography (SPLEBL), which combines the long-range spatial coherence of interference lithography with the flexibility of scanning e-beam lithography. Inherent pattern-placement errors in gratings written by standard e-beam lithography limit device performance. SPLEBL references the interference-generated grating during the e-beam exposure to minimize these placement errors.

In many cases, the techniques mentioned above are not applied directly to a device, but instead to an x-ray lithography mask. Once the mask is generated, with the appropriate gratings and alignment marks, the patterns can be repeatedly transferred to substrates using x-ray lithography.

One of the critical challenges facing integrated Bragg gratings is that they often require submicron grating structures patterned over relatively tall optical waveguides. In order to address this topography problem, we have developed a dual-hardmask process, depicted in Figure 2. This process allows both lithography steps to be performed over essentially planar surfaces. Figure 3

shows devices fabricated by the dual-hardmask process in the indium-phosphide and silicon-on-insulator materials systems.

In many cases it is desirable to place Bragg gratings in the sidewalls of optical waveguides as shown in Figure 1 (b). This technique allows the grating and waveguide to be patterned in the same lithographic step. As a result, the grating depth can be easily varied along the waveguide to introduce apodization. Apodization, the process of gradually increasing and then decreasing the grating strength, reduces side-lobe levels in the reflection and transmission spectra of the device, thus reducing cross-talk between neighboring channels in wavelength-division multiplexing. Figure 3 shows an apodized-sidewall grating in a SOI ridge waveguide along with measured transmission spectra. The waveguide-grating structures were patterned using spatial-phase-locked e-beam lithography (SPLEBL) and chlorine reactive ion etching. The silicon-on-insulator substrates were provided by Canon.

High Index-Contrast Devices

High-refractive-index-contrast-material systems enable very small bending radii in microphotonic devices. In low-index-contrast waveguides (such as optical fibers), the bending radii must be on the order of centimeters. On the other hand, integrated-optical waveguides exploiting the high index contrast between Silicon Nitride and Silicon Oxide may have bending radii on the order of 10 μ m. This is 1000 times smaller. Consequently, device size shrinks considerably, and large-scale integrated optical circuits become possible. Unfortunately, fabrication of high-index-contrast microphotonic devices is much more demanding than fabrication of low-index-contrast ones. The main challenges reside in precisely and accurately controlling dimensions of submicron features as well as in achieving the required smoothness of waveguide sidewalls. High-index-contrast microphotonic devices are much more sensitive to feature size variations. Moreover, scattering losses due to sidewall roughness become increasingly important when index contrast goes up and may even render devices unusable. In the NanoStructures Laboratory, dimensional control is addressed by using direct-write scanning-electron-beam lithography. The higher resolution allows for much better control of submicron features than photolithography. Sidewall roughness is addressed by optimizing reactive-ion etching for minimal mask erosion (see figure 5). Additionally, quantitative sidewall roughness measurement techniques are developed for efficient optimization and monitoring of fabrication processes.

An add-drop filter based on optical racetrack resonators is shown on figure 6. Light is evanescently coupled from a bus waveguide to an adjacent racetrack. If the optical path in a racetrack is equal to an integer number of wavelengths, one will have resonance. In this case, power will be entirely transferred from one bus waveguide to the racetracks and then to the other bus waveguide. The resonance has a Lorentzian profile for a single racetrack and becomes sharper if multiple racetracks are used. The whole device occupies about 20 by 50 μ m while low-index-contrast add-drop filters require millimeters or even centimeters.

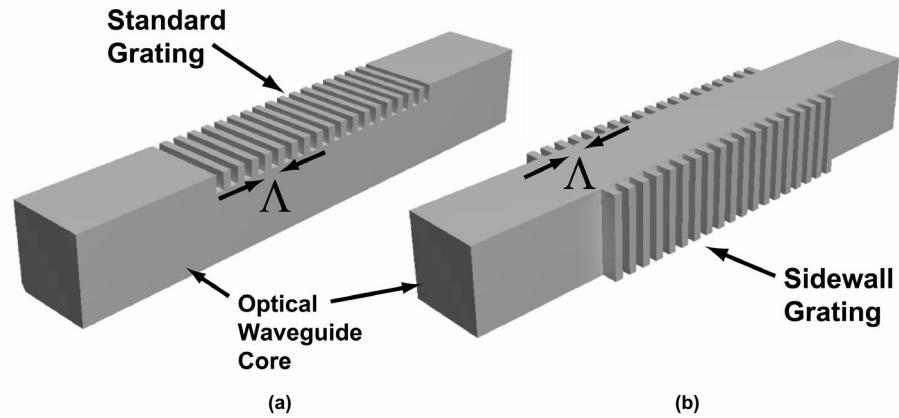


Figure 1: Two possible configurations for physically patterned Bragg gratings in optical waveguides. (a) Bragg grating patterned in the top of the high-index core. (b) Bragg grating patterned in the sides of the high-index core.

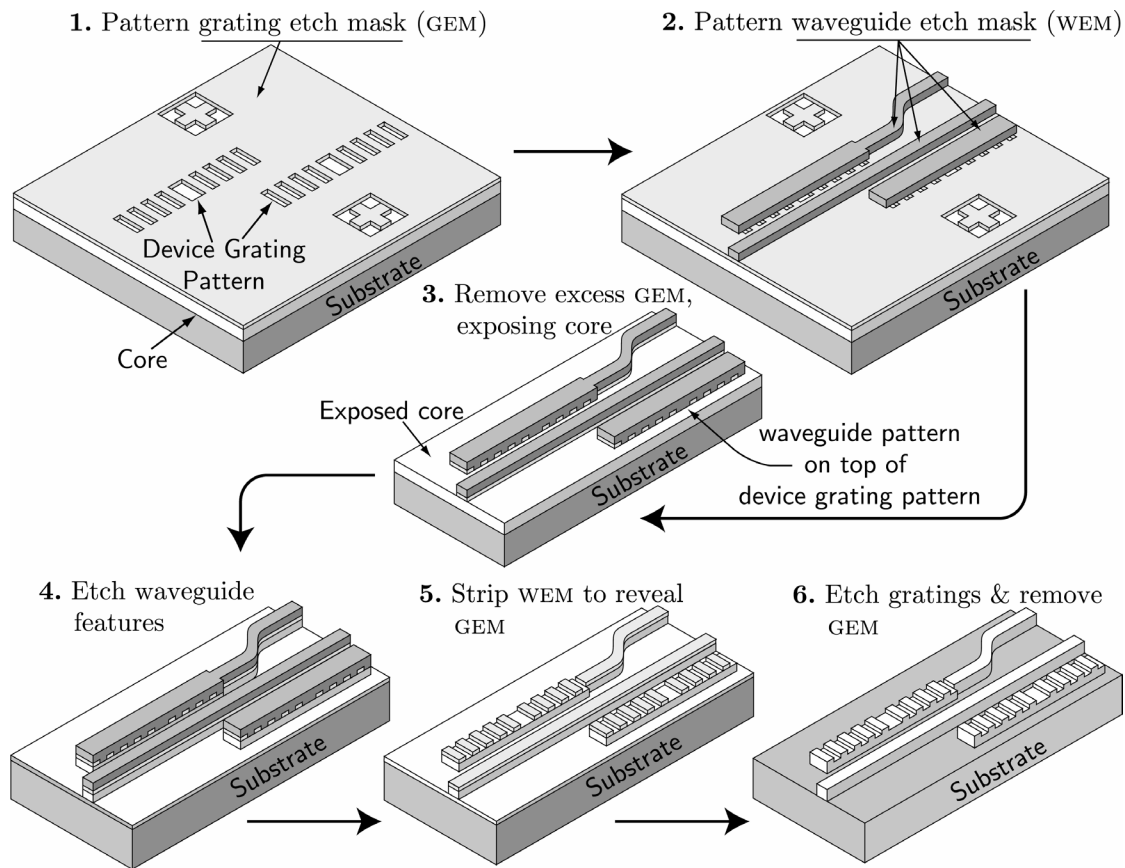


Figure 2: Dual-hardmask process used to pattern fine-period Bragg gratings atop relatively tall waveguide structures. The process is designed such that all lithography steps are performed over essentially planar topography.

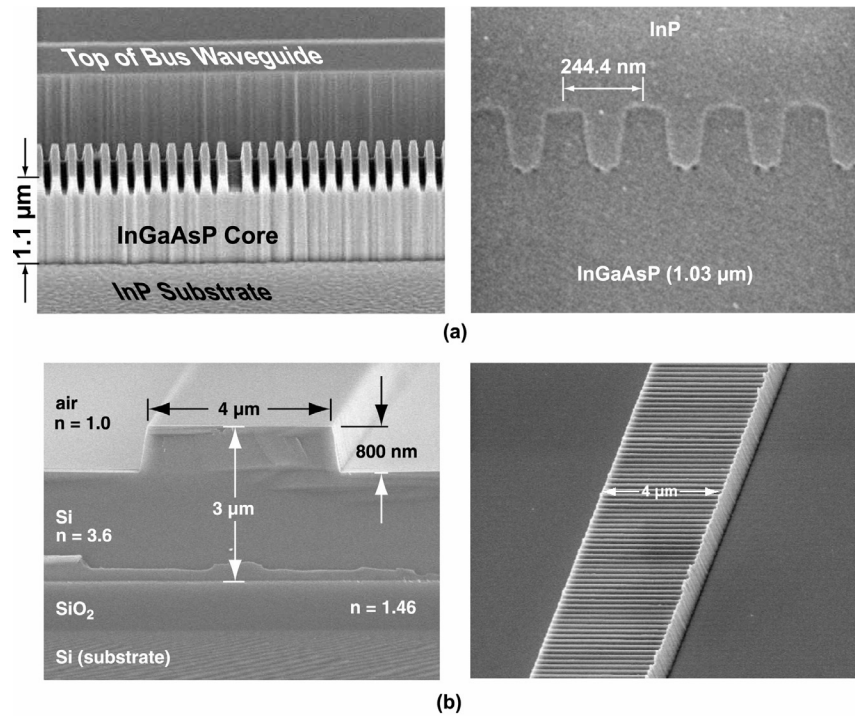


Figure 3: Examples of the dual-hardmask process applied to two different materials systems. **(a)** Scanning-electron micrograph depicting a quarter-wave-shifted, 244.4 nm period Bragg grating etched into the top surface of an InGaAsP waveguide, and the subsequent InP overgrowth. **(b)** Silicon-on-insulator (SOI) ridge waveguide cross-section and SOI waveguide with Bragg grating in the top.

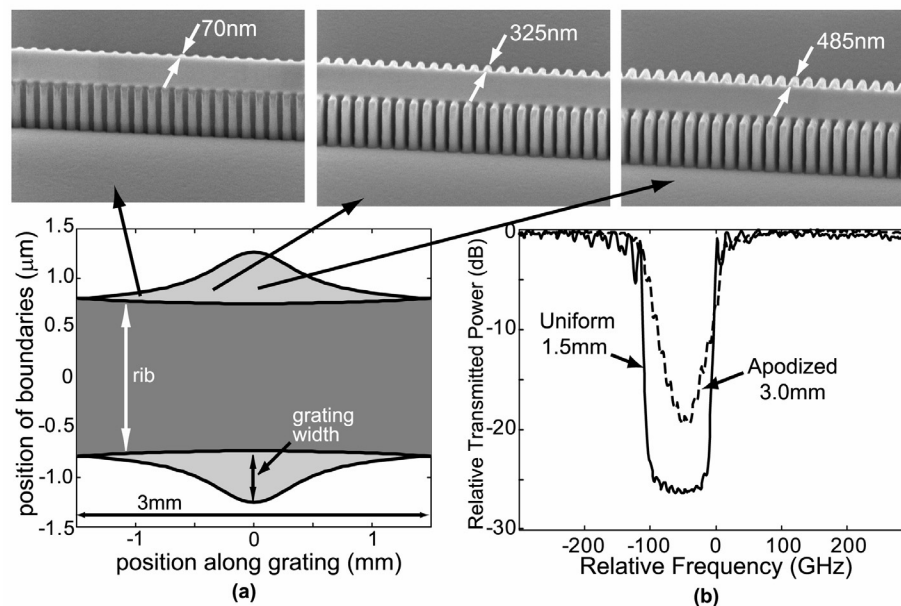


Figure 4: **(a)** Apodized Bragg gratings fabricated in the side-walls of a SOI ridge waveguide. **(b)** Transmission spectra for the TE- mode of uniform and apodized waveguide-grating devices. The reduction of side-lobe levels for the apodized devices is readily apparent.

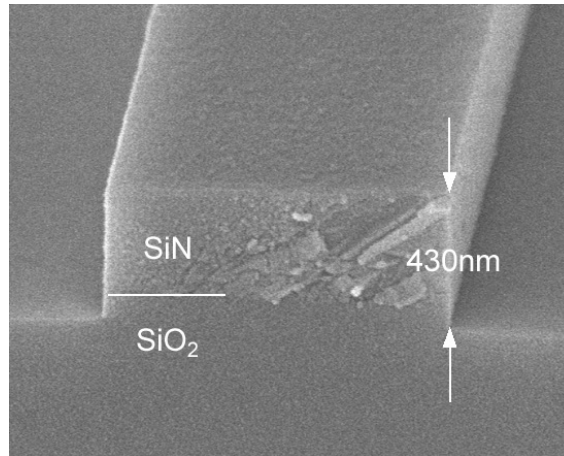


Figure 5: Cross-section of a high-index-contrast waveguide with smooth sidewalls. Light is guided by the 330nm thick Silicon-rich Silicon Nitride (SiN) layer with an index of refraction of 2.20. The Silicon Oxide layer is about 3 microns thick and acts as optical isolation from the Silicon wafer.

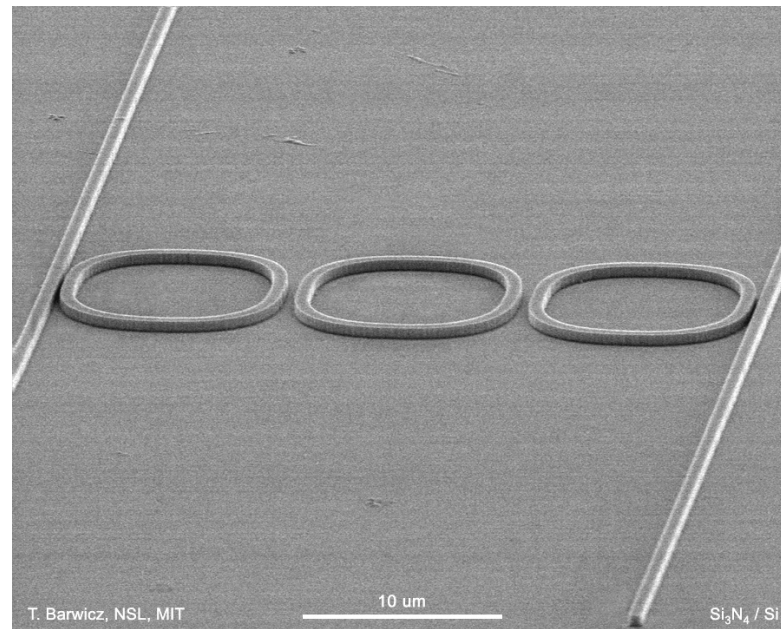


Figure 6: Add-drop filter based on optical racetrack resonators. This structure was fabricated using scanning-electron-beam lithography. For high-volume manufacturing, a high-resolution replication technique such as x-ray lithography could be used.

14. Fabrication of 3-D Photonic Bandgap Structures

Sponsors:

National Science Foundation
Contract DMR-9808941

Project Staff:

Minghao Qi, Professor John Joannopoulos, Professor Henry I. Smith

Three-dimensional (3D) Photonic Bandgap (PBG) Structures offer opportunities for miniaturizing a variety of conventional optical devices. The structure under investigation consists of a stack of alternating “hole” layers and “rod” layers, which themselves are 2D PBG structures (Figure 1). Consequently, result most results in 2D structures can be ported to the 3D design with minimal modification. Compared to other 3D structures in the literature, this design has the unique advantage that each layer is highly symmetric so that optical devices, such as cavities and waveguides can be realized by modifying only one layer. From the fabrication point of view, the rod layer is a byproduct of etching holes into the previous hole layer, which effectively cut the fabrication steps by one half.

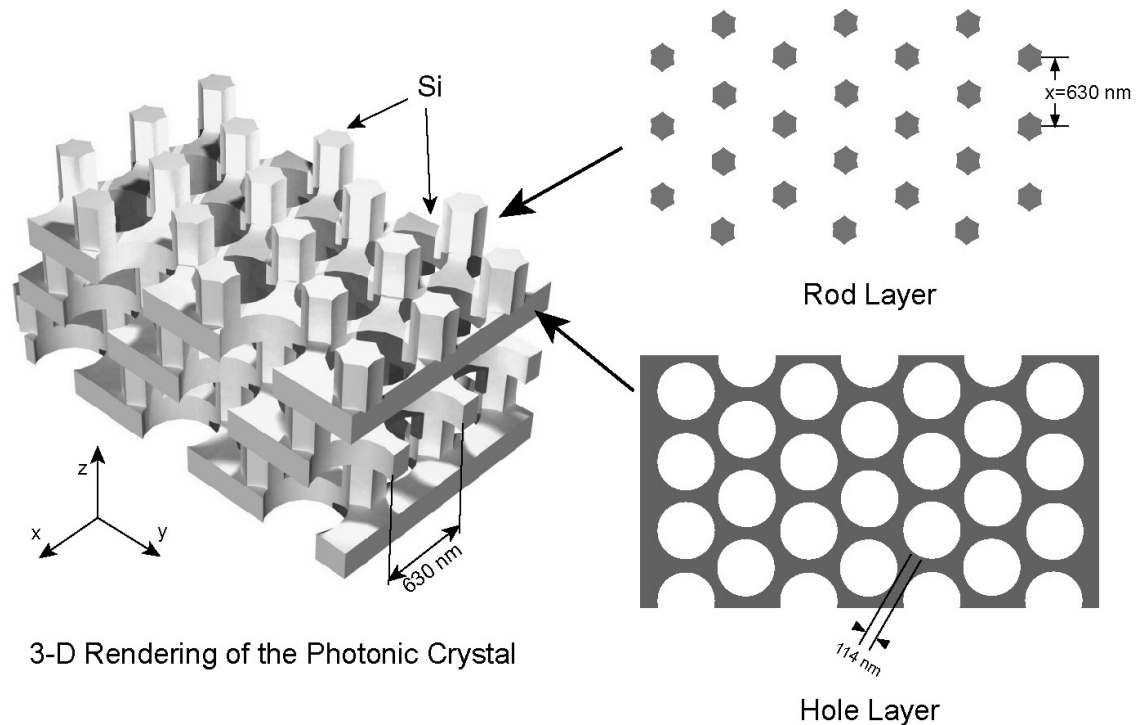


Figure 1: A schematic of the MIT 3D photonic crystal.

The structure has been fabricated in a layer-by-layer approach using e-beam lithography and spin-on-dielectrics planarization. E-beam lithography has the advantages that it allows design flexibility, controlled introduction of defects and robust overlay alignment. Figure 2 shows the SEM micrographs of the final structure. Seven functional layers can be seen clearly.

With the success of the pilot process, two efforts are ongoing simultaneously. One is to fine-tune the structure and process, and the other is to demonstrate the capability of large area, low-cost fabrication of 3D PBG structures.

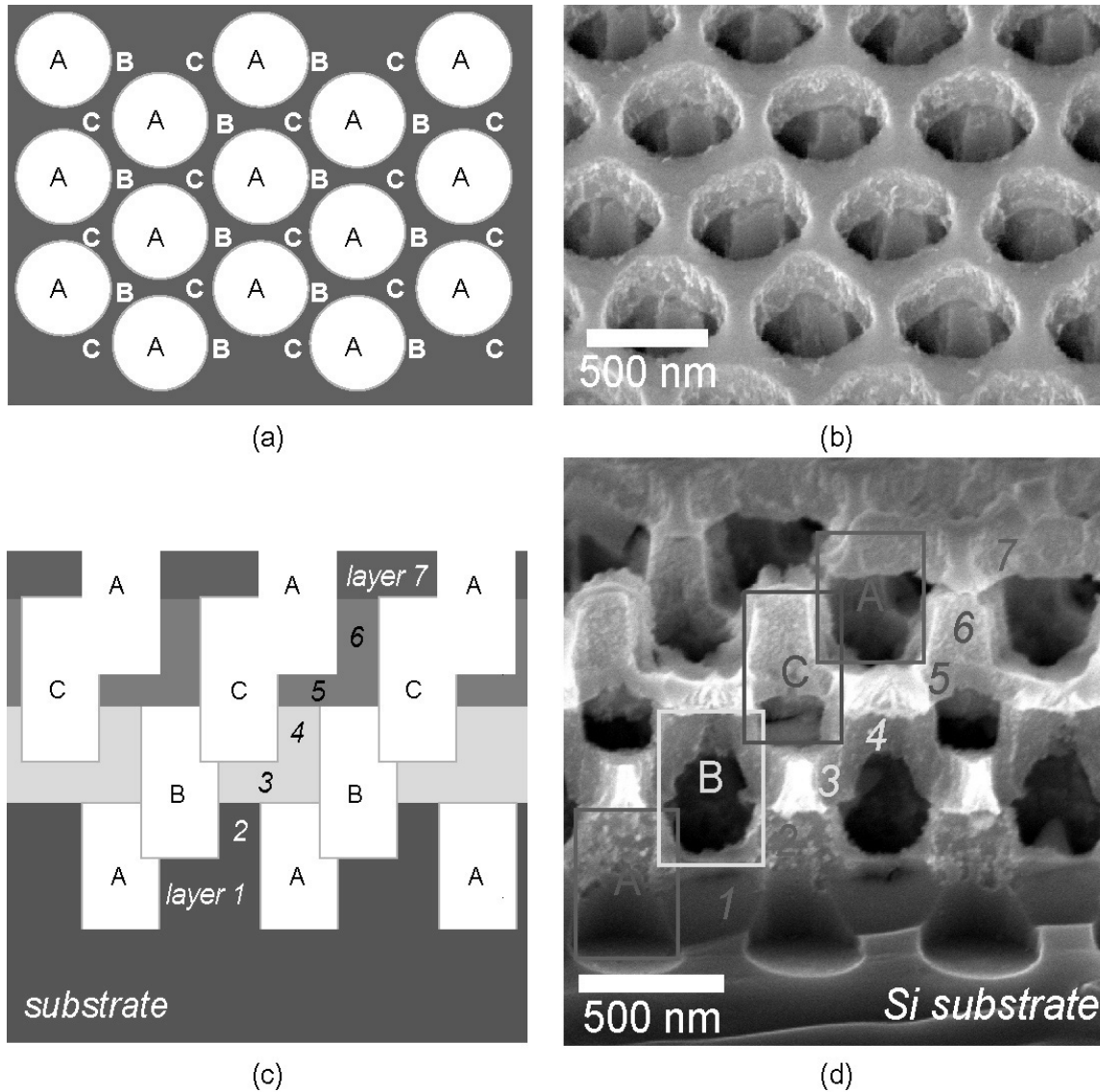


Figure 2: (a) Schematic of the 3D photonic crystal viewed from the top, showing the hexagonal array of holes. The points marked "B" and "C" designate the centers of holes in layers beneath, as depicted in cross section in (c). (b) Scanning-electron micrograph of the seventh layer of the photonic crystal. The sixth layer can be seen through the holes. (c) Cross-sectional schematic of the photonic crystal. Different colors correspond to different process cycles. (d) A cross-sectional view of the 3D photonic crystal cleaved with a diesaw. The functional layers are marked by numbers, while the etched holes are outlined with rectangles.

The structure shown in Figure 1 is suboptimal because the effective radius of the rod layer is dependent on the hole size. The bandgap can increase from 21% (measured as a percentage of the midgap frequency) to 27.3% if the shape and size of the rods can be varied (in this case reduced) independently from those of the holes. However this will require that the rod layer being fabricated in a separate step. A balance can be found by changing the shapes of the holes as shown in Figure 3(a). In this way the rod size will be reduced due to the extra semicircular holes

at the six corners of the main holes. Meanwhile the change of the effective hole size is minimal because the holes are much larger than the rods. Simulation shows that a complete bandgap of 25% can be achieved, which is a 19% increase over the original 21% gap. The fabrication of such a structure will be no different than the pilot process since the e-beam lithography can pattern virtually any shapes. A larger bandgap is highly desirable because it displays the biggest optical effects, allows the widest bandwidth for optical devices, and most importantly, is robust in the presence of fabrication imperfections.

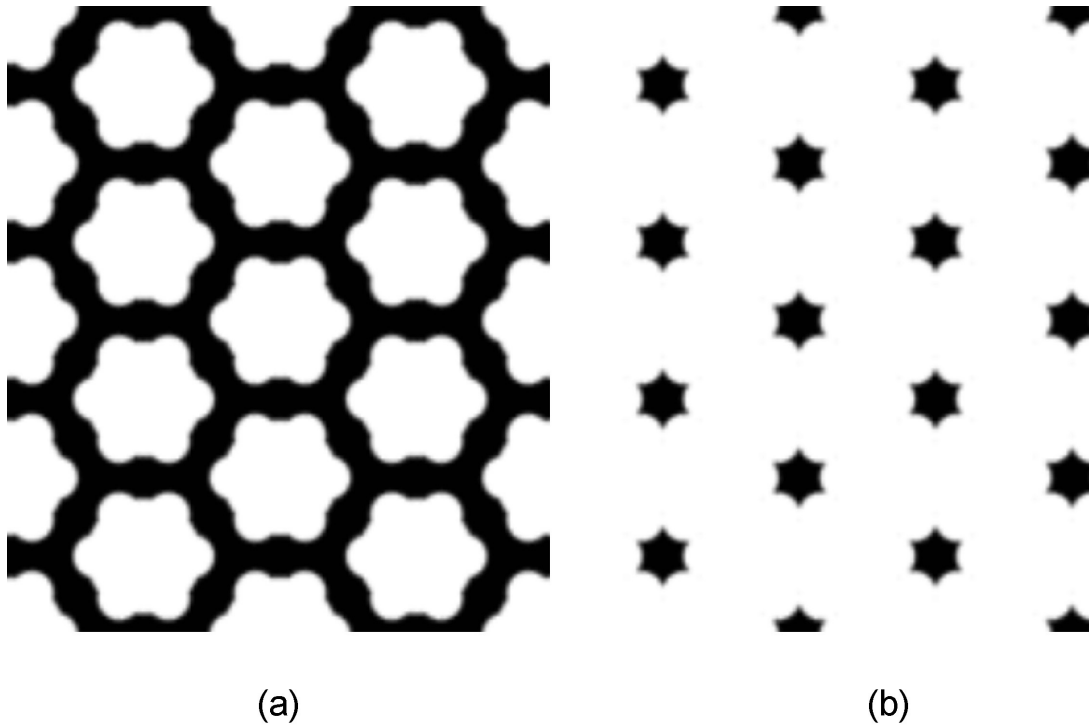


Figure 3: Schematics of the improved 3D PBG design. (a) The “hole” layer. (b) The “rod” layer.

In order to realize real-world applications of 3D PBG structures, large area and spatial coherence are required. Interference lithography can easily pattern a hexagonal lattice of holes (or rods) by a double exposure with the second exposure rotated 60 degrees from the first. However, the holes obtained are elliptical. Such elliptical shape breaks the hexagonal symmetry of the lattice, and simulation shows that the bandgap will be reduced by a factor of two. Last year we proposed a set of new techniques which overcame such difficulty via a combination of interference lithography and tilted x-ray lithography. The method is ideally suited to low-cost, large-area 3D fabrication of periodic structures. This year we set up the equipment and demonstrated the synthesis of a hexagonal array of circular holes (Figure 4). The staging that we build for exposure is shown in Figure 5.

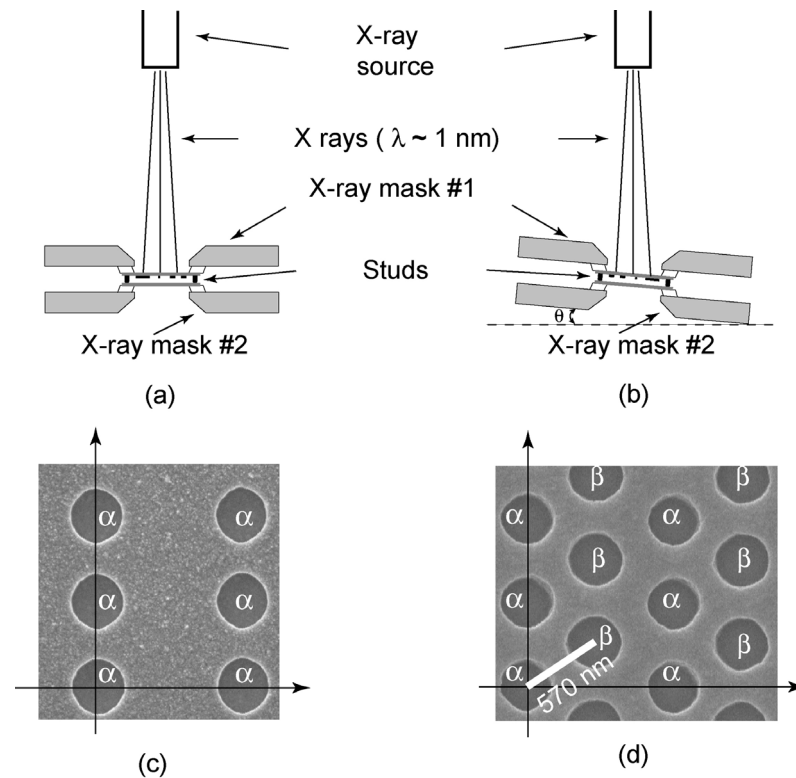


Figure 4: Synthesizing a hexagonal lattice of circular holes with tilted x-ray exposure. (a) Schematic of proximity x-ray exposure. (b) After the first exposure, a second one is carried out with the mask-substrate assembly tilted with an angle $\theta = G/V$, where G is the gap between the mask and substrate and V is the image shift vector, in this case it is set to 570nm. (c) Pattern on x-ray mask #1. (d) Pattern on the substrate after the double exposure (in this case the substrate is a wafer).

By combining this tilting technique and an overlay alignment technique, such as interferometric broad-band imaging (IBBI), it should be possible to fabricate large area 3D photonic crystal.

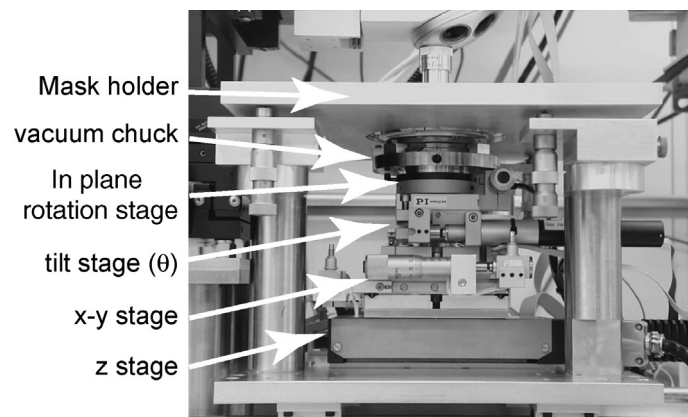


Figure 5: Photograph of the stage for tilted x-ray exposure. The x-ray source, which is not shown, is above the mask holder.

15. **Enhanced Extraction from a Light-Emitting Diode Modified by a Photonic Crystal and Lasing Action**

Sponsors

National Science Foundation - #DMR-9808941

Project Staff

Alexei A. Erchak, D. J Ripin, Dr. S. Fan, Peter Rakich, Dr. Gale Petrich, M. Mondol, Professor Erich P. Ippen, Professor John D. Joannopoulos, Professor Leslie A. Kolodziejki, and Professor Henry I. Smith

Semiconductor LEDs have the potential to be low-cost and long-lifetime solid-state lighting sources for applications as varied as room lighting and flat-panel displays. LEDs are also used in short-range telecommunication systems and may be desirable for optical interconnects in computers. Unfortunately, most of the light emitted from a semiconductor LED is lost due to total internal reflection resulting in low extraction efficiency.

In this work, the effect of a two-dimensional (2D) photonic crystal (PC) on the emission properties of a quantum well (QW) inside an LED is examined. Enhanced extraction of light into the vertical direction is obtained and attributed to the presence of leaky resonant states created by the coherent scattering from the periodicity of the PC. Scattering along the high-symmetry directions also provides sufficient distributed feedback for lasing to occur. The 2D PC is fabricated in the top cladding layer of an asymmetric active region that emits at $\lambda = 980$ nm with a full-width at half-maximum of approximately 60 nm at room temperature. The photoluminescence (PL) emission at 935 nm, normal to the surface, is enhanced by a factor of 100, and the spectrally integrated PL is enhanced by a factor of 8, both when compared to a reference structure without a PC. When optically pumped above threshold, lasing occurs at a wavelength of 1005 nm. This work provides a basis for the design of high efficiency LEDs and lasers based on 2D PCs.

The 2D PC is a 30×30 μm triangular lattice of holes etched within the upper InGaP cladding layer of a 50 μm mesa, as illustrated in Figure 1. To minimize carrier recombination at the etched surfaces, the holes do not penetrate the InGaAs QW; however, the hole depth is sufficient to cause enhanced extraction of light and laser feedback. The device structure is grown using gas-source molecular beam epitaxy. The separation layer is initially grown as $\text{Al}_{0.98}\text{Ga}_{0.02}\text{As}$ and the DBR consists of AlAs and GaAs layers. A SiO_2 layer is deposited on the grown structure

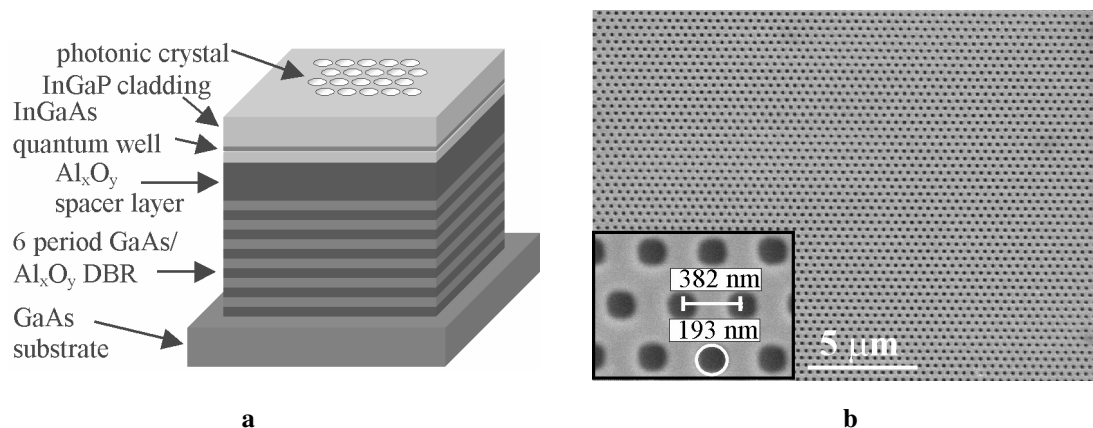


Figure 1. a) The 2D PC structure. b) Scanning electron micrographs of PC structure.

using plasma enhanced chemical vapor deposition. The holes are defined in PMMA by direct-write electron-beam lithography. The electron beam writes a square pattern in the PMMA to represent each hole. The beam size, however, is larger than the step size for translating the electron beam. This leads to the desired circular pattern following development.

The PMMA is used as a mask in transferring the hexagonal pattern to the SiO₂ layer using RIE. This is accomplished by RIE with a CHF₃ plasma using 15 second steps in between 1 minute cool-down steps. The purpose of the cool-down step is to prevent flowing of the PMMA mask. The SiO₂ mask is subsequently used in the RIE of the holes into the upper InGaP cladding layer using RIE with a CH₄/H₂/O₂ plasma in a 20:20:2.5 gas flow ratio. The mesas are next defined using photolithography followed by RIE with the CH₄/H₂/O₂ plasma to penetrate the active region. RIE with a BCl₃ plasma is used to expose the mesa sidewalls. The final step in the device fabrication is the wet thermal oxidation of the Al_{0.98}Ga_{0.02}As separation layer and the AlAs DBR layers. Figure 1b shows scanning electron micrographs of a PC structure with lattice constant, *a*, of 382 nm, hole diameter of 193 nm, hole depth of 101 nm, and an active region thickness of 198 nm. This structure is characterized and the results are reported below.

The photoluminescence is observed using a cw Ti:Al₂O₃ laser with an emission wavelength of 785 nm. Figure 2(a) shows a spectrum of the enhancement of PL from the PC region normalized to the same structure but without a PC. Figure 2(b) is a calculation of the photonic band structure near the Γ point in the first Brillouin zone. The bands represent leaky resonant states that provide a pathway for the enhancement of light extraction. On the long wavelength end of the spectrum, the range covered by the first three bands closely matches the large observed peak centered near 935 nm. The width of the peak is determined by the Q of the leaky resonance and by the collection angle (dotted line). Band 4 and bands 5 and 6 closely match the peaks near 890 nm and 860 nm respectively. The dip between peaks 2 and 3 corresponds well with the gap in available states between bands 3 and 4.

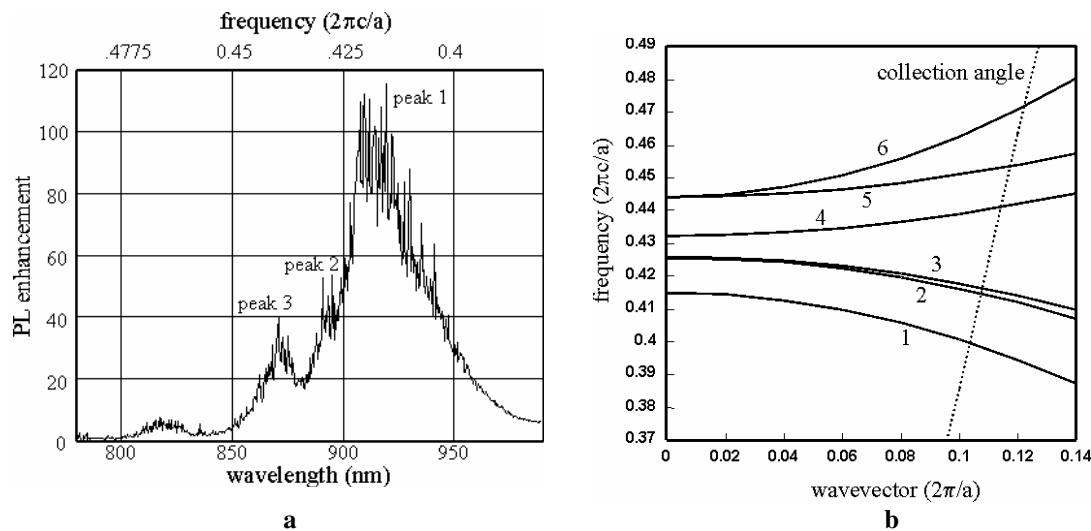


Figure 2: a) PL enhancement spectrum from PC structure. B) Calculated photonic band structure near Γ point.

Lasing occurs at a wavelength of 1005 nm as the pump power is increased (Figure 3(a)). The lasing peak occurs from distributed feedback and corresponds well with the bending of bands at the M point (Figure 3(b)).

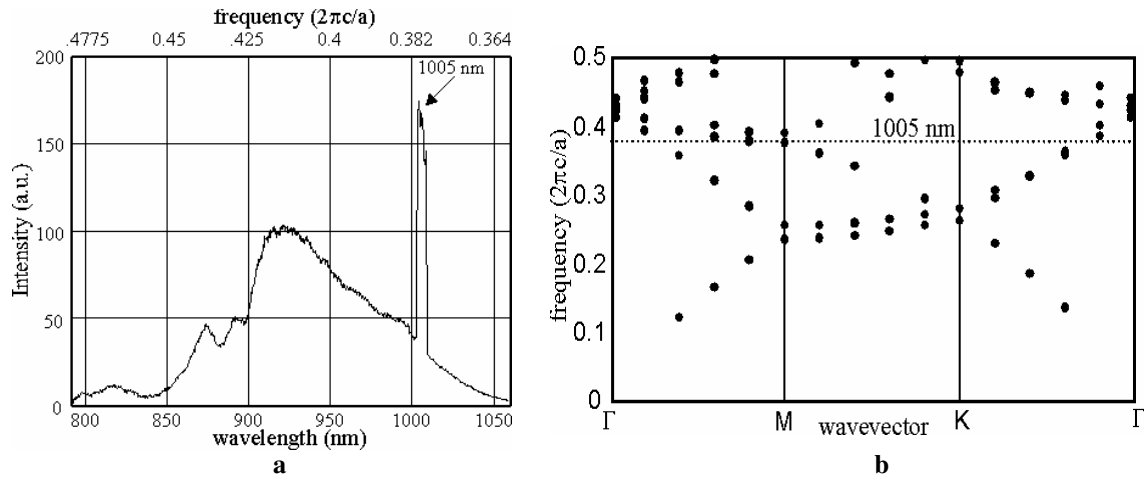


Figure 3. a) Lasing spectrum. b) Calculated band structure showing band folding near M point.

16. Design and Fabrication of a Superprism Using Two Dimensional Photonic Crystals

Sponsors

DARPA/Rockwell Scientific Corp. #B1F431652

Project Staff:

Sheila Tandon, Chiyan Luo, Michael E. Walsh, Dr. Gale S. Petrich, Prof. Leslie A. Kolodziejski, Prof. Henry I. Smith, and Prof. John D. Joannopoulos

A superprism is an optical device similar to a conventional prism only with two enhanced properties: (1) super-dispersion and (2) ultra-refraction. Just as a conventional prism separates light into its component wavelengths, a superprism separates these wavelengths over wider angles--termed "super-dispersion." A superprism can magnify the angle of propagation of a single wavelength of light to steer the beam over wide angles--termed "ultra-refraction." Photonic crystals are responsible for the superprism effect. Superprism effects would be useful in a number of applications ranging from enhanced devices for wavelength-division multiplexing (WDM) to a new class of ultra-refractive optical elements for beam manipulation.

Our superprism consists of a 2D photonic crystal with a square lattice of cylindrical air holes in a high index material such as silicon or gallium arsenide. The top view schematic of the device shape is shown in figure 1. The device is hexagonal shaped with the photonic crystal (PC) occupying a square region in the center. The initial design has focused on realizing ultra-refraction such that an input angular sweep of approximately +/- 2 degrees is amplified to about +/- 30 degrees at the output for a wavelength of 3.2 μm . A thick low-index layer is used to minimize radiation loss into the high index substrate.

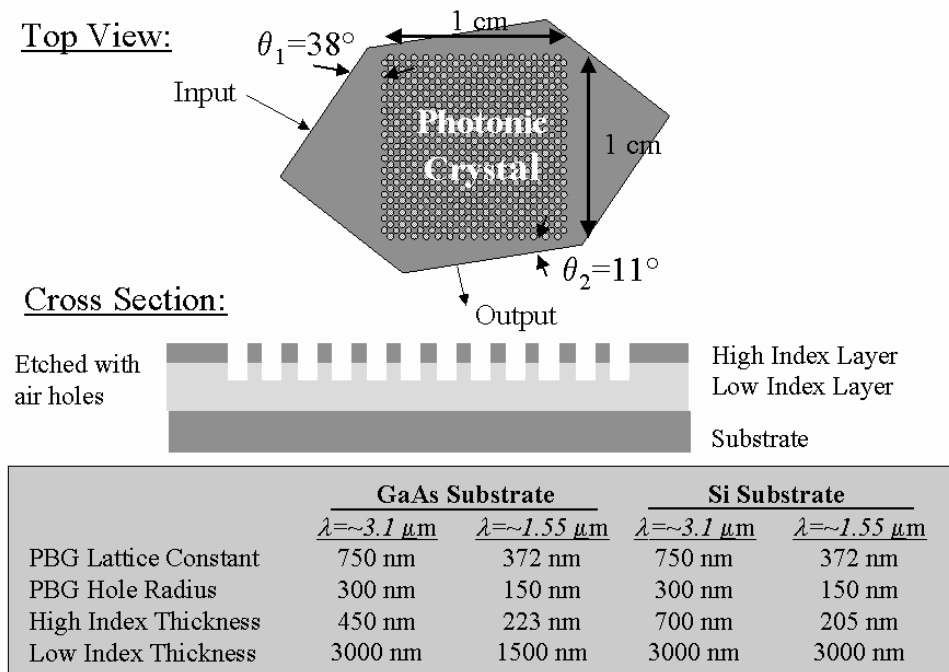


Figure 1: Superprism device design showing top and side views of the device.

The feature sizes of the photonic crystal can be scaled depending on the wavelength of operation as shown in figure 1. Our desired wavelengths of $3.1\mu\text{m}$ and $1.55\mu\text{m}$ imply hole lattice constants of 750nm and 372nm , and hole radii of 300nm and 150nm . The total thickness of the device (excluding substrate) is about 3.5 microns (460nm GaAs, $3\mu\text{m}$ Al_xO_y) while the top surface will have an area somewhat larger than $2\text{x}2\text{cm}$.

The hexagonal device shape is patterned using photolithography while the photonic crystal holes are patterned using interference lithography and a tri-layer resist process. After each lithography step, patterns are etched into hard mask layers via reactive ion etching (RIE). The fully patterned hard mask layers are then used to etch the substrate material via another RIE step. Figure 2(a) is a photograph of the patterned hard-mask layers on a silicon substrate. Two hard-mask layers have been used: 50nm chromium on top of 250nm HSQ (spin-on oxide). The chromium layer is patterned with the superprism hexagonal shape while the open square area is patterned with the $\sim 780\text{nm}$ period photonic crystal in HSQ. The diffraction pattern from the PC can be seen as a blue streak across the square area.

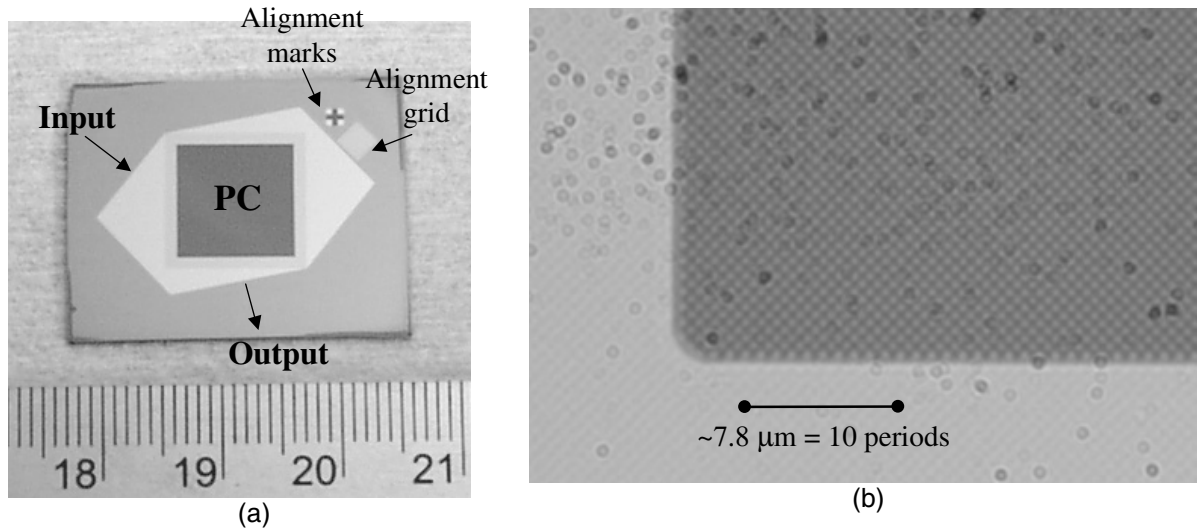


Figure 2: (a) Photograph showing a top view of the superprism hard mask layers on a silicon substrate. (b) Microscope image of the corner area of the photonic crystal region shown in fig 2(a). The defects in the photograph are due to dust particles in the microscope optics that could not be readily removed.

Figure 2(b) shows a microscope image ($100\times$ magnification) of the corner region of the photonic crystal area. The square grid of the PC is rotated 45 degrees with respect to the square region. The alignment accuracy between the photonic crystal orientation and the square region is critical for superprism performance. Figure 2(b) shows how a line of PC holes is aligned to the square edge with accuracy of less than one degree thus achieving our required tolerance.

Future work will include calibrating the photonic crystal hole size during the interference lithography, finding a better hard-mask layer than chromium (which leaves behind post-wet-etch residue) and reactive ion etching of the silicon substrate material.

17. Coupling into Photonic Crystal Waveguides

Sponsors

Center for Material Science, National Science Foundation,
Grant # DMR-9808941

Project Staff

Solomon Assefa, P. Rakich, Dr. P. Bienstman, Dr. Steven G. Johnson, Dr. Gale S. Petrich,
Professor John D. Joannopoulos, Professor Leslie A. Kolodziejski, Professor Erich Ippen, and
Professor Henry I Smith

Large-scale photonic integrated circuits require a capability of guiding light around sharp bends with a radius of curvature on the order of the wavelength. In conventional index-guided waveguides, light is confined as a result of total internal reflection at the interface between the high-refractive-index waveguiding layer and its low index surroundings. However, conventional high-index-contrast waveguides are susceptible to large optical losses as the bend's radius of curvature decreases. Photonic crystals (PCs), which consists of a periodic arrangement of high and low-index dielectric material, have been proposed as a potential solution for guiding light around corners, including 90° bends, with near perfect transmission.

The 2D photonic crystal consists of an array of cylindrical rods of high-dielectric material above a low dielectric material. Introducing a line defect, such as a row of smaller radius cylinders, into the 2D photonic crystal results in a linear waveguide. The forest of periodic dielectric rods surrounding the line defect creates a photonic band gap (PBG), i.e. a range of frequencies over which light cannot propagate. Thus, an optical signal with a frequency inside the PBG has its energy confined within the line defect and becomes evanescent into the photonic crystal. The radius of the cylinders in the line defect remains large enough to provide index guiding in the third dimension (normal to the plane of periodicity). The localization of a mode inside the line defect can be utilized to guide light around sharp corners. This is illustrated in Figure 1.

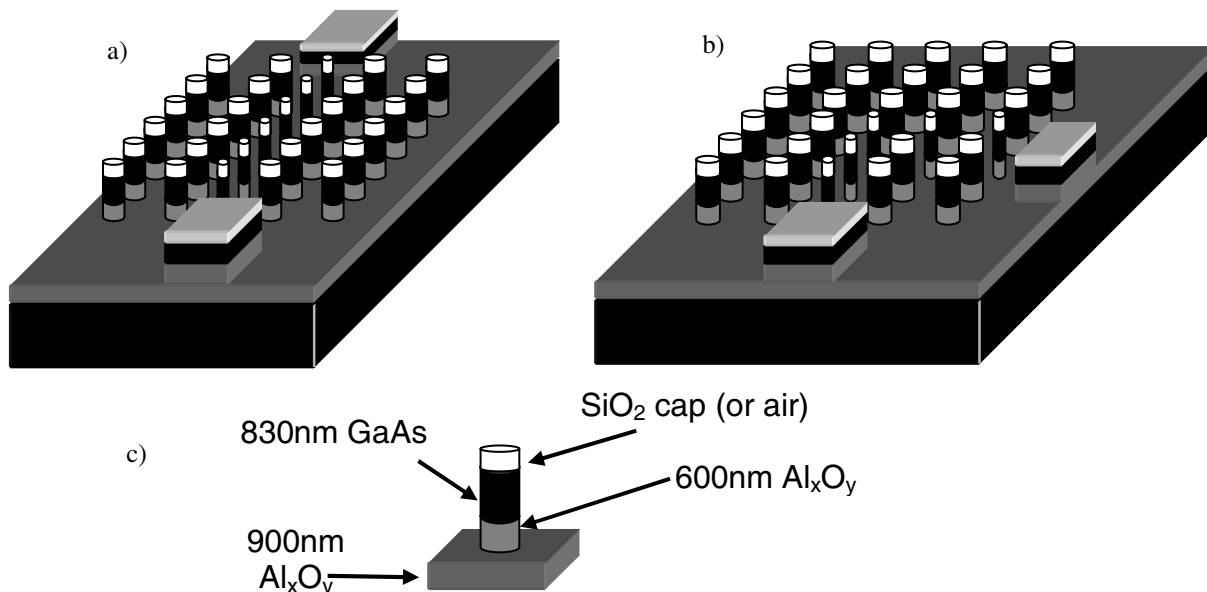


Figure 1 (a) Schematic of a linear PC waveguide. (b) Schematic of a 90° bend PC waveguide. (c) Schematic of a cylindrical pillar structure. For the bulk photonic crystal, the pillar diameter is 300nm; for the defects, the diameter is 250nm.

The practical use of photonic crystal waveguides is limited due to the poor coupling efficiency between the photonic crystal waveguide, and conventional index-guided input and output waveguides. Coupling poses a challenge because the photonic crystal waveguide exhibits a significantly different mode profile and propagation mechanism compared to traditional waveguides that use index confinement. In the conventional waveguide the field has only forward propagating components, while the field in the photonic crystal waveguide has both forward and backward propagating components. Furthermore, guiding in the conventional waveguide is in high index surrounded by low index; in the photonic crystal guiding is in low index surrounded by two photonic crystal “mirrors”.

Figure 2 compares three different designs for coupling into the photonic-crystal waveguide. The design in Figure 3(a) suffers from Fabry-Perot reflection at the edges of the photonic crystal region, which makes the transmission of the waveguide dependent on the waveguide length. By tapering the end of input and output index waveguides as shown in Figure 3(b), the reflection can be somewhat reduced. In the third design, the input waveguide is adiabatically converted into a strongly coupled-cavity waveguide (CCW). This adiabatically transforms the forward propagating component of the field into both forward and backward propagating components before reaching the photonic crystal. Also, the “cladding” is introduced slowly from the edge, thereby adiabatically transforming the mode from high-index guiding to gap guiding. 2D simulations show that this coupling scheme results in almost 100% transmission through the photonic crystal waveguide.

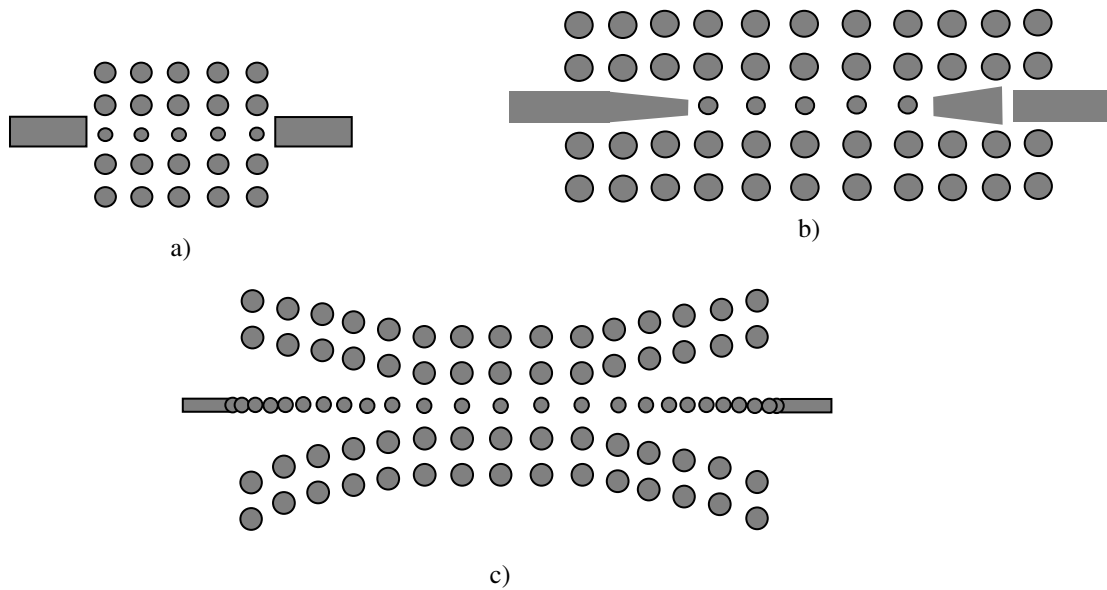


Figure 2. a) Schematic of coupling from untapered dielectric waveguide. b) Schematic of coupling from a tapered dielectric waveguide. c) Schematic of adiabatic transition from a dielectric waveguide into strongly coupled cavities and tapered cladding.

The cylindrical rods of the photonic crystal consist of a high-index, 830nm epitaxial GaAs layer sandwiched between 100nm-thick SiO₂ cap layer and a 600nm-thick low-index Al_xO_y layer. An additional 900nm thick Al_xO_y layer is below the cylindrical rods, isolating the GaAs guiding layer from the GaAs substrate. The heterostructure is grown using gas-source molecular-beam epitaxy on a (100) GaAs substrate. The Al_xO_y is initially grown epitaxially as Al_{0.9}Ga_{0.1}As and subsequently converted.

The fabrication process commences by sputtering 400nm thick SiO₂ on the sample. Next, the waveguide and photonic crystal are defined using direct-write scanning-electron-beam lithography. Each sample is coated with polymethylmethacrylate (PMMA) electron beam resist, and each cylinder is defined by exposing a square pattern. The finite width of the beam rounds-off the corners of each square yielding a circular hole upon development. Simulation show that the largest band gap is obtained from a periodic arrangement of rods with diameter of 300nm. Exposure-dose experiments are done to find the optimal parameters for the exposures. A dose of 536 μC/cm², current of 250pA, and clock frequency of 0.20 MHz gave hole diameters close to the desired values. The input and output coupling waveguides and different sized arrays of holes are written by stitching together 250μm fields.

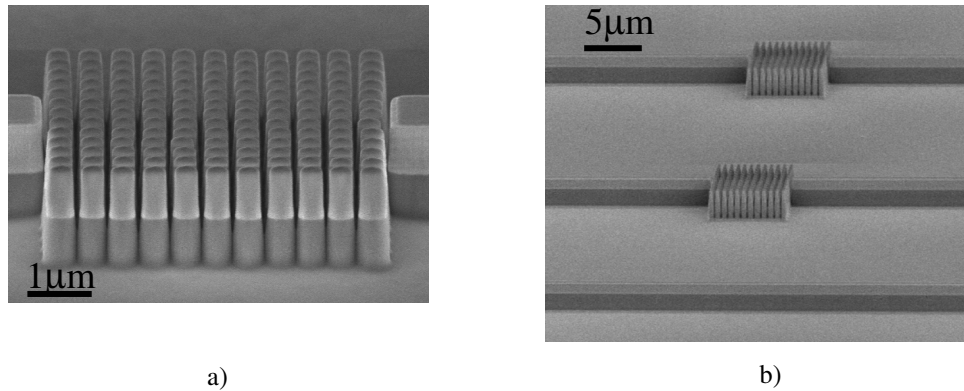


Figure 3. a) Side view SEM of a bulk photonic crystal etched in GaAs/AlGaAs using BCl₃/He plasma. The AlGaAs is oxidized into Al_xO_y. The period is 500nm and the diameter of the pillars is 300nm. The input and output waveguides are 1.5μm wide. b) Photonic crystal devices on a single chip. The design contains a straight waveguide for normalization purposes.

A 50nm-thick nickel film is evaporated on the sample after the PMMA is developed, and a liftoff process is performed. The pattern is transferred to the SiO₂ by reactive-ion etching (RIE) in a CHF₃ plasma after which the nickel mask is removed using nickel etchant. Using the SiO₂ mask, the cylindrical rods are created by etching the GaAs and the AlGaAs to a total depth of 1.5 μm in a BCl₃/He plasma. Experiments were done using various metal masks as an alternative to the SiO₂ mask. However, the metal masks sputtered or degraded during the long duration of the GaAs/AlGaAs etch. Next, each sample is lapped and cleaved in order to create a smooth input facet to promote the efficient coupling of a test signal of 1.55μm wavelength. Finally, the AlGaAs is transformed into Al_xO_y using a wet thermal oxidation process.

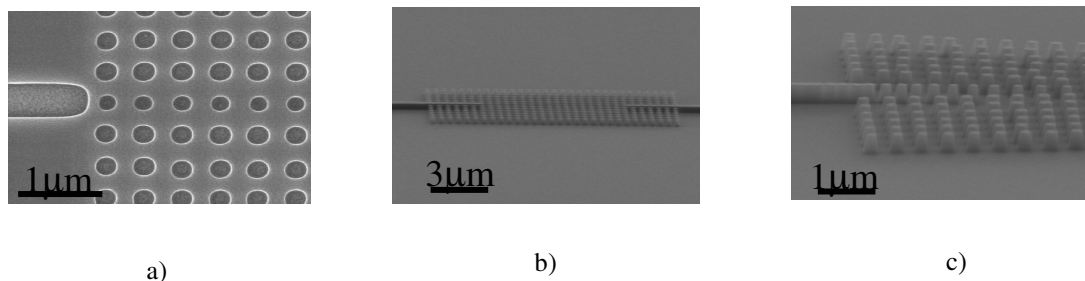


Figure 4. a) Top view SEM of coupling design from Figure 2(a) after e-beam lithography in PMMA. The bulk photonic crystal has hole diameter of 307nm, while the defect has diameter of 244nm. b) Top view SEM of coupling designs from Figure 2(b) after SiO₂ etch. c) Top view SEM of coupling design from Figure 2(c) after SiO₂ etch.

Currently, the photonic crystal devices are being tested. The band gap is being mapped first by varying the number of columns in a bulk photonic crystal. Also, the three coupling mechanisms are being compared to confirm the best transmission through the photonic crystal waveguide.

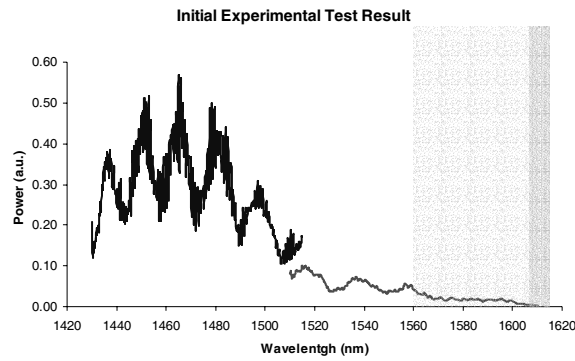


Figure 5. Initial experimental data of a bulk photonic crystal with 7 columns and 13 rows of dielectric pillars. The blue data is for a tunable laser source of 1410nm-1510nm. The red data is for source wavelength of 1510-1610nm. The shaded region indicates the band gap covered by the tunable range. The band gap extends to 1725nm.

18. Development of birefringence-free ridge waveguides for waveguide isolators

Sponsor

Walsin-Lihwa Corporation – Agmt. DTD: 3/26/01

Project Staff

Xiaoyun Guo, Tauhid Zaman, Professor Rajeev Ram and Professor Henry I. Smith

An optical isolator is a device to transport light in only one direction. They are required in optical communication systems to protect laser sources from reflections. Nowadays, microoptic isolators are available, but they are bulky and require expensive alignment. In contrast, a waveguide isolator which can be integrated with the source and other waveguide devices will be necessary for highly integrated photonics circuit, and may be much cheaper. The goal of this project is to develop an integrated waveguide isolator.

A nonreciprocal polarization rotation is the key to an isolator's performance. Faraday rotation is a well known nonreciprocal polarization rotation. We have observed Faraday rotation in magnetically doped InP with $F=6/\text{mm}$, and a loss of $\alpha=0.2\text{cm}^{-1}$ at 1550nm. The coupling ratio is calculation as below in a Faraday rotation.

$$R = \frac{F^2}{F^2 + (\Delta\beta/2)^2}$$

where R is the conversion ratio between TE and TM, F is the Faraday constant, and $\Delta\beta = \beta_{TE} - \beta_{TM}$ is the difference of propagation constants between TE and TM. In a waveguide with linear birefringence, the incomplete conversion of TE and TM will limit the polarization rotation to a small angle. Thus, a waveguide is required to have same propagation constant for both TE and TM in order to have pure nonreciprocal polarization rotation. Linear birefringence arises from various sources including stress, waveguide geometry, photoelastic effect, etc.

We have developed techniques for fabricating birefringence-free ridge waveguides for integrated waveguide isolators. The waveguide consist of a INGaAsP core layer and cladding layers of magnetically doped InP. Both stress-induced birefringence and photoelastic birefringence are negligibly small. To eliminate the shape birefringence, the ridge waveguide is designed to have a certain width and depth. The calculation of parameters for a birefringence-free waveguide is shown in Fig. 1 from a program developed by Mike Watts and Hermann Haus.

In our process, a high-index-contrast mesa is used. The etched depth is 2.0-2.5 μm and the width 1-1.5 μm . The etching mask is 100 nm of Ti. The ridge waveguide is etched using reactive ion etching with a mixture of hydrogen and methane. An SEM micrograph of the etched ridge waveguide is shown in Fig. 2.

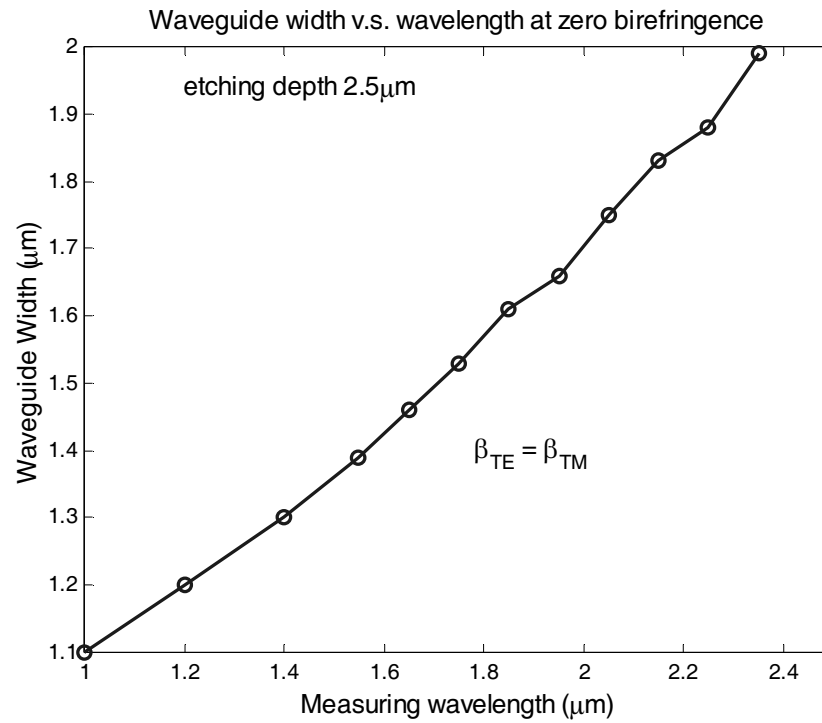


Figure 1. Calculation of zero birefringence for different waveguide widths and measuring wavelengths (2.5 μm etch depth for all waveguides)

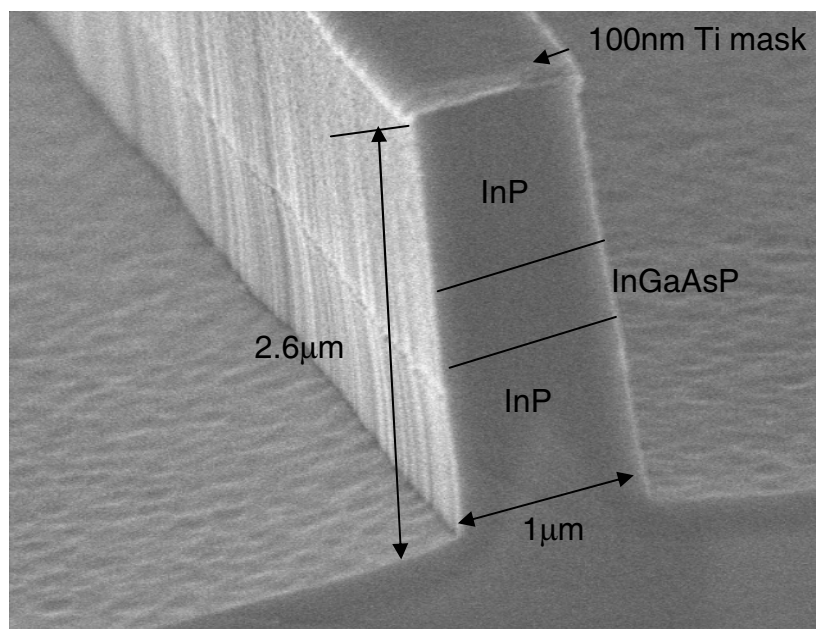


Figure 2. Scanning-electron micrograph of a RIE etched ridge waveguide

19. **Nanomagnets and Magnetic random access memories**

Sponsors

Cambridge-MIT Institute, National Science Foundation

Project Staff

Professor Caroline A. Ross, Professor Henry I. Smith, Dr. Fernando J. Castaño, Yao Hao, Michael Walsh, Dario Gil, Alexander Eilez, Elizabeth Lyons, in collaboration with F. Humphrey and M. Redjda (Boston University)

We are using a variety of lithography techniques (electron-beam lithography, interference lithography, block copolymer lithography and X-ray lithography) to produce arrays of pillars, bar-shaped, and ring-shaped ‘nanomagnets’. These tiny structures have thicknesses of a few nanometers and lateral dimensions typically smaller than 100 nm. Arrays of these elements are made with spatial periods of 100 nm and above. Nanomagnets have been made by electrodeposition, by evaporation and liftoff, or by etching of a sputtered film. We are exploring the switching mechanisms of the particles, the thermal stability of their magnetization, and interparticle interactions, and we are assessing their suitability for various data-storage schemes. The behavior of individual particles can be measured using magnetic-force microscopy, while the collective behavior of arrays of particles can be measured using magnetometry. Comparison of these data shows how the behavior of one magnet is affected by its neighbors, and how much intrinsic variability there is between the particles as a result of microstructural differences. We have also performed micromagnetic simulations to explore the remanent magnetic states, and mechanisms for magnetization reversal in these structures. Small particles have near-uniform magnetization states, while larger ones develop more complex structures such as magnetization vortices or domain walls. Good agreement is obtained between modelled and observed remanent states, taking the shape and crystal orientation into account. We are investigating in particular the behavior of multilayered nanomagnets, magneto-resistive structures, and the effects of patterning on strain in magnetostrictive films.

These nanomagnets have potential uses in ‘patterned media’, magnetic-random-access memories (MRAM) and other magneto-electronic applications. Current MRAM devices rely on bar-shaped multilayered magneto-resistive nanomagnets in which a bit of data is stored depending on the relative orientation between the magnetization of the different magnetic layers in the structure. An alternative possibility for high-density MRAMs is to use a ring-shaped nanomagnet, in which a bit of information is stored by magnetizing the ring clockwise or counterclockwise.

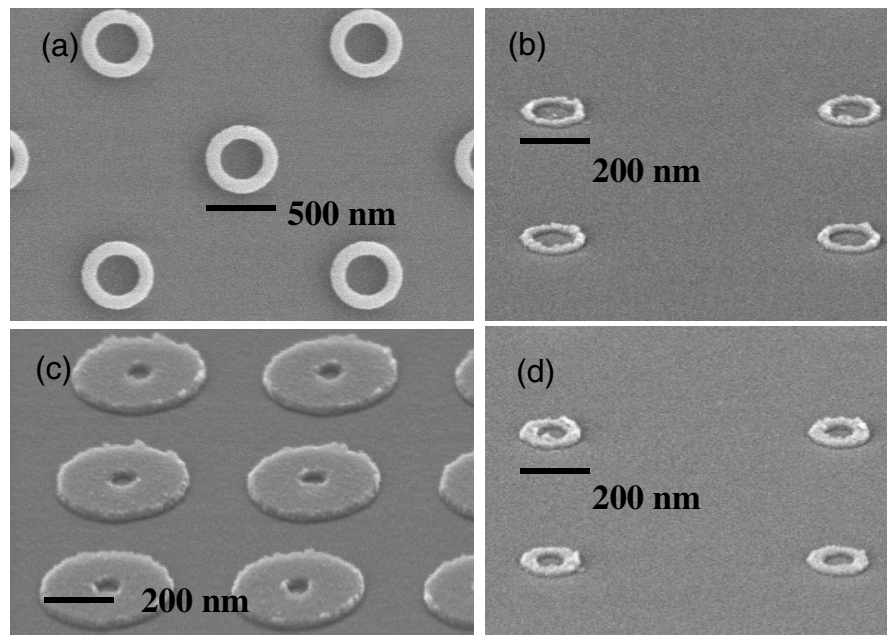


Figure 1: Plan-view and tilted scanning-electron micrographs of four arrays of Co rings with diameters and linewidths of (a) 520 nm and 120 nm, (b) 190 nm and 30 nm, (c) 360 nm and 160 nm, (d) 180 nm and 50 nm.

As an example, we have explored, for the first time, the magnetic switching mechanisms of rings with deep sub-micron dimensions (see Figure 1). The experimental results reported to date on micron-sized ring magnets support the existence of just two different magnetic states: one being the flux-closure or ‘vortex’ state (with clockwise or counter-clockwise magnetization) and the other a state with two domain walls, known as an ‘onion’ state. Unexpectedly, we found that magnetic rings with small diameters display new metastable states, called twisted states, consisting of a vortex state containing a 360° wall. The existence of twisted states in nanorings has interesting consequences for the design of magnetoelectronic devices. We are measuring the magnetoresistance of these structures with the aim of incorporating them into magnetic memory or logic devices.

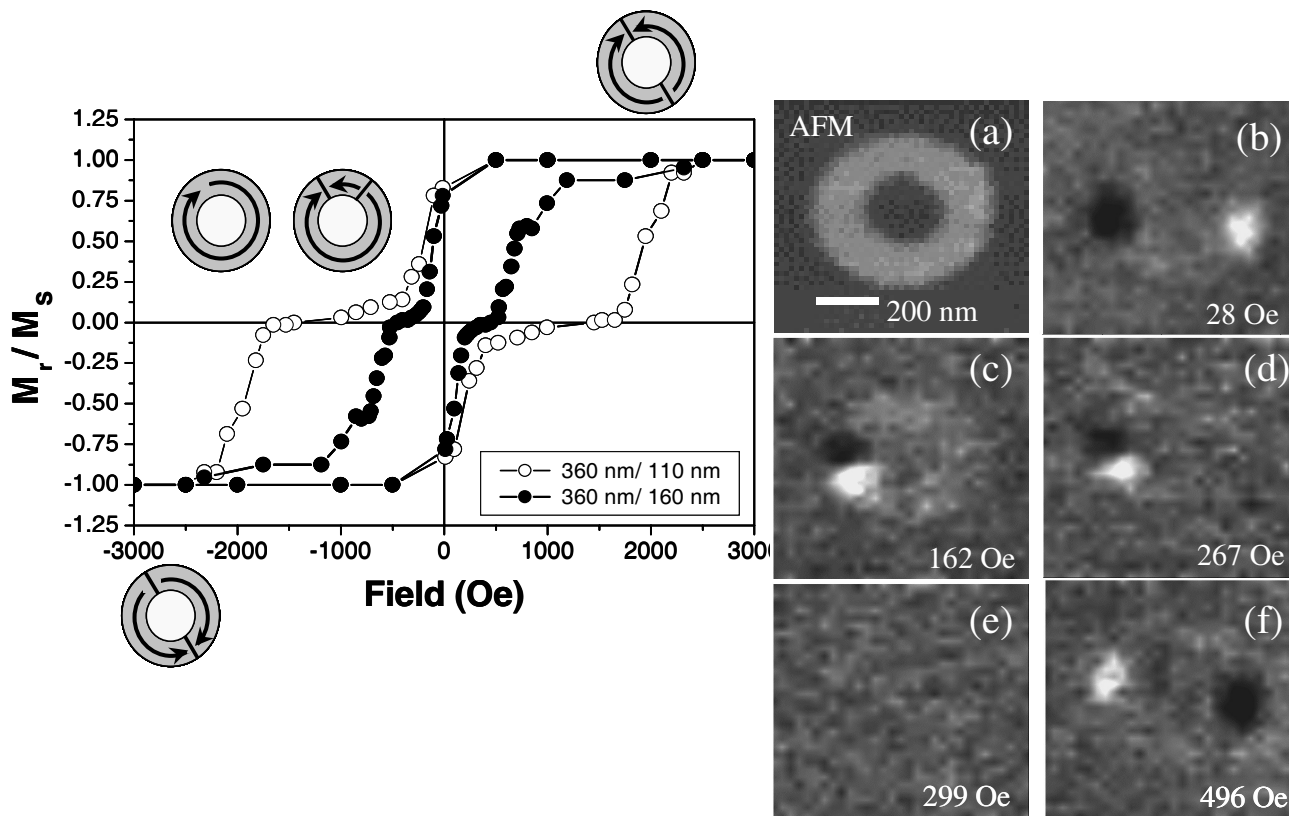


Figure 2: At left, hysteresis loops calculated from magnetic force microscopy data, as well as a schematic representation of the different magnetic states present in Co nanorings with outer diameter of 360 nm and widths of 110 nm and 160 nm (onion state, top right and bottom left; twisted and vortex states at center). On the right, data from a 520 nm-diameter ring: (a) an atomic force micrograph. (b-f) a sequence of MFM images measured at remanence after first saturating the sample at 1000 Oe, then applying and removing a reverse field of (b) 28 Oe, (c) 162 Oe, (d) 267 Oe, (e) 299 Oe and (f) 496 Oe. After saturation, the ring is in an onion state which is characterized by dark and light contrast at opposite sides of the ring originating from the two domain walls. At a reverse field of 299 Oe, the ring ‘disappears’ from the image as a vortex state forms, Fig. 2(e). However, over a range of fields smaller than that needed to produce the vortex state, a new state is visible, which we call a twisted state. This state, which can be seen in Fig. 2(c) and (d), is characterized by adjacent light and dark contrast at one side of the ring. Fig 2(f) shows the reversed onion state.

20. Templated Self-Assembly

Sponsors

National Science Foundation

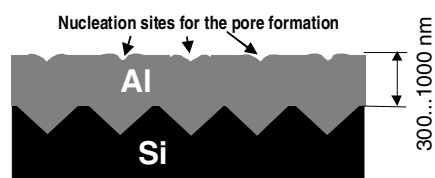
Project Staff

Professor Caroline A. Ross, Professor Henry I. Smith, Professor Carl Thompson, Dr. F. Ross (IBM), Dr. J. Floro (Sandia NL), F. Frankel, Dr Kornelius Nielsch, Michael Walsh, A. Gierman

Self-organizing systems can be used to create fine-scale periodic patterns with good short-range order. However, the long-range order of such patterns is typically poor, limiting their usefulness in nanoscale structures or devices. In this new project, methods are being developed to induce long-range order in self-assembled systems patterning the substrate with a lithographically defined periodic structure. This approach is called ‘templated self-assembly’. Patterning is carried out by topographically or chemically modulating a substrate using interference lithography, which can pattern large areas of a substrate with periodic features of ~100 nm dimension. The periodically-modulated substrate then provides long-range order to the self-organized system. The overall goal of the project is to develop methods by which nanoscale patterns can be created using a combination of ‘conventional’ lithography and self-assembly. Of particular interest is how the quality of the assembly is affected by the relative length-scales of the template and the natural period of the self-assembled system.

This approach is being applied to several different physical systems in order to understand how different types of substrate modulation can be used to create nanostructures with long-range order. Examples include the phase-separation of block copolymers (see under ‘Block Copolymer Lithography’), the formation of pores in alumina during anodization, the growth of strained SiGe quantum dots on Si substrates by chemical vapor deposition, and the agglomeration (‘dewetting’) of metal films on oxide surfaces. An example is shown below which illustrates how the pores in anodized alumina, which typically form with a hexagonally-close-packed arrangement, can be formed instead in a square array. This is achieved by depositing an aluminum film over a substrate that has been patterned with a square array of pyramidal indentations, created by interference lithography and anisotropic etching.

Al layer on a nanopatterned Si surface with an inverted pyramid structure



Al₂O₃ pore structure after the anodisation process

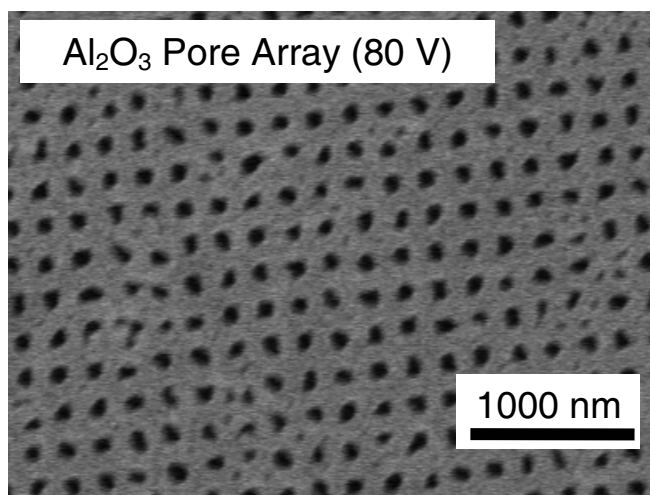
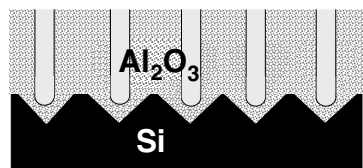


Figure 1. To make a film of anodized alumina containing a regular arrangement of pores, we start by patterning a silicon substrate with a square array of inverted pyramids, using interference lithography. The substrate is then coated with Al, which conforms to the surface topography. The aluminum film is then anodized (at 80V in this case), and the indentations in the aluminum act as nucleation sites for pores. A film of porous alumina grows containing a square array of pores.

21. Block Copolymer Lithography

Sponsors

National Science Foundation through the MIT Center for Materials Science and Engineering

Project Staff:

Professor C.A. Ross, J. Cheng, Professor H. I. Smith, and Professor E.L. Thomas, Professor G. J. Vancso

Fabrication of large-area periodic nanoscale structures using self-organizing systems is of great interest because of the simplicity and low cost of the process. Block copolymers consist of polymer chains made from two chemically distinct polymer materials. These can self-assemble to form small-scale domains whose size and geometry depend on the molecular weights of the two types of polymer and their interaction. The domains have a very uniform distribution of sizes and shapes. We have been using block copolymers as templates for the formation of structures such as magnetic particles, by selectively removing one type of domain and using the resulting template to pattern a nanostructured magnetic film. An example is shown in Fig. 1, where Co dots have been made using ion milling to pattern a Co film. The structure has a center-to-center spacing of ~ 50 nm.

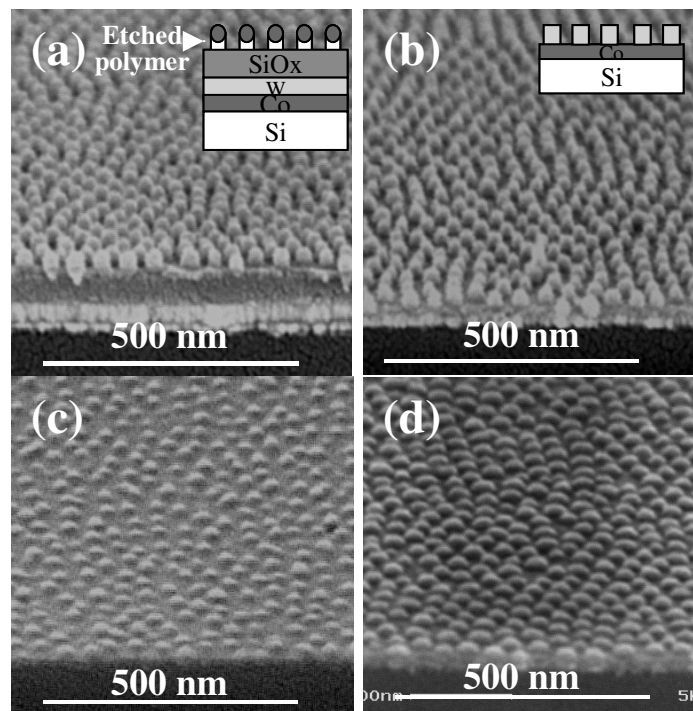


Figure 1. Cross-sectional SEM micrographs of (a) Block-copolymer lithographic template on the multilayer film. (b) W hard mask (dots) on continuous Co film. (c) Co dots after Ar ion milling. (d) Co dots after Ne ion milling.

However, the self-assembled block copolymer lacks long-range order (Figure 2(a)). Templated self assembly is used here to induce orientation and positional ordering of the block copolymer through artificial surface patterning. Block copolymers have been spin-cast on the silica grating substrates which were patterned using interference lithography. For the block copolymer PS/PFS 50/12, well-ordered structures form in the grooves of the gratings with all the close-packed rows aligned within the grooves (Figure 2(b)), provided the groove width is comparable to the 'grain size' of the block copolymers. We have found that the number of rows within the groove, the spacing of the rows, and the deliberate introduction of defects such as vacancies and dislocations, can be controlled by adjusting the groove dimensions. These ordered nanostructures may be useful as templates for a variety of applications.

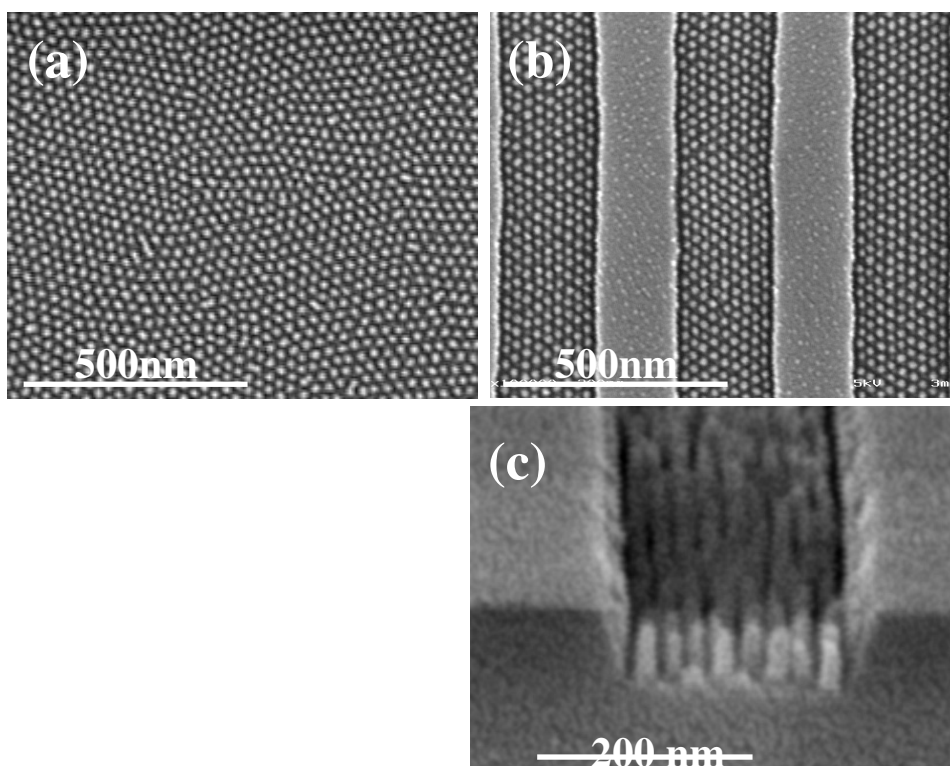


Figure 2. (a) PS/PFS block copolymer 50/12 on the flat silica substrate. (b) Ordered block copolymer PS/PFS 50/12 forms an ordered structure in 260nm-wide silica grooves fabricated by interference lithography and reactive-ion etching. (c) Ordered array of silica pillars, formed by etching using the ordered block copolymer as a template.

22. Transmission Gratings for X-ray and Atom-Beam Spectroscopy and Interferometry.

Sponsors

X-OPT, Inc.

Project Staff

James M. Carter, Timothy A. Savas, Edward Murphy, Professor Henry I. Smith and Dr. Mark L. Schattenburg

Transmission gratings with periods of 100 to 1000 nm are widely used in applications such as x-ray, vacuum-ultraviolet, and atom-beam spectroscopy and interferometry. Over 30 laboratories around the world depend on MIT-supplied gratings in their work. For x-ray and VUV spectroscopy, gratings are made of gold and have periods of 100 to 1000 nm, and thicknesses ranging from 100 to 1000 nm. The gratings are most commonly used for spectroscopy of the x-ray emission from high-temperature plasmas. Transmission gratings are supported on thin (1 micron) polyimide membranes, or made self supporting ("free standing") by the addition of crossing struts (mesh). (For short x-ray wavelengths, membrane support is desired, while for the long wavelengths, a mesh support is preferred in order to increase efficiency.) Fabrication is performed by interference lithography combined with reactive-ion etching and electroplating. Progress in this area tends to focus on improving the yield and flexibility of the fabrication procedures.

Another application is the diffraction of neutral-atom and molecular beams by mesh-supported gratings. Lithographic and etching procedures have been developed for fabricating free-standing gratings and grids in thin silicon nitride (SiNx) membranes supported in a Si frame. Figure 1 shows a free-standing 100 nm-period grating in 100 nm-thick silicon nitride. Figure 2 shows a 100 nm-period grid in a 100 nm-thick SiNx membrane. Such a grid is used in experiments as a "molecular sieve."

We have established a collaboration with the Max-Planck Institute in Göttingen, Germany, in which they utilize our gratings of 100 nm period in diffraction experiments using atomic, molecular, and helium-cluster beams. As shown in Figure 3, the diffraction of atomic and molecular beams reveals striking deviations from Kirchhoff's optical diffraction theory. The analysis of the diffraction intensities enabled a quantitative determination of the attractive van der Waals interaction between the silicon nitride surface and various atomic and molecular species, including He, Ne, Ar, Kr, He*, Ne*, D₂, and CH₃F. The diffraction of cluster beams by a transmission grating has been established as a unique technique for the non-destructive mass selection and detection of small and weakly bound van der Waals clusters. Recently, the Göttingen group discovered bound states in mixed-isotope helium clusters, e.g. ³He⁴He₂, ³He⁴He₃, etc., by diffraction from one of our 100-nm-period gratings as shown in Figure 4. In addition, they employed the grating to measure the bond length of the helium dimer, ⁴He₂, which is assumed to be the weakest molecular bond. Future experiments based on the transmission gratings include the study of cluster formation dynamics and the search for the Efimov effect in the helium trimer.

Data obtained by helium-atom-beam diffraction at large incident angles showed Lyman ghosts in the spectrum. This data led to the development of new fabrication techniques to improve the quality of the free-standing gratings in silicon nitride. Diffraction spectra from gratings made with the improved process show no Lyman ghosts, illustrating the important synergy between applications and nanofabrication.

Successful diffraction experiments with beams of buckyballs (C₆₀) have been carried out with our 100 nm-period, free-standing SiNx gratings by Dr. Markus Arndt of the University of Vienna. In addition, our 100 nm-period, free-standing SiNx gratings can be lightly coated with metal. Prof. Herman Batelaan of the University of Nebraska-Lincoln has used such gratings in highly-successful diffraction experiments with beams of 500 eV electrons.

Our 100 nm-period free-standing SiN_x gratings are also used for atom interferometry by two groups: those of Prof. Alexander Cronin of the University of Arizona and Prof. Bruce Doak of the State University of Arizona. Cronin's group interferes neutral beams of sodium atoms while Doak's group interferes helium beams (performed at the Max Planck Institute in Göttingen, Germany in collaboration with P. Toennies).

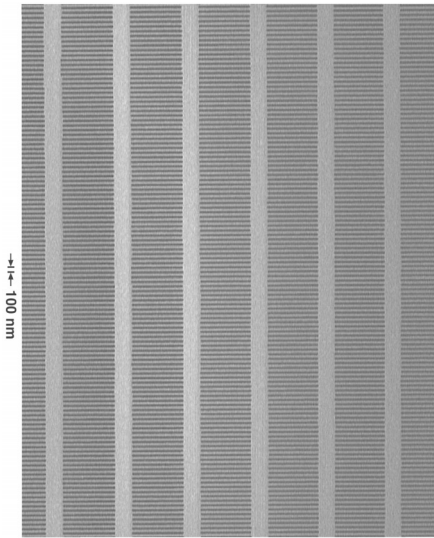


Figure 1. Scanning electron micrograph of a free-standing 100 nm-period grating (50 nm-wide bars) in a silicon nitride membrane of area 500 microns by 5 mm.

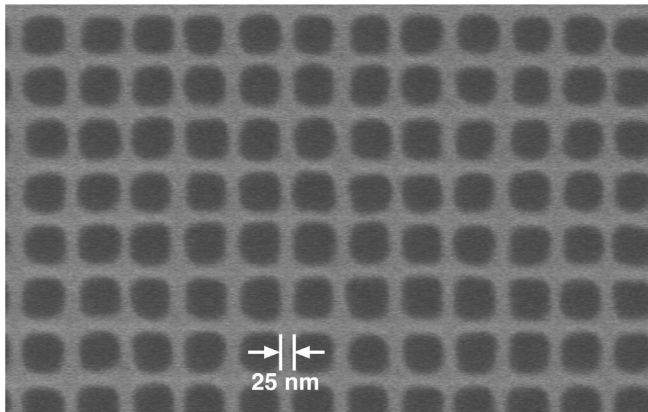


Figure 2. Scanning electron micrograph of a free-standing 100 nm-period grid in a silicon nitride membrane of area 500 micron by 5 mm. Such grids are used in experiments to separate out Helium trimers from other clusters.

Rare Gas Atomic Beam Diffraction Patterns at 300 K for Normal Incidence

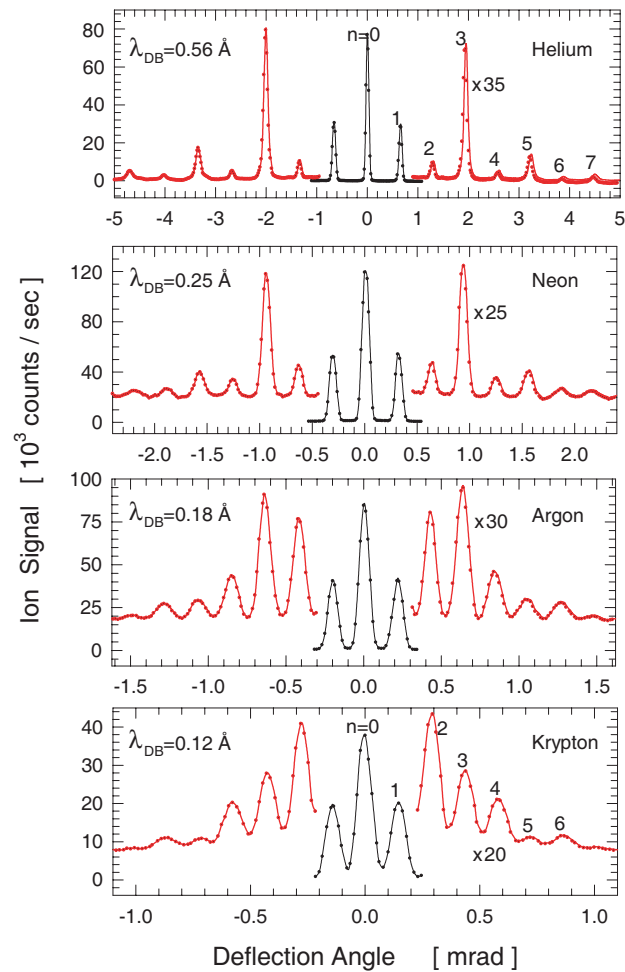


Figure 3. Rare-gas atom-beam diffraction patterns. These results were obtained by Wieland Schöllkopf and Peter Toennies at the Max-Planck Institute in Göttingen, Germany, using a free-standing, 100nm-period grating.

Mixed ^4He - ^3He -Isotope Clusters Discovered by Diffraction
from 100 nm-Period-Grating at $T_0 = 5\text{ K}$, $P_0 = 1\text{ bar}$

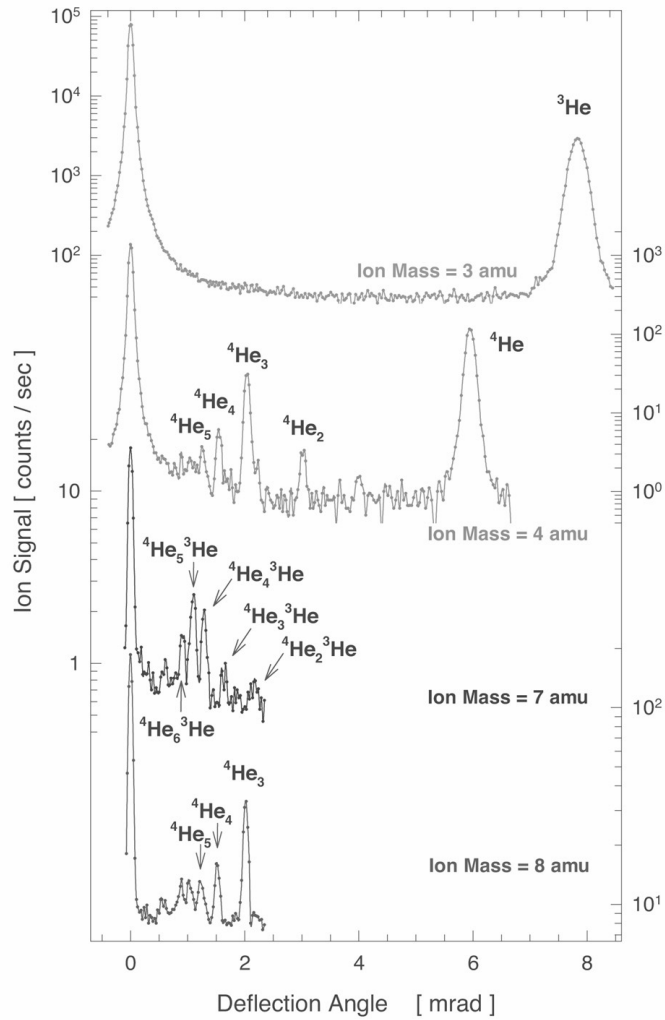


Figure 4. Non-destructive mass separation of small mixed-isotope helium clusters. These results were obtained by Peter Toennies, et al, at the Max-Planck Institute in Goettingen, Germany, using free-standing, 100 nm-period gratings made in the NSL at MIT.

23. Nanofabricated Metal Transmission Gratings

Sponsors:

NASA (NAG5-5405) and XOPT, Inc.

Project Staff:

James Carter, Robert C. Fleming, Edward Murphy, Dr. Mark L. Schattenburg, Professor Claude R. Canizares and Professor Henry I. Smith

Wire-grid metal transmission gratings have many useful and novel optical properties that are enhanced when the grating period and/or slit dimensions approach or go below the wavelength of light. These benefits are particularly attractive in the UV and x-ray bands where the performance of conventional optics is poor. This benefit generally requires control of the grating period and feature dimensions in the nanometer to picometer range. In this research effort we are advancing metal transmission gratings past the already sophisticated technology developed at MIT over the past 20 years.

Our research group is the world leader in metal transmission grating fabrication technology and has used them to a wide variety of laboratory and space research applications. Over forty laboratories worldwide use MIT-fabricated transmission gratings for research, ranging from materials science to laser plasma fusion (see Table 1). Nine NASA missions have also utilized hundreds of MIT-fabricated transmission gratings in space research instruments ranging from x-ray spectrographs to atom imagers.

Metal transmission gratings are generally fabricated with electroplated gold and supported by submicron-thick polyimide membranes or coarse meshes of electroplated gold or nickel. The thin and fragile grating members require a carefully engineered coarse support mesh and metal frame to withstand the rigors of rocket launch and space environment. Transmission grating periods down to 100 nm and sizes up to 30x30 mm have been fabricated. Grating patterning is performed by interference lithography (IL) using a variety of novel tri-level resists schemes, followed by reactive-ion etching and metal electroplating. The combined resources of the MIT Nanostructures Lab (NSL) and Space Nanotechnology Lab (SNL) have been used to develop the most advanced IL tools in the world for high-yield volume production of transmission gratings.

High-dispersion x-ray and extreme ultraviolet (EUV) transmission gratings were fabricated for NASA missions including the *Solar EUV Monitor* (SEM) on the *Solar and Heliospheric Observatory* (SOHO) mission, launched December 2, 1995, the *Chandra* x-ray telescope, launched July 23, 1999, and the *Geostationary Operational Environmental Satellites* (GOES N-Q or 13-16) missions. The *Chandra* telescope provides high-resolution imaging and spectroscopy of x-ray-emitting astrophysical objects, with unprecedented power and clarity, which is significantly widening our view of the Universe. The SOHO and GOES satellite series perform solar EUV monitoring which provides early warning of solar flare events that could imperil satellite and astronaut operations.

A scanning-electron micrograph of a 200 nm-period gold grating from the *Chandra* mission is shown in Fig. 1. This grating is used in the High Energy Transmission Grating Spectrometer (HETGS) which provides high-resolution x-ray spectroscopy in the $\lambda = 0.1\text{-}14$ nm band. Period control of 40 picometers was required to meet telescope resolution requirements. Figure 2 is an example of an x-ray spectrum obtained by *Chandra* using our gratings.

Transmission grating filters were also fabricated for the *Medium Energy Neutral Atom* (MENA) instrument on the NASA *Magnetospheric Imaging Medium-Class Explorer* (IMAGE) mission, launched March 25, 2000, and also for the NASA *Two Wide-Angle Imaging Neutral-atom Spectrometers* (TWINS A, B) Missions. Instruments on these missions provide neutral atom imaging of Earth's magnetosphere. Transmission gratings are used to block the intense Hydrogen Lyman Alpha ($\lambda = 121.6$ nm) deep-UV radiation that would otherwise overwhelm the sensitive atom detectors. Figure 3 depicts a 200 nm period

atom nanofilter grating with 45 nm-wide slots, designed to block deep-UV radiation. Slot widths need to be controlled to within a few nanometers for optimal UV blocking.

The current research effort seeks to boost grating transmission efficiency, reduce defect levels, and improve control of grating feature geometry.

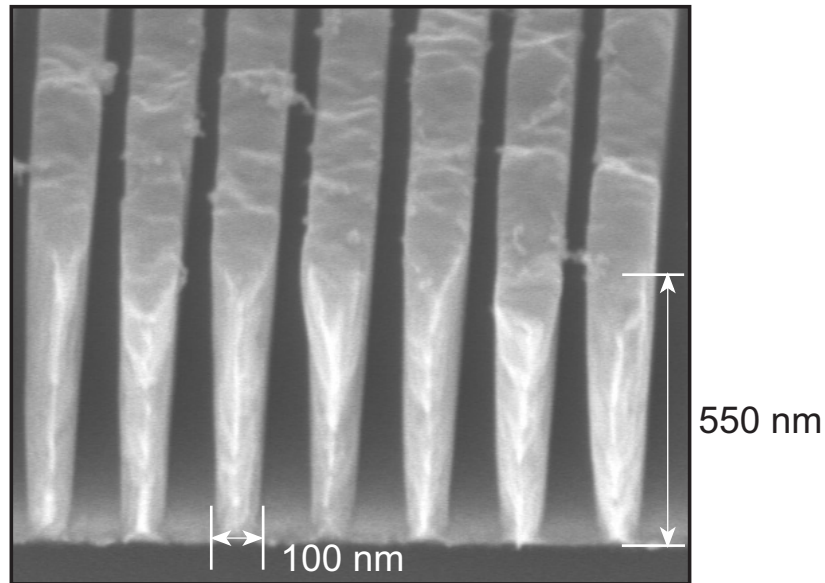


Figure 1: Scanning-electron micrograph of a 200 nm-period gold x-ray transmission grating used in the HETGS instrument on the Chandra Observatory, cleaved to show the grating line sidewalls. The HETGS provides high-resolution x-ray spectroscopy in the $\lambda = 0.1\text{-}14$ nm band. The gold bars are 100 nm wide, or approximately 400 gold atoms.

Chandra Observatory X-ray Spectrum of Binary Star Capella

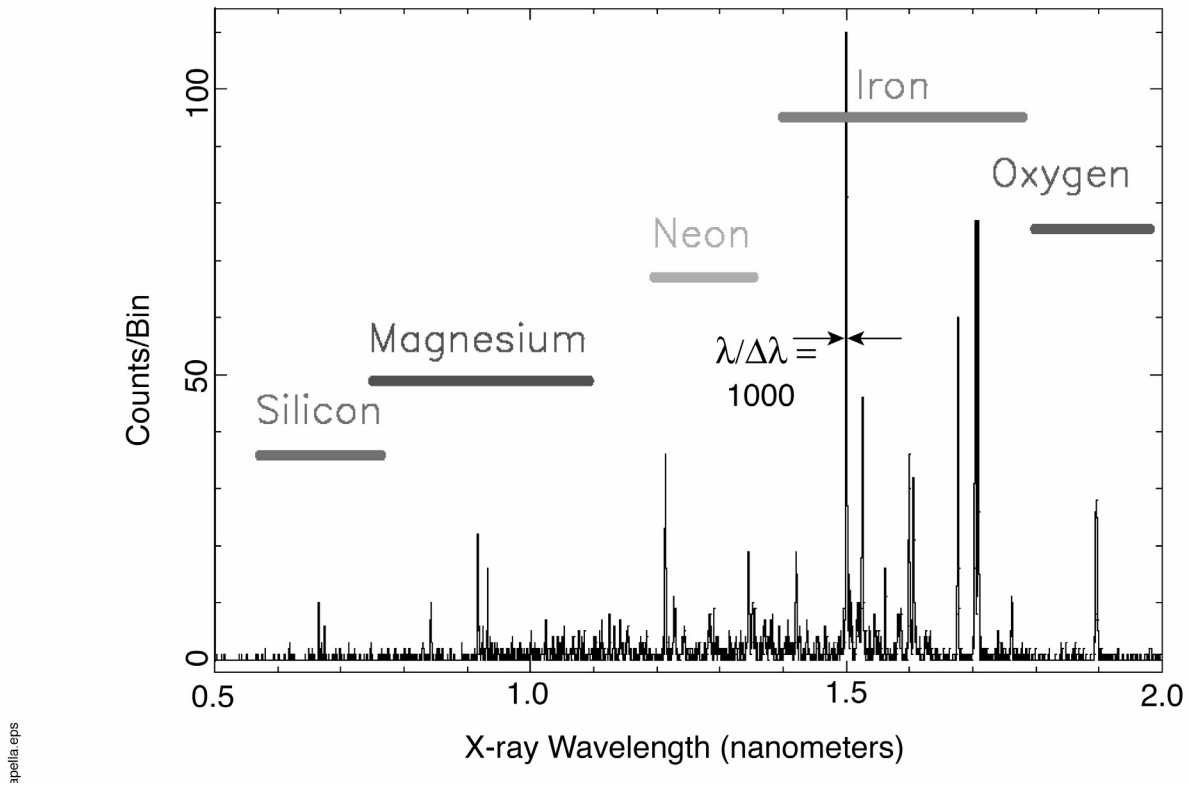


Figure 2: X-ray spectrum of the binary star Capella obtained via our gold diffraction gratings on the Chandra x-ray astronomy satellite.

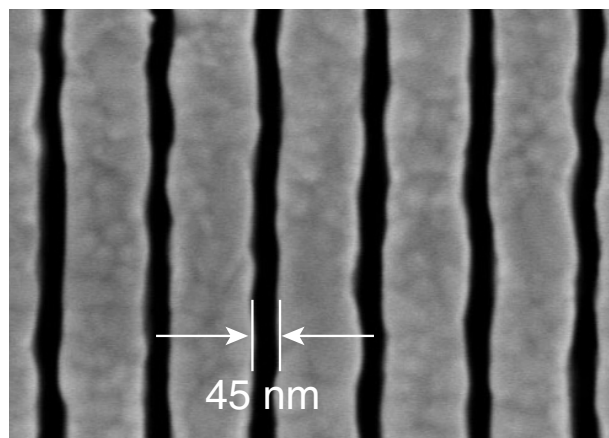


Figure 3. Scanning-electron micrograph of a deep-UV blocking grating used in atom telescopes on the NASA IMAGE and TWINS missions. The grating blocks deep-UV radiation while passing energetic neutral atoms. Due to the narrow slot width of 45 nm and the large slot depth (~500 nm), the UV transmission is extremely low ($\sim 10^{-6}$ at $\lambda = 121.6$ nm), while decreasing the transmitted atomic flux by only a factor of 10.

Table 1. *Laboratories supplied with SNL-fabricated gratings and lithography calibration standards.*

Aerospace Corporation (P. R. Strauss)	Lawrence Livermore National Laboratory (Nat Ceglio)
Avance Inc., Japan (Yachiyo Kimpara)	Lawrence Livermore National Laboratory (Joseph Nilsoen)
AWE Aldermaston Goods Inwards (Richard T. Eagleton)	Los Alamos National Laboratory (Earl Scime)
BESSY-Zentrales, Berlin, Germany (H.R. Molter)	Los Alamos National Laboratory (Gary Stradling)
Commonwealth Technology (John Seely, Drew Fielding)	Los Alamos National Laboratory (Jim Cobble)
Danish Space Research Institute (Herb Schnopper)	Los Alamos National Laboratory (Peter Lee)
Duke University (Louis Johnson)	Martin Marietta/Oak Ridge (J. A. Stokes)
Etablissement de Bruyeres-le-Chatel, France (Michele Courtin)	Max Planck Institute for Quantum Optics (Eidman)
Foreign Economic Association, Russia (Akademintorg)	Max Planck Institute fur Biophys. Chemie (Kuhnle)
French Atomic Energy Commision (B. Erlinger)	Max Plank Gesellschaft at the Friedrich-Schiller Universitaet (Eckhart Foerster)
Hampshire Instruments (Irving Plotnik)	MIT (Prof. Pritchard)
Hampshire Instruments (Robert Frankel)	MIT Nuclear Engineering Lab (Eugene DiSalvatore)
Indian Dept. of Atomic Energy (K. Visvanathan)	National Synchrotron Light Source - Brookhaven (David Eaterer)
John Hopkins University (Vlad Soukhanovskii)	Panametrics Corp. (Frederick Hanser)
Kernforschungszentrum Karlsruhe GmbH (H. Tebbert)	Pennsylvania State University (Gordon Garmire)
Laboratory for Laser Energetics, Rochester University (Fred Marshall)	Sandia National Laboratory (Larry Ruggles)
Laboratory for Laser Energetics, Rochester University (Justin Peatross)	Sandia National Laboratory (Tina Tanaka)
Lawrence Berkeley National Laboratory (Eric Gullikson)	Sandia National Laboratory (John Porter)
Lawrence Berkeley National Laboratory (Phil Heiman)	Stanford Synchrotron Radiation Laboratory (Pierro Pianetta)
	University of Florida (Chuck Hooper)
	University of Illinois at Chicago (G. Gnutek)
	University of Southern California (Howard Ogawa)
	US Department of Energy (J. Snyder)

24. Nanofabricated Reflection Gratings

Sponsors

NASA (NAG5-5405, NAG5-12583), Chromaplex Corp.

Project Staff

James Carter, C.-H. Chang, Robert C. Fleming, Dr. Ralph Heilmann, Edward Murphy, Dr. Mark L. Schattenburg, Professor Claude R. Canizares and Professor Henry I. Smith

Grazing-incidence x-ray reflection gratings are an important component of advanced high-resolution spectrometers and other x-ray optics. These have traditionally been fabricated by diamond scribing with a ruling engine or by interference lithography followed by ion etching. These methods result in gratings which suffer from a number of deficiencies, including high surface roughness and poor groove profile control, leading to poor diffraction efficiency and large amounts of scattered light.

We are developing improved methods for fabricating blazed x-ray reflection gratings which utilize special (111) silicon wafers, cut ~1 degree off the (111) plane. Silicon anisotropic etching solutions, such as potassium hydroxide (KOH), etch the (111) planes very slow compared to other crystallographic directions, resulting in the desired super-smooth blaze surface. Previous work used similar off-cut (111) silicon substrates to fabricate blazed diffraction gratings, but utilized a second KOH etch step that compromised the grating facet flatness and is unsuitable for small grazing-angle x-ray diffraction.

Gratings are patterned using interference lithography with the $\lambda=351.1$ nm wavelength, and transferred into the substrate using tri-level resist processing, reactive-ion etching (RIE), and silicon-nitride masking during the KOH etch. The narrow (~100 nm) ridge of silicon which supports the nitride mask is removed using a novel chromium lift-off step followed by a CF₄ RIE. The result is extremely-smooth sawtooth patterns, which, after applying a thin evaporative coating of Cr/Au, are suitable for x-ray reflection (see Fig.1).

We have recently begun a new effort to replicate saw-tooth gratings using nano-imprint lithography with a UV-curable polymer (see Fig. 2). If successful, this new method promises to significantly reduce the cost of grating fabrication.

Potential applications of these improved gratings are for materials science research with synchrotron radiation and satellite-based high-resolution x-ray spectroscopy for planned NASA missions such as *Constellation X*. We are also exploring other applications for this technology, including telecom devices and atom microscopy.

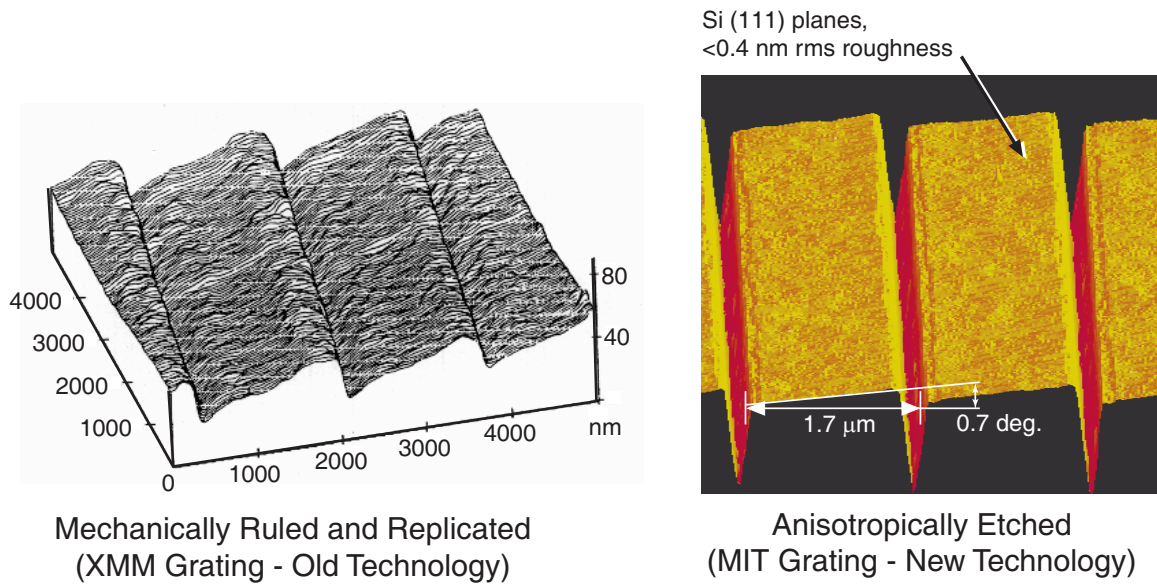


Figure 1. (a) An AFM image of a traditional mechanically-ruled and replicated x-ray reflection grating (Bixler et al., *Proc. SPIE* **1549**, 420-428 [1991]). Note the rough, wavy grating surfaces that lead to poor diffraction performance. (b) An AFM image of a blazed x-ray reflection grating fabricated by anisotropic etching of special off-cut (111) silicon wafers. Note the improvement of grating surface flatness and smoothness, leading to significantly improved performance.

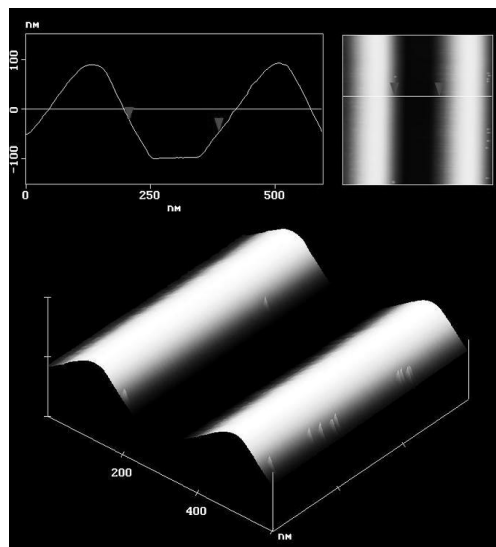


Figure 2. AFM image of nano-imprinted grating. Profile is far from ideal at this stage.

25. X-ray Foil Optics Shaping Technology

Sponsors

NASA (NAG5-5405, NAG5-12583), QED, Inc.

Project Staff

M. Akilian, C. Forest, Dr. R. Heilmann, Y. Sun, Professor C.R. Canizares, Dr. G.R. Ricker and Dr. M.L. Schattenburg)

Future x-ray astronomy missions will require orders-of-magnitude improvement in collecting area and resolution. Thin-foil optics are attractive candidates for x-ray telescopes because of the tremendous weight and cost savings which can be achieved compared to traditional monolithic optics. However, substantial improvement in our ability to shape foils to high accuracy is required. In this research program we are developing technology for high-volume shaping of thin (~0.5 mm) glass and silicon substrates, including both reflective and diffractive components.

Over the last several years we have developed methods for thermally shaping glass sheets. This process involves heating the sheet in a furnace until it begins to slump, conforming to quartz or silicon mandrels that have been lithographically patterned with thousands of pins. The pins reduce the surface area of the mandrel to minimize sticking and mitigate the effects of dust particles. We are also developing an alternative slumping method based on air bearings.

We are also developing a complementary shaping process called block lapping. This novel process involves the bonding of foils to rigid polishing blocks, while in their relaxed state, using special UV-cured epoxies and thermoplastics. The bonded foils are then mechanically polished into the desired shape.

A third method involved a process called magneto-rheologic fluid polishing (MRF) to deterministically shape the surface of the substrate. A magnetic polishing compound is entrained onto a spinning sphere that is scanned over the substrate. A magnetic field stiffens the fluid in a confined area generating high shear polishing forces. This method requires an accurate surface error map as input to the MRF shaping machine.

A critical component of this research is accurate surface metrology of thin foils. We are developing a variety of Hartmann and Shack-Hartmann surface metrology tools for this purpose, and special fixturing that holds the sheets during metrology while minimizing holding torques and gravity distortions.

Our short-term goal is to develop foil shaping technology with sub-500 nm accuracy. This will enable a number of important NASA missions such as *Constellation X*. Our long term goal is to realize sub-20 nm shaping accuracy, which will enable diffraction-limited x-ray imaging with resolution improved ~1000X more than today's telescopes.

26. **Nano-Accurate Assembly Technology for X-ray Foil Optics**

Sponsors

NASA (NAG5-5405, NAG5-12583, NCC5-633)

Project Staff

M. Akilian, C. Chen, C. Forest, Dr. R. Heilmann, Y. Sun, Professor. C.R. Canizares and Professor A. Slocum, Dr. G.R. Ricker and Dr. M.L. Schattenburg

Future x-ray astronomy missions will require orders of magnitude improvement in collecting area and resolution. Foils optics are attractive candidates for x-ray telescopes because of the tremendous weight and cost savings which can be achieved compared to traditional monolithic optics. However, substantial improvements in our ability to assemble foils with high accuracy are required. In this research program we are developing microstructures to assemble foil optics, including both reflective and diffractive components.

Plasma micromachining is used to lithographically fabricate silicon “microcombs” designed to guide and register silicon and glass foils into precise three-dimensional shapes with sub-micron accuracy. Thousands of ~500 μm -thick foils are typically required in an x-ray telescope, each shaped and assembled to form the precise curves or flats that focus x-rays by grazing-incidence reflection. Fig. 1 shows SEM images of two types of microcombs under development.

A prototype flight mirror structure based on these principles has been built and tested. Test results show that glass sheets are assembled to a repeatability of ~0.3 micron, corresponding to an angle error of <1 arc-second. This accuracy exceeds previous foil assembly methods by a factor of ~100. Our microstructure technology is being supported by NASA as the baseline technology for assembling foil optics in the *Constellation X* telescope.

Recent effort seeks to improve the accuracy of the microcombs from the current level of ~200 nm to under 100 nm. With further progress it may be possible to achieve diffraction-limited x-ray imaging, which can potentially improve the accuracy of telescopes by over 1000X.

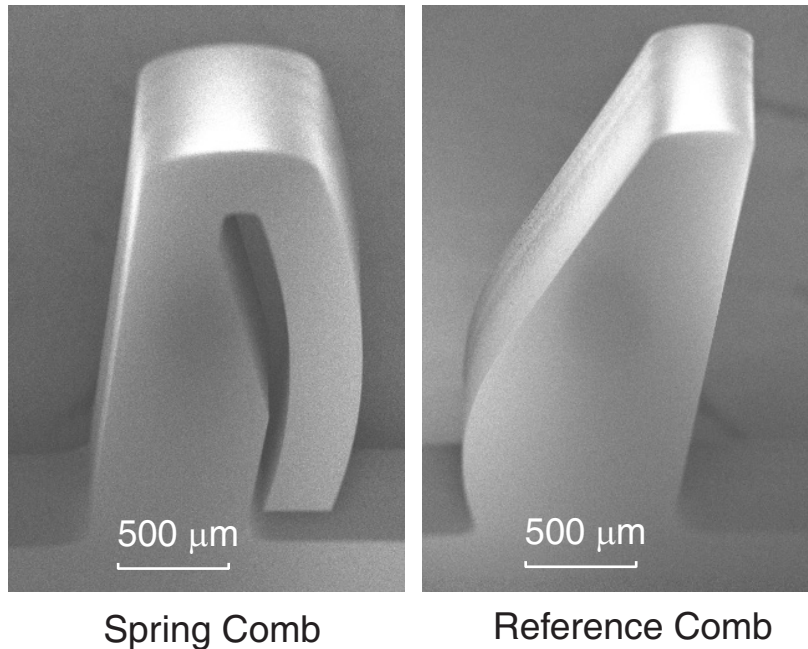


Figure 1. Electron micrographs of silicon microcombs. Teeth are ~500 μm wide. a) Spring comb. b) Reference comb.

27. **Functional 3D Nanostructures achieved via Folding of 2D Membranes**

Sponsors

National Science Foundation, 6894464

Project Staff

Stanley M. Jurga, Carlos H. Hidrovo-Chavez, Professor George Barbastathis, Professor Henry I. Smith

Functional three-dimensional (3D) nanostructures are of interest in numerous technological domains. The 3rd dimension promises to extend micro processors and memories beyond “the end of Moore’s law,” *i.e.* when feature sizes of planar electronics reach their minimum practical limit. In applications other than electronics, the need to conquer the 3rd dimension is even more urgent. Examples include optical elements that integrate sensing and processing for defense or commercial applications, miniature reactors for chemical and biochemical analysis, drug delivery by miniaturized microfluidic implants, micromechanical and nanomechanical energy storage elements, and environmental monitoring and industrial quality control applications. However, 3D fabrication is not well understood and developed. Our research is aimed at a specific method for 3D fabrication and assembly, which we refer to as “membrane folding.”

Our approach is a two step process designed to satisfy the following functional requirements: (a) integration of dimensional scales from the nano to the micro and beyond; (b) maximum utilization of existing fabrication tools; and (c) flexibility in achieving a large number of possible 3D configurations with minimum cost and maximum repeatability and yield. In the first step, all devices are fabricated on a planar substrate just as they are in today’s semiconductor industry. In the second step, the planar substrate is folded into a 3D structure as depicted in Figure 1. Designated compliant zones act as hinges between stiffer regions that contain micro and nano devices. By virtue of compliant circuitry that

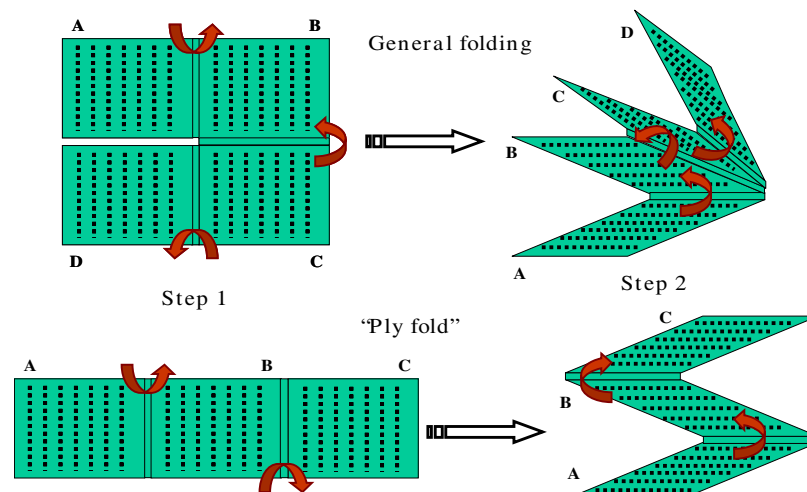


Figure 1. Examples of how 3D structures can be obtained by folding pre-fabricated thin 2D membranes in a two-step process. Black dots denote surface features nanofabricated on the membrane surface.

spans the hinge areas, full 2D connectivity is preserved across the entire length after folding. This is important for electronics as well as communication in MEMS sensors and actuators and integrated nano devices. Connectivity is also achieved in the vertical, 3rd direction by designing

vertical connections to be formed when the planar folds reach predetermined locations during folding. At present, our study aims to build 3D diffractive-optical elements (3D-DOEs) as a case study in the technology development for folded-membrane devices. 3D-DOEs promise better performance in terms of efficiency and angular selectivity than traditional 2D diffractive-optical elements. Spacing multiple diffractive gratings or Fresnel zone plates (perhaps as many as 50) vertically above one another establishes a matched filter with very high efficiency. Although such a 3-D structure could be fabricated one layer at a time, the folded-membrane approach should be far more cost effective. Also, the folded membrane approach may enable tuning of the diffractive optical systems, for example, by electrically varying the spacing of the stack.

In our preliminary work, we have demonstrated a single 180 degree fold in a silicon-based device with magnetic-actuation-induced folding (Figure 2). The gold hinges are plastically deformed so that the folded membrane remains near 180 degrees. Electron beam evaporated gold was chosen for the compliant hinges due to its high ductility and comparatively small spring back angle. The hinges also complete a current loop around the perimeter of the membrane. By placing the device in a magnetic field and controlling the magnitude of current in this loop, a Lorentz force is generated that rotates the flap about its hinges. The Lorentz force is highly controllable and thus allows extensive experimental characterization of the mechanics of folding in our device. In the future, we will also explore other means of actuation such as stress and chemically-induced folding. Some of these alternatives are more attractive than the magnetic method from the point of view of alignment and flexibility in 3D assembly schemes.

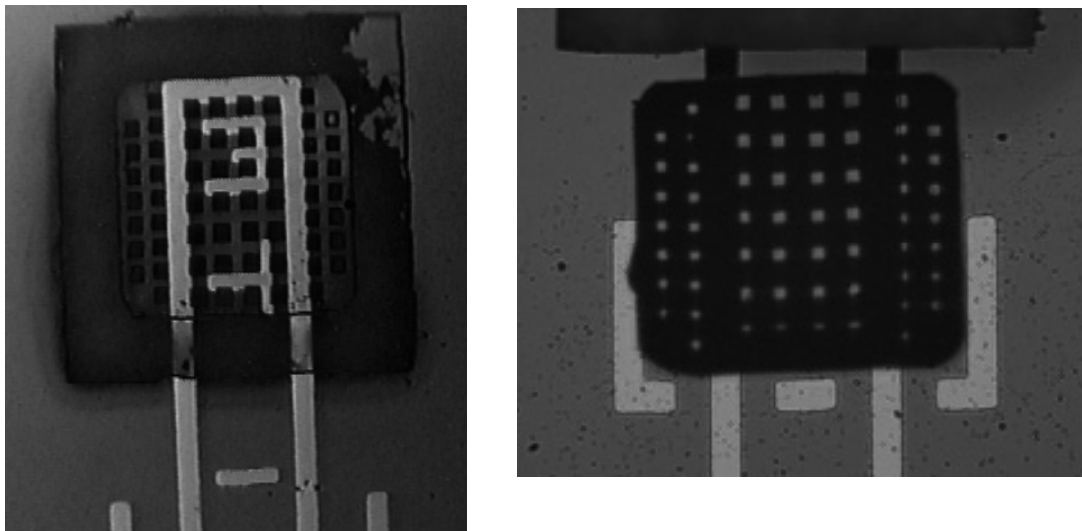
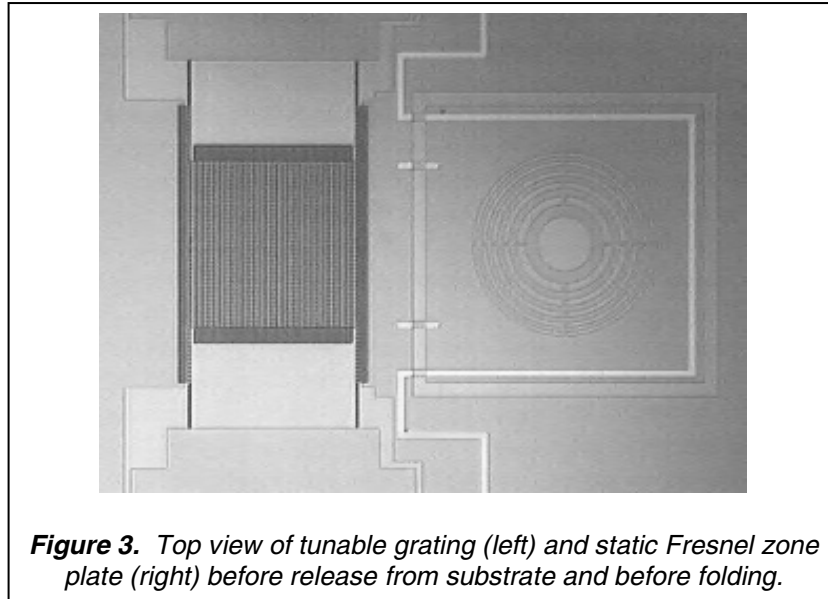


Figure 2. Membrane flap before folding (left) and after folding to 180 degrees (right). Note the alignment tolerance achieved in folding (alignment fiducials are $50\mu\text{m}$ wide).

The first 3D diffractive device is displayed in its unfolded state, still attached to the substrate in Figure 3. Electrostatic combdrives tune the period of the binary grating, which changes the angle of the diffracted orders. The Fresnel zone plate (essentially a diffractive lens) will be folded over and aligned to the grating as a demonstration of compound diffractive optics in 3D.



Future work will focus on the final alignment and latching of the folds in addition to new actuation methods for folding that could be categorized as templated-self-assembly. Work in implementing multiple folds and studying their behavior is also underway. These steps are the formative building blocks for establishing a multi-use platform. 3D assembly through folding lends itself to broader goals such as combining discrete devices of varied functionality (optics, electronics, microfluidics, etc) into one cohesive, self-contained system capable of multiple tasks such as advanced sensing and response.

28. Strain-tunable Photonic Band Gap Microcavity Waveguides at 1.55 μm

Sponsors:

KIMM, Microphotonics Center

Project Staff:

Chee Wei Wong, Minghao Qi, P. Rakich, S.G. Johnson, Y.-B. Jeon, Professor George Barbastathis, S.-G. Kim, Professor Henry I. Smith

We have designed and fabricated tunable photonic-bandgap microcavities in optical waveguides, with strain modulation via thin-film piezoelectric actuators on deformable membranes. Cavity resonance tunability, with nanometer lattice control, is designed through perturbation on finite-difference time-domain FDTD computations. Device fabrication integrates X-ray nanolithography, piezoelectric micro-actuators and bulk micromachining.

Motivation and Device Concept

Photonic-bandgap microcavities in optical waveguides have demonstrated cavity resonances at wavelengths near the 1.55 μm band, quality factors on the order of 300, and modal volume at 0.055 μm^3 in high-index contrast Si/SiO₂ waveguides and GaAs air-bridge waveguides. Applications include zero-threshold microlasers, filters and signal routers. For tunability in Si microphotonic platforms, thermal actuation is often utilized. Compared to thermo-optics, strain-tuning via thin-film piezoelectric micro-actuators provides a significantly faster response, lower power consumption and better localization of tunability. This level of integration permits dynamic reconfiguration of the cavity resonance and band-edges, fine-tuning for fabrication mismatches, and active compensation of device arrays to external disturbances.

The conceptual design is illustrated in Figure 1. The Si microcavity waveguide is located on a deformable double-anchored SiO₂/Si membrane. The thin-film piezoelectric actuators provide sufficient driving force, under 5 V actuation, for the sub-nanometer strain control of the geometric lattice in the microcavity. Comparative designs of the double-anchored membrane have been demonstrated for analog tunable diffractive gratings. Experimental effects of static strain on coupled vertical microcavity resonators and theoretical designs for shear-modulated 2D photonic crystals on bulk piezoelectric substrates have also been reported.

Device Design

We employ first-order perturbation theory to obtain a semi-analytical result for the strain-induced shift in the cavity resonance; such methods ease the study of small modulations such as the 0.3% strain considered here. First, a closed-form solution for the hole boundary displacements is derived following classical mechanics. The material boundary displacements are then numerically meshed and employed in a perturbation-theory formulation, which involves surface integrals of the unperturbed fields (obtained by FDTD simulation) over the perturbed material boundaries. The result predicts a 0.8% shift in resonant wavelength (12.7 nm in the C-band) for a 0.3% mechanical strain from a 3D computation. This is illustrated in Figure 2a. While a 2D computation suggests similar final results in the resonant shift, the 3D computation highlights differences from the individual contributions – hole ellipticity, defect cavity length, and hole diameters – in the strain perturbation. Other effects such as photoelasticity and waveguide out-of-plane bending were found to be secondary.

Device Fabrication and Results

For resonance wavelength at 1.55 μm , the minimum feature size, located between the waveguide edges and the hole edges, is 130 nm. X-ray lithography is employed with a Cu_L source at 1.3 nm to transfer the pattern from the mask to a PMMA resist. The mask is a thin SiN_x membrane with 200 nm Au patterned with e-beam lithography. The resist image is then transferred to 50 nm of

Cr, via lift-off, and etched into a 212 nm single-crystal Si layer to form our waveguide. The microfabricated piezoelectric film has an excellent dielectric constant of 1200 and a d_{31} coefficient of ~ -100 pC/N. A fiber lens assembly is used to couple a 1.430 μm to 1.610 μm tunable laser diode source, with TE polarization and lock-in amplification, into the prepared input/output waveguide facets. For a static microcavity waveguide, resonance is detected at 1555.4 nm with a Q of 159, as shown in Figure 2b. Experimental measurements of the tunable cavity resonance, band-edges and other cavity responses are currently underway.

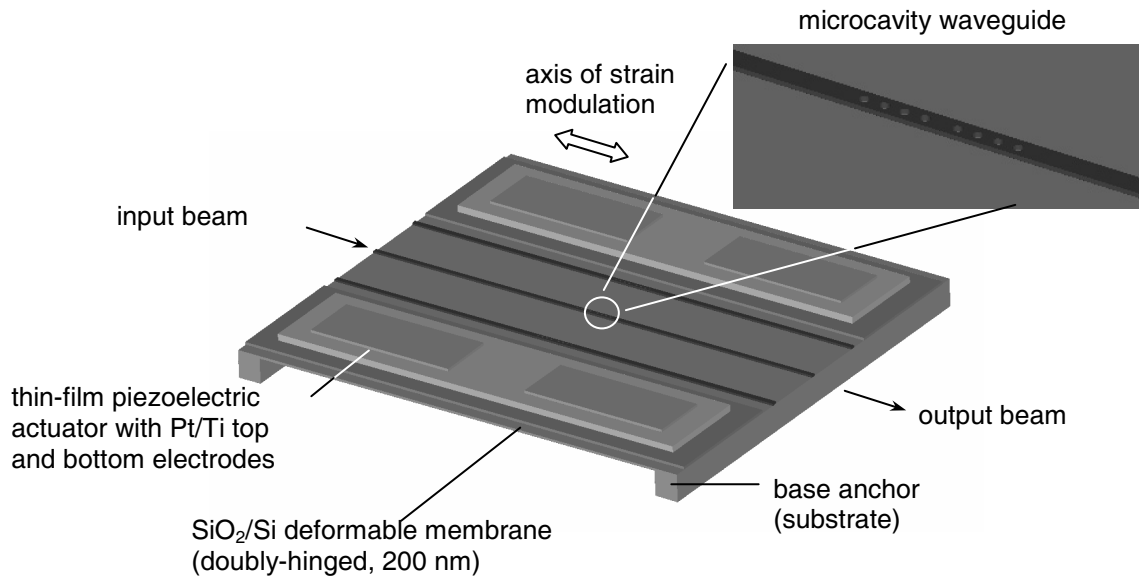


Figure 1. Device schematic of the tunable photonic-bandgap microcavity waveguide, with strain modulation via thin-film piezoelectric actuators on the deformable membrane.

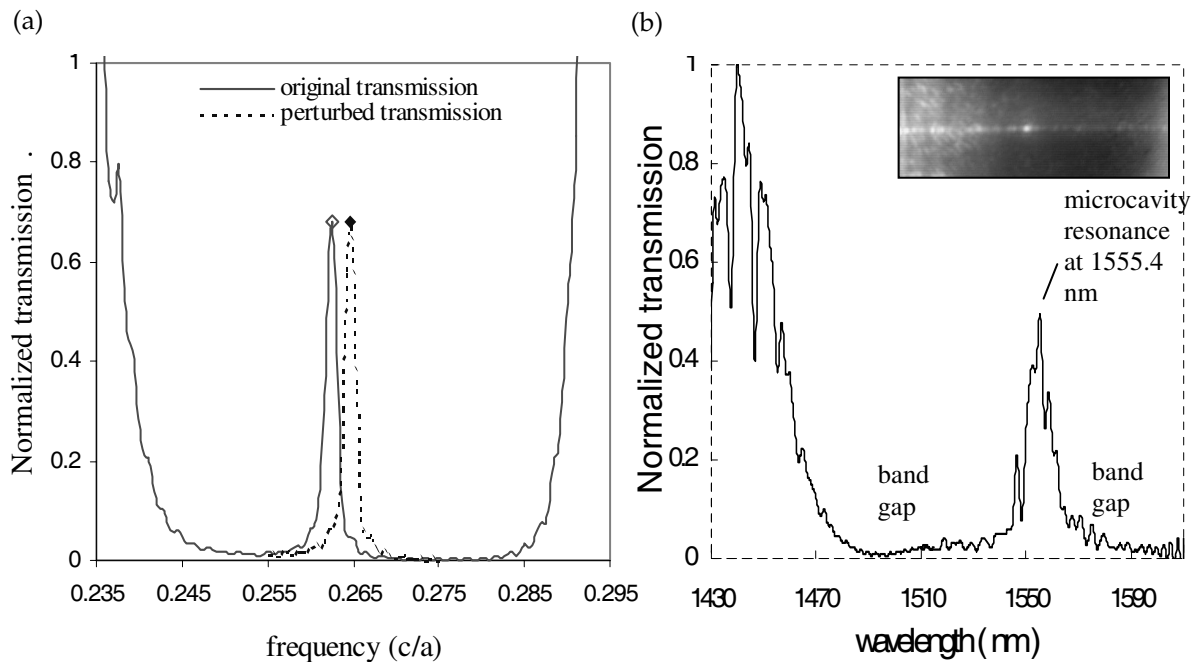


Figure 2. (a) Computed transmission shift through perturbation theory in the photonic band gap, (b) Measured static microcavity resonance with Q of 159. Inset: top view of microcavity waveguide in transmission.

29. Journal Articles, Published

1. C. A. Ross, M. Hwang, M. Shima, J. Y. Cheng, M. Farhoud, T. A. Savas, Henry I. Smith, W. Schwarzacher, F. M. Ross, M. Redjda and F. B. Humphrey, "Micromagnetic behavior of electrodeposited cylinder arrays", *Physical Review B* 65, 144417-1-144417-8 (2002).
2. K-I. Murooka, M.H. Lim, Henry I. Smith, "Membrane Mask Magnification Correction: An Alternate Technique", *J. Vac. Sci. Technol. B*20(1), 370-372 (2002).
3. K-I. Murooka, M.H. Lim, Henry I. Smith, "Effect of thermal diffusion on a membrane-mask-distortion correction and compensation method", *J. Vac. Sci. Technol. B*20(2), 721-724 (2002).
4. Masaki Yoshizawa and T. A. Savas, "A Feasibility Study of 50 nm Resolution with Low Energy Electron Beam Proximity Projection Lithography", *Jpn. J. Appl. Phys.* 41, 87-88 (2002).
5. M. Peuker, "Hydrogen Silses Quioxane, a High Resolution Negative Tone e-beam Resis, Investigated for its Applicability in Photon Based Lithographies", *Microelectronic Engineering*, 61-62, 803-809, (2002).
6. C. A. Ross, S. Haratani, F. J. Castano, Y. Hao, B. Vogeli, M. Farhoud, M. Walsh and Henry I. Smith, "Magnetic behavior of lithographically patterned particle arrays (invited)", *J. Appl. Phys.* 91(10), 6848-6853 (2002).
7. Hans-Jurgen Eisler, Vikram C. Sundar, Mounji G. Bawendi, Michael Walsh, Henry I. Smith, Victor Klimov, "Color-Selective Semiconductor Nanocrystal Laser", *Appl. Phys. Lett.*, 80(24) 4614-4616 (2002).
8. F. J. Castano, S. Haratani, Y. Hao, C. A. Ross, Henry I. Smith, "Giant magnetoresistance in 60-150-nm-wide pseudo-spin-valve nanowires", *Appl. Phys. Lett.* 81(15), 2809-2811 (2002).
9. Y. Hao, F. J. Castano, C. A. Ross, b. Vogeli, M. E. Walsh, Henry I. Smith, "Magnetization reversal in lithographically patterned sub-200-nm Co particle arrays", *J. Appl. Phys.* 91(10), 7989-7991 (2002).
10. F. J. Castano, Y. Hao, C. A. Ross, B. Vogeli S. Haratani, and Henry I. Smith, "Switching field trends in pseudo spin valve nanoelement arrays", *J. Appl. Phys.* 91(10), 7317-7319 (2002).
11. James G. Goodberlet and Hamide Kavak, "Patterning Sub-50 nm features with near-field embedded-amplitude masks", *Appl. Phys. Lett.* 81(7), 1315-1317 ,(2002).
12. C. A. Ross, M. Hwang, M. Shima, Henry I. Smith, M. Farhoud, T. A. Savas, W. Schwarzacher, J. Parrochon, W. Esoffier, H. Neal Bertram, F. B. Humphrey and M. Redjda, "Magnetic properties of arrays of electrodeposited nanowires", *Journal of Magnetism and Magnetic Materials* 249, 200-207, 2002.
13. J.Y. Cheng, C.A. Ross, E.L. Thomas, H.I. Smith, R.G.H. Lammertink and G.J. Vancso, "Magnetic Properties of Large-Area Particle Arrays Fabricated using Block Copolymer Lithography", *IEEE Transactions of Magnetism*, Vol. 38(5) 2541-2543, 2002.

22 – **Nanostructures** – Nanostructures Technology, Research and Applications – 22
RLE Progress Report 145

14. M. Qi and Henry I. Smith, "Achieving nanometer-scale, controllable pattern shifts in x-ray lithography using an assembly-tilting technique", *J. Vac. Sci. Technol. B* 20(6), 2991 – 2994, Nov/Dec. 2002.
15. J.T. Hastings, M.H. Lim, J.G. Goodberlet and Henry Smith, "Optical Waveguides with Apodized Sidewall Gratings via spatial-phase-locked electron-beam lithography", *J. Vac. Sci. Technol. B* 20(6), 2753-2757, Nov/Dec. 2002.
16. Chulmin Joo, G.S. Pati, P. K. Konkola, C. G. Chen, R. Heilmann, E.H. Anderson, Mark Schattenburg, "Precision fringe metrology using a Fresnel zone plate", *J. Vac. Sci. Technol. B* 20(6), 3075-3079, Nov/Dec. 2002.
17. C. G. Chen, R. K. Heilmann, C. Joo, P. T. Konkola, G.S. Pati and Mark L. Schattenburg, "Beam alignment for scanning beam interference lithography", *J. Vac. Sci. Technol. B* 20(6), 3071-3074, Nov/Dec. 2002.
18. G. S. Pati, P.T. Konkola, C. G. Chen, C. Joo, R. K. Heilmann and M. L. Scattenburg, "Generalized scanning beam interference lithography system for patterning gratings with variable period progressions", *J. Vac. Sci. Technol. B* 20(6), 2617-2621, Nov/Dec. 2002.
19. Dario Gil, D.J.D. Carter, R. Menon, X. Tang and Henry I. Smith, "Parallel maskless optical lithography for prototyping, low-volume production, and research", *J. Vac. Sci. Technol. B* 20(6), 2597-2601, Nov/Dec. 2002.
20. M. Yoshizawa, "Sub-50 nm Stencil Mask for Low-Energy Electron-Beam Projection Lithography", *J. Vac. Sci. Technol. B* 20(6), 3021-3024, Nov/Dec. 2002.
21. R.A. Forber, Z.W. Chen, S. Mrowka, C.G. Gaeta, K. Cassidy, H.I. Smith and I.C.E. Turcu, JMAR Research Inc., San Diego, CA, X-Ray Optical Systems, Albany, NY, and MIT, Cambridge, MA, "Collimated Point-Source X-ray Nanolithography", *J. Vac. Sci. Technol. B* 20(6), 2984-2990, Nov/Dec. 2002.
22. Saul Griffith, Mark Mondol, David S. Kong, Joseph M. Jacobson, "Nanostructure Fabrication by Direct Electron-Beam Writing of Nanoparticles", *J. Vac. Sci. Technol. B* 20(6), 2768-2772, Nov/Dec. 2002.

29.1 Journal Articles, Submitted for Publication

1. C. J. Gaeta, H. Rieger, I.E.E. Turcu, R.A. Forber, S.M. Campeau, K.L. Cassdy, M.F. Powers, J.R. Maldonado, G. French, J. Naungayan, C. Kelsy, P. Hark, J.H. Morris, R.M. Foster, H.I. Smith, M.H. Lim, "High Power Compact Laser-Plasma Source for X-Ray Lithography", To be published in the Japanese Journal of Applied Physics, June 2002.
2. C. A. Ross, F. J. Castano, C. Frandsen, D. Gil, Henry I. Smith, M. Redjdal and F. Humphrey, "Twisted states in magnetic nanorings", submitted to *Science* (2002).
3. J. Y. Cheng, C. A. Ross, E. L. Thomas, Henry I. Smith, G. J. Vancso, "Engineering Nanoscale Patterns by Templated Self-Assembly", submitted to *Nature* (2002).

22 – **Nanostructures** – Nanostructures Technology, Research and Applications – 22
RLE Progress Report 145

29.2 Meeting Papers, to be published

1. M. Peuker, "Hydrogen Silses Quioxane, a High Resolution Negative Tone e-beam Resis, Investigated for its Applicability in Photon Based Lithographies", to be published in Microelectronic Engineering, MNE '01. In press (2002)

29.3 Conference Presentations

1. Henry I. Smith, "Templated Self Assembly: The Role of Nanolithography in the Nanotechnology revolution", CMSE Colloquium Series, Fall 2002.

29.4 Theses

1. M. Lim, "Development of x-ray Lithography and Nanofabrication techniques for III-V Optical Devices", Ph.D. Thesis, Department of Electrical Engineering and Computer Science, MIT, February 2002.
2. A. A. Erchak, "Enhanced Performance of Optical Sources in III-V Materials Using Photonic Crystals", Ph.D. Thesis, Department of Materials Science and Engineering, June 2002.

